

# A measurement of the parity violating parameter $A_b$ with a muon tag at the SLD\*

Giulia Bellodi

Stanford Linear Accelerator Center  
Stanford University  
Stanford, CA 94309

SLAC-Report-566  
February 2001

Prepared for the Department of Energy  
under contract number DE-AC03-76SF00515

Printed in the United States of America. Available from the National Technical Information Service, U.S. Department of Commerce, 5285 Port Royal Road, Springfield, VA 22161.

---

\*Ph.D. thesis, Oxford University, Oxford, UK

UNIVERSITY of OXFORD

**A Measurement of the  
Parity Violating Parameter  $A_b$   
with a Muon Tag at the SLD**

A thesis submitted for the degree of

Doctor of Philosophy

in

Physics

by

**Giulia Bellodi, Wolfson College**

Trinity Term 2000

# Contents

<b>Abstract</b>	<b>v</b>
<b>Acknowledgements</b>	<b>vii</b>
<b>List of Figures</b>	<b>ix</b>
<b>List of Tables</b>	<b>xiii</b>
<b>1 Theoretical Introduction</b>	<b>1</b>
1.1 The Standard Model . . . . .	1
1.2 $e^+e^-$ physics at the $Z^0$ resonance . . . . .	3
1.3 A summary of $Z^0$ physics . . . . .	6
1.4 The Asymmetries . . . . .	9
1.4.1 The left-right asymmetry . . . . .	9
1.4.2 The $\tau$ polarization asymmetry . . . . .	10
1.4.3 The forward-backward asymmetry . . . . .	11
1.4.4 The polarized forward-backward asymmetry . . . . .	12
1.5 Radiative corrections and mass effects . . . . .	13
<b>2 Measurement of the Polarized Forward-Backward Asymmetry at SLD/SLC</b>	<b>20</b>
2.1 Introduction . . . . .	20
2.2 $A_b$ sensitivity to New Physics . . . . .	22
2.2.1 Z bosons beyond the Standard Model . . . . .	23
2.2.2 The Minimal SuperSymmetric Model . . . . .	23
2.2.3 Anomalous couplings . . . . .	24
2.3 Measuring the Forward-Backward Asymmetry . . . . .	26
2.3.1 The Jet Charge Method . . . . .	27
2.3.2 The Vertex Charge Method . . . . .	29
2.3.3 $A_b$ with a kaon tag . . . . .	30
2.3.4 $A_c$ with exclusive charmed mesons reconstruction . . . . .	31
2.3.5 $A_c$ analysis with inclusive soft pions . . . . .	32

## Contents

---

2.3.6	$A_c$ with inclusive charm tagging . . . . .	33
2.3.7	Measurement of $A_b$ and $A_c$ with identified leptons . . . . .	34
<b>3</b>	<b>The Experimental Apparatus</b>	<b>35</b>
3.1	The Stanford Linear Collider . . . . .	35
3.1.1	Luminosity . . . . .	39
3.1.2	Polarized Electron Source . . . . .	42
3.1.3	Spin transport . . . . .	44
3.1.4	Polarimetry . . . . .	45
3.1.5	Energy Spectrometer . . . . .	46
3.2	The SLC Large Detector . . . . .	47
3.2.1	The Vertex Detectors . . . . .	49
3.2.2	The Drift Chamber . . . . .	53
3.2.3	The Čerenkov Ring Imaging Detector (CRID) . . . . .	57
3.2.4	Calorimetry . . . . .	60
3.2.5	The Luminosity Monitor . . . . .	67
3.2.6	Data Acquisition . . . . .	69
<b>4</b>	<b>The SLD Monte Carlo</b>	<b>71</b>
4.1	Introduction . . . . .	71
4.1.1	The Event Generator . . . . .	73
4.1.2	Detector Simulation . . . . .	79
<b>5</b>	<b>Event Selection and B Tagging</b>	<b>81</b>
5.1	Hadronic event selection . . . . .	84
5.2	Jet Reconstruction . . . . .	87
5.3	$B$ Hadron Selection . . . . .	90
5.3.1	Vertexing algorithms . . . . .	91
5.4	Muon Selection . . . . .	100
5.4.1	Muon identification in the WIC . . . . .	102
5.4.2	Muon Identification in the CRID . . . . .	105
5.4.3	The Muon- <i>id</i> Algorithm . . . . .	108
<b>6</b>	<b>Measurement of <math>A_b</math></b>	<b>117</b>
6.1	Signal and background . . . . .	118
6.2	The Maximum Likelihood Method . . . . .	120
6.3	Estimate of the muon decay sources . . . . .	123
6.3.1	L/D information . . . . .	130
6.4	Maximum likelihood fit . . . . .	133
6.4.1	$B$ mixing . . . . .	133
6.4.2	$O(\alpha_s)$ QCD corrections . . . . .	135
6.4.3	Background asymmetry . . . . .	140
6.5	Crosscheck: MC as data study . . . . .	143
6.6	Flavour tag calibration . . . . .	145

## Contents

---

6.7	Fit Results . . . . .	148
6.8	Comparison with a different technique (1) . . . . .	152
6.9	Comparison with a different technique (2) . . . . .	157
6.10	Systematic Errors . . . . .	161
6.10.1	Monte Carlo statistics . . . . .	161
6.10.2	Jet axis simulation . . . . .	162
6.10.3	Tracking Efficiency . . . . .	163
6.10.4	Background Level in muon identification . . . . .	166
6.10.5	Background Asymmetry . . . . .	167
6.10.6	$\Gamma(Z^0 \rightarrow b\bar{b}), \Gamma(Z^0 \rightarrow c\bar{c})$ and other branching ratios . . . . .	168
6.10.7	$B^\pm, B^0$ and $B_s$ meson decay lepton spectrum . . . . .	168
6.10.8	$D$ meson decay lepton spectrum . . . . .	169
6.10.9	$B_s$ and $\Lambda_b$ fractions . . . . .	170
6.10.10	$b$ and $c$ quark fragmentation . . . . .	171
6.10.11	$B$ tag systematic error . . . . .	175
6.10.12	L/D systematic errors . . . . .	176
6.10.13	Polarization . . . . .	177
6.10.14	$B$ mixing . . . . .	178
6.10.15	Second order QCD corrections and QCD systematic errors . . . . .	178
6.11	Final results . . . . .	180
<b>7</b>	<b>Conclusions</b>	<b>183</b>
	<b>Bibliography</b>	<b>193</b>

**A Measurement of the  
Parity Violating Parameter  $A_b$   
with a Muon Tag at the SLD**

Giulia Bellodi, Wolfson College

Trinity Term 2000

A thesis submitted for the degree of

Doctor of Philosophy

in

Physics

## **Abstract**

We present a direct measurement of the parity violation parameter  $A_b$ , derived from the left-right forward-backward asymmetry of  $b$  quarks tagged via muons from semileptonic decays. The value of  $A_b$  is extracted using a maximum likelihood fit to the differential cross section for fermion production.

The novelty of this measurement consists in the use of topological vertexing information alongside the more traditional decay kinematics to discriminate among the different sources of tagged leptons. The small and stable SLC beam spot and the CCD based vertex detector are used to reconstruct secondary decay vertices and to provide precise kinematic information and a highly efficient and pure  $B$  mass tag. A multivariate approach has been used, with a total of 4 tagging variables, whose correlation with each other has been taken into account. The final result has been cross-checked both with a classical cut-and-count method and combining all the information into a neural net.

Based on the full SLD dataset of 550K  $Z^0$  events with highly polarized electron beams, this measurement represents an improvement of a factor of 2 with respect to the previously published result (1993-1995 only and with no vertexing information). The statistical sensitivity achieved is around 4% for  $A_b$ , making this a world-class single measurement.

An estimate of  $A_c$  has been simultaneously derived from a common fit, with a precision of about 10%.

## Acknowledgements

First of all, I'd like to express my gratitude to the two SLD spokesmen, Marty Breidenbach and Charles Baltay, without whom this thesis would not probably have been possible. Thanks for never losing your "faith in SLD", even despite the numerous difficulties and impasses encountered along the way, and for pushing its program to the final delivery of excellent physics measurements.

I found working with the SLD collaboration a particularly rewarding experience, both from a professional and a human perspective. Especially during my first year out at SLAC, I enjoyed the daily interchange with my colleagues in a most friendly and laid-back atmosphere, with neither feelings of competition nor other drives apart from sheer scientific curiosity. I'm grateful to all the people I've been working with, and in particular the " $A_b$  gang": Giampiero, for guiding me into this work, "by hand" initially, and then for giving me the necessary competence to carry it on by myself; Bruce, for his helpful suggestions and for directing endless discussions in our meetings, out of his quest for perfection; Su Dong, for his brilliant ideas, and for always being there with an answer, day and night; and again Victor, Sal and Jorge.

I wish to thank also Ramon and Richard Dubois (as well as their counterparts here in Oxford, Pete Gronbeck and John Harris), for having coped with someone pestering them every time there were computing problems.

I'd like to thank my supervisor Dr. Philip N. Burrows for always leaving me freedom in my work, supporting all my requests for visits to SLAC whenever I needed to escape from my desk in Oxford, and also for patiently going and re-going through the drafts of this

thesis (probably finding it a good jet-lag cure during his long-haul flights!).

A special thought goes to all the friends that made my year in the States a particularly enjoyable one: Giampi (again), for letting me guess his thoughts before he could speak them out and for being a living proof that a “naughty mind is a terrible thing to waste” ...even if these are not quite the original words; Robin, for being such a good and open friend, sharing all sorts of more and less serious moments and for introducing me to American habits and ways of life, including a big discovery: margaritas!; and finally all the British lot of PhD and postdoc students, for all the fun we’ve had together.

Another thanks goes to my flatmates (ex-!) here in Oxford, Yasmine and Julian, for cheering me up from the stress of work and the greyness of England with late night chats and confessions of long-legged Oriental women dreaming.

If it was possible to consider a place in this list, I couldn’t fail to mention San Francisco, for providing plenty of escapes for the not so many hours off work, be it a museum exhibition, a concert, a street parade, some bookstore-browsing or just wandering through the streets in the sunshine.

Finally, I’d like to give a special thanks to the people that have been closest to me in this period: my Mum and Dad, for coping with a much felt distance and for nevertheless always supporting myself and my choices unconditionally; Arturo, my “kind of” replacement, for living up to his name, so far; and Phil, for all the things he’s been willing to share with me, on the same and opposite sides of the world. This work would not have been possible without their support and encouragement.

# List of Figures

1.1	Examples of higher level diagrams for $e^+e^- \rightarrow f\bar{f}$ . . . . .	13
1.2	Lowest order Bremsstrahlung contributions to the $e^+e^- \rightarrow Z^0 \rightarrow q\bar{q}$ process. . . . .	15
1.3	Corrections to the $Z^0$ lineshape for initial state radiation. The non-corrected curve is indicated with $\sigma_0$ . . . . .	16
2.1	Standard Model corrections to the $Z^0 \rightarrow b\bar{b}$ vertex. . . . .	22
2.2	Diagrams contributing to $Z^0 \rightarrow b\bar{b}$ in the MSSM model. . . . .	24
2.3	The contour lines show a hundred times the contribution to $A_b$ by diagrams with neutralinos, with $\tan\beta = 70$ . . . . .	25
2.4	In the left plot histograms of $Q_b$ and $Q_{\bar{b}}$ (from Monte Carlo) and Gaussian fits are shown. In the right one is the contour plot of the $Q_b, Q_{\bar{b}}$ joint distribution. . . . .	28
2.5	The mass-difference distributions for the channel $D^{*+} \rightarrow D^0\pi^+$ for the four $D^0$ decay modes. The solid circles indicate the experimental data and histograms are MC signal (open) and Random Combinatoric Background (double hatched). . . . .	31
3.1	Scheme of the SLC accelerator. . . . .	36
3.2	Luminosity history over all SLD runs. The histogram shows the accumulated events per week, while the solid curve shows the integrated luminosity. The average polarization values are also shown. . . . .	41
3.3	Energy levels of the valence and conduction bands for strained GaAs. The Clebsch-Gordon coefficients for the various spin transitions in the case of a right-handed incident photon are also shown. In bulk GaAs, spin-orbit interactions separate the $P_{1/2}$ and $P_{3/2}$ energy levels to provide a maximum polarization of 50%. With a strained lattice, the degenerate $P_{3/2}$ can also be separated and a polarization of nearly 100% can be achieved. . . . .	43
3.4	The polarized source optical system. . . . .	43
3.5	The Compton asymmetry versus the energy of the backscattered electrons is shown for 100% and 77% polarization [47]. . . . .	46
3.6	Isometric view of the SLD detector, with the endcaps removed for clarity. . . . .	48

## List of Figures

---

3.7	Quadrant view of the detector with the IP in the bottom left corner. The detector is both radially and longitudinally symmetric. . . . .	48
3.8	SLD vertex detectors . . . . .	51
3.9	Track impact parameter resolutions as a function of momentum for VXD2 and VXD3 [51]. . . . .	52
3.10	The CDC superlayers. . . . .	54
3.11	The field map for a CDC cell. The figure on the left shows the lines of constant potential (bold) and the lines of constant strength (thin) within a cell. The figure on the right shows a drift path of charges caused by a charged track passing through the cell. . . . .	55
3.12	Distribution of number of hits on a track. . . . .	56
3.13	Geometry of a CRID module: radial view (lower image) and photoelectrons being detected on both sides of the TPC (upper image). . . . .	58
3.14	Schematic view of a TPC and MWPC detector for a CRID module. . . . .	60
3.15	The CRID efficiency matrix. The diagonal plots show the efficiency for correctly tagging a particle. The two peaks represent the efficiencies for the liquid (left) and gas (right) radiators. The off-diagonal are the mis-ID efficiencies. The bands represent the error bars with the center of the band representing the central value for the efficiency [58]. . . . .	61
3.16	View of a LAC module, showing the inner EM and the outer HAD sections. . . . .	63
3.17	Quadrant section of the WIC barrel. . . . .	64
3.18	Cut-away view of the WIC. . . . .	64
3.19	A side view of the SLD LUM, showing the LMSAT and the MASiC. . . . .	68
4.1	Fragmentation functions for uds, c, and b quarks. A value of $m_{\perp} = 300$ MeV/ $c^2$ has been assumed for the Lund symmetric function. . . . .	73
4.2	Lepton momentum distribution in $B^0$ , $B^{\pm}$ meson decays according to CLEO results in comparison with the decay model adopted at SLD. The Monte Carlo contributions from prompt $B \rightarrow l$ and $B \rightarrow D \rightarrow l$ are shown shaded and hatched respectively. CLEO results are represented by open circles for leptons from direct decays, by triangles for leptons from cascade decays, by solid circles (electrons) and stars (muons) for the total spectrum [73]. . . . .	75
4.3	A comparison of the SLD-tuned CLEO $B$ meson decay model (histogram) with inclusive particle spectra from ARGUS (points). . . . .	76
4.4	Comparison of the spectra of $D$ mesons from $B$ decay in the SLD Monte Carlo (histogram) against data measured by CLEO [75] (points). . . . .	77
4.5	Comparison of the spectra of $D$ mesons from $B$ decay in the default JETSET 7.4 model (histogram) against data measured by CLEO [75] (points). . . . .	78
5.1	Distribution of several hadronic event selection variables. Data are represented by points and Monte Carlo by histograms. . . . .	88
5.2	Tracks produced in a typical $B$ decay hemisphere. . . . .	90

**List of Figures**


---

5.3	Topological parameters of a track: D is the distance of the secondary seed vertex from the IP along the line connecting them; T is the transverse distance of the track from the vertex axis calculated at the point of closest approach (POCA) and finally L is the distance from the IP of the projection of the POCA on the vertex axis. . . . .	93
5.4	Illustration of the method to calculate $P_t$ . . . . .	94
5.5	Distributions of the reconstructed raw and $P_t$ -corrected vertex masses for data (dots) and Monte Carlo (histogram). Also shown is the Monte Carlo flavour composition. [88] . . . . .	95
5.6	Residual distributions between a true $B$ direction and a “ghost” track/thrust axis. The “ghost” track gives a better $B$ direction estimate than the thrust axis [52]. . . . .	98
5.7	$B$ reconstruction efficiency curves as a function of the $B$ decay length. Black points indicate the ghost track algorithm and grey points the original topological vertexing algorithm. The ghost track algorithm improves the efficiency along the entire $B$ decay length, in particular at short decay length [52].	99
5.8	Vertex mass distribution for muon hemispheres in 1997-98 data (dots) and Monte Carlo (histogram). . . . .	100
5.9	Muon matching $\chi^2$ distributions for hadronic events after applying various cuts. Shown is data (points) and simulation of all muons (histogram) and background (hashed). (a) All muon candidates. (b) A 1 GeV/c cut in transverse momentum isolates muons from heavy quark decays and therefore produces a smaller fraction of background. (c) Penetration requirements remove much of the background. (d) Muon candidates that fail the penetration requirements are dominated by background [91]. . . . .	104
5.10	Differences in the logarithms of the likelihood function for muons and pions (top) and muons and kaons (bottom), for tracks with momentum $> 2$ GeV/c [91]. . . . .	107
5.11	Differences in the logarithms of the likelihood function for muons and protons (top) and muons and electrons (bottom), for tracks with momentum $> 2$ GeV/c [91]. . . . .	107
5.12	Efficiency of the algorithm for muon identification as a function of the track momentum (top) and of the polar angle (center and bottom) for $p > 2$ and $p > 4$ GeV/c respectively. . . . .	114
5.13	Comparison of efficiency and purity of the muon identification algorithm with and without CRID information. . . . .	116
6.1	Total momentum distribution of identified muons in 1997-98 data (dots) and Monte Carlo (histogram). . . . .	124
6.2	Transverse momentum distribution of identified muons in 1997-98 data (dots) and Monte Carlo (histogram). . . . .	124
6.3	Event mass distribution for muons in 1997-98 data (dots) and Monte Carlo (histogram). The event mass is defined as the largest of the vertex masses found in the two hemispheres. . . . .	125

**List of Figures**


---

6.4	Distribution of $0.5 \ln P$ and $\sqrt{P_t}$ for muons in the 1996-98 data. . . . .	127
6.5	Illustration of the method applied in the $\sqrt{P_t}$ vs $1/2 \ln P$ planes to select MC events to calculate decay source probabilities for the muon in the data. . . .	128
6.6	Stability of the $A_b$ , $A_c$ fit results as a function of the MC sampling area from which decay sources probabilities are derived. . . . .	129
6.7	L/D distribution for muons in 1997-98 data (dots) and Monte Carlo (histogram). . . . .	131
6.8	Tails of the L/D distribution for 1997-98 data (dots) and Monte Carlo (histogram). . . . .	132
6.9	Distribution of the mixing probability $\chi_i$ for $b\bar{b}$ events: highlighted in red is the spectrum of $b$ direct decays and in blue that for $b$ cascade decays. . . .	136
6.10	Contributions of the first order QCD corrections to the polarized forward-backward asymmetry of the $b$ quark as a function of the cosine of the polar angle $\theta$ . In the figure at the top is shown the asymmetry with (dashed line) and without (solid line) QCD corrections. In the figure at the bottom is shown the relative QCD correction $\Delta_{QCD}^b$ for $m_b=4.5$ GeV/ $c^2$ (solid line) and $m_b=0$ (dashed line). . . . .	137
6.11	Angular distribution of: non-leptonic charged tracks in the data (top left) and Monte Carlo (top right), Monte Carlo muons from light hadron decays (bottom left) and misidentified muons (bottom right). . . . .	141
6.12	Results of the asymmetry fit for MC muons from light hadron decays in every transverse momentum bin as a function of the logarithm of the total momentum. . . . .	142
6.13	Distribution of the fitted values of the asymmetry for 1997-98 Monte Carlo background events. . . . .	143
6.14	Dependence of the $B$ tag (left) and ctag (right) purities on the $\cos\theta$ of the jet axis in the low mass region. . . . .	147
6.15	Variation of the logarithm of the maximum likelihood function as a function of $A_b$ and $A_c$ around the maxima for 1997-1998 data. (a) Variation as a function of $A_b$ (with $A_c$ fixed to the fit result value). (b) Variation as a function of $A_c$ (with $A_b$ fixed). . . . .	150
6.16	Contours relative to one and two standard deviations of the logarithm of the maximum likelihood function for 1997-1998 data. . . . .	151
6.17	Elliptic cut on the total and transverse momenta for muons coming from $b$ direct decays (top left), from all other sources (top right), from $b$ cascade decays (bottom left) and from $c$ decays (bottom right). . . . .	153
6.18	Histograms used to calculate the polarized forward-backward asymmetry in $ \cos\theta $ intervals. . . . .	154
6.19	Distributions of the quantity $-Q \cos\theta$ , which gives the $b$ quark direction, for events with positive and negative polarization respectively. . . . .	155
6.20	Asymmetry fit as a function of $\cos\theta$ . . . . .	156
6.21	The architecture used for the source classification neural net (8-10-10-4). It is a full connection, feed forward with back-propagation neural network. . .	157

## List of Figures

---

6.22	Two-dimensional representation of the output nodes, with axes defined by $x = OUT_b + OUT_{bc}$ and $y = OUT_b + OUT_c$ . . . . .	160
6.23	Transverse momentum distribution of all charged tracks in 1997-98 Monte Carlo (histogram) and in the data before (dots) and after (open triangles) applying the smearing. . . . .	163
6.24	At the top: comparison between data (dots) and Monte Carlo (histogram) distributions of the logarithm of the total momentum for 1997-98 charged tracks. At the bottom: ratio of the two distributions. . . . .	164
6.25	At the top: comparison between data (dots) and Monte Carlo (histogram) distributions of the transverse momentum for 1997-98 charged tracks after applying a 15 mrad smearing. At the bottom: ratio of the two distributions. . . . .	165
6.26	Comparison between measured charged hadron production fractions and JETSET rates. The dots represent the $\pi^\pm$ fraction in the data, the triangles the $K^\pm$ fraction in the data, and the lines represent the one-sigma Monte Carlo bands. . . . .	167
6.27	Variations (dashed lines) in the momentum spectrum of muons from $D$ hadron decays adopted to estimate the systematic error, as compared to the SLD MC (solid line). . . . .	170
6.28	Momentum distributions for muons from $B$ hadron direct (left) and cascade (right) decays, for central (solid line) and boundary (dashed lines) values of $\epsilon_b$ . . . . .	172
6.29	Ratio of the momentum distributions of muons from simulations with different values of $\epsilon_b$ and the fit used to weigh events in the Monte Carlo to calculate systematic errors. . . . .	173
6.30	(Top): variations in the momentum distributions of muons from $D$ hadron decays, for the central (solid line) and boundary (dashed lines) values of $\epsilon_c$ . (Bottom left and right): ratios of these distributions and the fits used to weigh Monte Carlo events to calculate systematic errors. . . . .	174
6.31	Ratios of the momentum distributions of primary (left) and secondary (right) muons from simulations with the standard Peterson and the phenomenological Aleph functions. . . . .	175
7.1	Current world measurements of $A_b$ [122]. . . . .	185
7.2	Measurements of $A_l$ , $A_b$ , $A_{FB}^b$ are plotted in the $\delta \sin^2 \theta_W - \delta \zeta$ plane. The SM prediction appears as a horizontal line and the best fit to the data is shown as concentric 68% and 95% ellipses [123]. . . . .	187
7.3	Current world measurements of $\sin^2 \theta_W$ . Hadronic measurements ( $A_{FB}^b$ , $A_{FB}^c$ , $Q_{FB}$ ) tend to be higher than the SM value, whereas purely leptonic ones ( $A_{FB}^l$ , $A_e$ , $A_l$ ) are slightly lower [124]. . . . .	188
7.4	$A_b$ vs $A_e$ from the current LEP and SLD electroweak data, compared to the expectation for the TESLA $Z^0$ factory running. Taken from [133]. . . . .	192

# List of Tables

1.1	Fermions in the Standard Model . . . . .	2
1.2	Fermion and boson masses (from the latest Particle Data Group listings) [7].	3
1.3	$Z^0$ vector and axial couplings to fermions in the Standard Model. . . . .	5
1.4	The values of $A_f$ and its dependence on $\sin^2 \theta_W$ for the different fermions. Values are calculated with $\sin^2 \theta_W = 0.232$ . . . . .	6
1.5	Forward-backward asymmetries sensitivities to $\sin^2 \theta_W$ . . . . .	12
1.6	Electroweak effects on forward-backward asymmetries, as calculated in [23].	16
3.1	Typical beam parameters at the SLC IP for the different running periods. Sizes and divergences are given as single bunch RMS values; the beam polarization is luminosity weighted over each running period. . . . .	40
3.2	Luminosity weighted polarization results [47]. . . . .	46
3.3	Comparison between VXD2 and VXD3. . . . .	53
3.4	SLC luminosity results for the various run periods [55]. . . . .	68
4.1	SLD semileptonic B meson decay branching modes. . . . .	74
4.2	Comparison of branching fractions of B mesons at the $\Upsilon(4S)$ to the different D mesons. Data are the CLEO/ARGUS average in August 1994. . . . .	75
5.1	Number of selected hadronic events in the different running periods. . . . .	87
5.2	Background rejection with cuts on $LLIK_\mu - LLIK_\pi$ for $2 < P < 6$ GeV/c and with cuts on $LLIK_\mu - LLIK_K$ for $P > 2$ GeV/c, for different particle types [91]. . . . .	110
5.3	Results of the muon identification algorithm test on a pure sample of pions selected from $K_s^0$ decays (1996-1998 data). The composition of the MC sample as a function of different cuts is shown. Percentages are relative to the sample selected with a particular choice of cuts. . . . .	111
5.4	Results of the muon identification algorithm test on a sample of pions from 3-prong $\tau$ decays (1996-1998 data). The composition of the MC sample as a function of different cuts is shown. . . . .	113
5.5	Identification efficiencies for muons coming from heavy hadron decays [91]. .	115

## List of Tables

---

5.6	Number of selected hemispheres with a muon track in $Z^0$ hadronic events per running year. . . . .	115
6.1	Composition of Monte Carlo identified muons from the main sources. . . . .	118
6.2	$A_b$ study on the analysis corrections to the first order QCD corrections. . .	138
6.3	Values adopted for some physical quantities in the fit. . . . .	148
6.4	Branching ratios in the SLD Monte Carlo, compared with the world averages [15]. . . . .	152
6.5	Systematic errors on the $A_b$ measurements. . . . .	181
6.6	Systematic errors on the $A_c$ measurements. . . . .	182

# Chapter 1

## Theoretical Introduction

### 1.1 The Standard Model

The unification of the fundamental interactions in nature has been the greatest ambition of high-energy physicists in the last quarter of the century, leading to an integration of personal efforts all over the world.

The 19<sup>th</sup> century saw the first step being taken in this direction with the formulation of the Maxwell equations, which showed how two seemingly separate forces, the electric and the magnetic, are in fact two faces of the same interaction, mediated by the photon.

The weak interaction was discovered at the beginnings of the 1900, through the observation of beta decays in nuclei. Fermi was the first to develop a theory of the phenomenon [1], and Lee and Yang later on observed [2] how this new interaction violated parity, a symmetry that was then assumed to be always satisfied.

In 1956 Yang and Mills [3] gave a new formulation to field theory by introducing non-

## 1.1 The Standard Model

---

<i>Leptons</i>	$\begin{pmatrix} \nu_e \\ e \end{pmatrix}_L$	$\begin{pmatrix} \nu_\mu \\ \mu \end{pmatrix}_L$	$\begin{pmatrix} \nu_\tau \\ \tau \end{pmatrix}_L$	$e_R$	$\mu_R$	$\tau_R$
<i>Quarks</i>	$\begin{pmatrix} u \\ d \end{pmatrix}_L$	$\begin{pmatrix} c \\ s \end{pmatrix}_L$	$\begin{pmatrix} t \\ b \end{pmatrix}_L$	$u_R$	$c_R$	$t_R$
				$d_R$	$s_R$	$b_R$

**Table 1.1:** Fermions in the Standard Model

abelian gauge symmetry groups. On this basis Glashow [4], Weinberg [5] and Salam [6] developed a theory which unifies weak and electromagnetic interactions into an electroweak force. This theory is now accepted as the best description of the phenomenology of fundamental particles and is referred to as the *Standard Model*.

The Standard Model describes all nature as constructed of particles called quarks and leptons (see Table 1.1), which interact through four forces called electro-magnetic, weak, strong and gravitational. Each force is transmitted by one or more gauge bosons, called photons,  $W$ s,  $Z^0$ s, gluons and gravitons. One remaining particle, the Higgs boson, is responsible for giving the  $W$ ,  $Z$  and all leptons and quarks their masses (see Table 1.2).

The validity of this model has been probed in the past few decades with a variety of high precision measurements, and confirmations came from the observation of weak neutral currents, that were predicted by the theory, in 1973 and by the observation of particles like the  $J/\psi$  [8], the  $\tau$  lepton (1975) [9], the  $\Upsilon$  (1977) [10], the top quark (1995) [11] and the  $W^\pm$  [12] and  $Z^0$  [13] gauge bosons (1983).

## 1.2 $e^+e^-$ physics at the $Z^0$ resonance

---

<i>Boson masses (GeV/c<sup>2</sup>)</i>			
	$\gamma$	$m_\gamma \simeq 0$	
	$g$	$m_g = 0$	
	$W$	$m_W = 80.42 \pm 0.06$	
	$Z$	$m_Z = 91.188 \pm 0.002$	
<i>Fermion masses (GeV/c<sup>2</sup>)</i>			
$e$	$m_e = 0.511 \times 10^{-3}$	$\nu_e$	$m_{\nu_e} < 3 \times 10^{-9}$
$\mu$	$m_\mu = 105.66 \times 10^{-3}$	$\nu_\mu$	$m_{\nu_\mu} < 0.19 \times 10^{-3}$
$\tau$	$m_\tau = 1.777$	$\nu_\tau$	$m_{\nu_\tau} < 18.2 \times 10^{-3}$
$u$	$m_u = 1 - 5 (\times 10^{-3})$	$c$	$m_c = 1.15 - 1.35$
$d$	$m_d = 3 - 9 (\times 10^{-3})$	$b$	$m_b = 4.0 - 4.4$
$s$	$m_s = 75 - 170 (\times 10^{-3})$	$t$	$m_t = 174.3 \pm 5.1$

**Table 1.2:** Fermion and boson masses (from the latest Particle Data Group listings) [7].

Two accelerators were built in the 1980s out of this quest to check the Standard Model: the Stanford Linear Collider (SLC) at the Stanford Linear Accelerator Center (SLAC) in California, and the Large Electron Positron (LEP) Collider at the European laboratory CERN in Geneva. Both were designed to produce large quantities of  $Z^0$  bosons, and either confirm the theory or study any new type of physics that could be uncovered.

## 1.2 $e^+e^-$ physics at the $Z^0$ resonance

At the SLC and LEP,  $Z^0$ s are produced at rest by colliding electrons and positrons at  $\sqrt{s}=91.2$  GeV. Once created, the  $Z^0$ s decay almost immediately, usually into two particles, a fermion and its anti-fermion. The probability of a particular interaction occurring in a certain angular configuration is described in particle physics by the differential cross-section for that interaction. For the simple case of two particles colliding together and forming two new particles, the differential cross-section  $d\sigma/d\Omega$  in the centre-of-mass frame

## 1.2 $e^+e^-$ physics at the $Z^0$ resonance

---

is given by [14]:

$$\frac{d\sigma}{d\Omega} = \frac{1}{64\pi^2 s} \frac{p_f}{p_i} |\mathcal{M}|^2, \quad (1.1)$$

where  $s$  is the collision energy squared,  $p_f$  and  $p_i$  the momentum of the final and initial particles, and  $\mathcal{M}$  is the matrix element which contains the dynamics. For the process  $e^+e^- \rightarrow Z^0 \rightarrow f\bar{f}$  at the  $Z^0$  pole,  $\mathcal{M}$  is well approximated by the quantum-field theory expression:

$$\mathcal{M}_Z = [\bar{f}V_f^\mu f] \left( \frac{g_{\mu\nu} - k_\mu k_\nu / M_Z^2}{k^2 - M_Z^2} \right) [\bar{e}V_e^\nu e] \quad [14], \quad (1.2)$$

where  $f$  and  $e$  represent the outgoing fermion and the incoming electron respectively,  $M_Z$  the mass of the  $Z^0$ , and  $k$  the momentum transfer of the  $Z^0$ . The terms in square brackets (*vertex factors*), represent the interaction of the  $Z^0$  with the electrons and the final-state fermions, and the central term (*propagator*) describes how the  $Z^0$  transfers four-momentum from the electron and positron collision to create the fermion/anti-fermion pair. According to the Standard Model, the vertex factor  $Z^0 f\bar{f}$  can be described by:

$$-i \frac{g}{2 \cos \theta_W} \gamma^\mu (c_V - c_A \gamma^5),$$

where the constants  $g$ ,  $\theta_W$ ,  $c_V$  and  $c_A$  are the electroweak-coupling, the Weinberg angle and vector and axial couplings respectively. The quantum field theory matrix  $\gamma^5$  is a parity-reversing operator, and in the expression  $(c_V - c_A \gamma^5)$ , with  $c_V \neq 0$ ,  $c_A \neq 0$ , it is the source of the parity violating nature of the weak force. The Standard Model also predicts that:

$$c_V = T_3 - 2Q \sin^2 \theta_W \quad (1.3)$$

$$c_A = T_3,$$

## 1.2 $e^+e^-$ physics at the $Z^0$ resonance

---

Fermions	$Z^0$ couplings			
	$Q_f$	$T_3$	$c_A$	$c_V$
$\nu_e, \nu_\mu, \nu_\tau$	0	1/2	1/2	1/2
$e, \mu, \tau$	-1	-1/2	-1/2	$-\frac{1}{2} + 2 \sin^2 \theta_W$
$u, c, t$	2/3	1/2	1/2	$\frac{1}{2} - \frac{4}{3} \sin^2 \theta_W$
$d, s, b$	-1/3	-1/2	-1/2	$-\frac{1}{2} + \frac{2}{3} \sin^2 \theta_W$

**Table 1.3:**  $Z^0$  vector and axial couplings to fermions in the Standard Model.

where  $Q$  is the charge of the fermion, and  $T_3$  the third component of the weak isospin, equal to 1/2 for neutrinos and up-type quarks and -1/2 for leptons and down-type quarks. The values of  $c_V$  and  $c_A$  are listed in Table 1.3 for each type of fermion. The resulting differential cross-section for longitudinally polarized electrons and massless fermions is obtained by multiplying the decay rate by the magnitude of the cross section for producing polarized  $Z^0$ s:

$$\begin{aligned} \frac{d^2\sigma^f(P_e)}{d\Omega} &\propto \left[ c_V^e{}^2 + c_A^e{}^2 - 2c_V^e c_A^e P_e \right] \times \left[ (c_V^f{}^2 + c_A^f{}^2)(1 + \cos^2\theta) - 4P_{Z^0}(P_e)c_V^f c_A^f \cos\theta \right] \\ &\propto (1 - A_e P_e)(1 + \cos^2\theta) + 2(A_e - P_e)A_f \cos\theta, \end{aligned} \quad (1.4)$$

where

- $P_e$  is the polarization of the electron beam;
- $\theta$  is the angle between the momentum of the fermion and the electron beam direction;
- $P_{Z^0}(P_e)$  is the polarization of the  $Z^0$  given by

$$P_{Z^0}(P_e) = \frac{P_{Z^0}(0) + P_e}{1 + P_{Z^0}(0)P_e},$$

where  $P_{Z^0}(0)$  is the  $Z^0$  polarization for unpolarized electrons

$$P_{Z^0}(0) = -2c_V^e c_A^e / ((c_V^e)^2 + (c_A^e)^2) = -A_e;$$

### 1.3 A summary of $Z^0$ physics

---

Fermions	$A_f$	$\partial A_f / \partial(\sin^2 \theta_W)$
$\nu_e, \nu_\mu, \nu_\tau$	1	0
$e, \mu, \tau$	0.155	-8.5
$u, c, t$	0.667	-3.5
$d, s, b$	0.935	-0.64

**Table 1.4:** The values of  $A_f$  and its dependence on  $\sin^2 \theta_W$  for the different fermions. Values are calculated with  $\sin^2 \theta_W = 0.232$ .

- and  $A_f$  is an asymmetry parameter expressed by:

$$A_f = \frac{2c_V^f c_A^f}{(c_V^f)^2 + (c_A^f)^2}. \quad (1.5)$$

The value of  $A_f$  for the different fermions is listed in Table 1.4.

### 1.3 A summary of $Z^0$ physics

This section wants to briefly summarize some of the physics studies that are possible at the SLC and LEP. The next section will describe in more details the measurements of asymmetries.

#### The $Z^0$ width and mass and neutrino counting

The  $Z^0$  lineshape is extracted from measurements of the cross-section for  $e^+e^-$  annihilation at centre of mass energies near the  $Z^0$  resonance: any deviation from this energy ( $|\sqrt{s} - M_Z| \geq \Gamma_Z$ , where  $\Gamma_Z$  is the  $Z^0$  decay width, inversely proportional to the lifetime  $\tau$ ) and the  $Z^0$  production falls rapidly. The  $Z^0$  mass can be measured by varying the collision energy until  $Z^0$  production is maximized, and the width can be measured by observing the rate at which  $Z^0$  production falls when moving away from the maximum.

### 1.3 A summary of $Z^0$ physics

---

By comparing the quark and lepton partial widths against the total  $Z^0$  width it is then possible to determine the total number of neutrino families. The latest measurements are:  $m_Z = 91.187 \pm 0.002$  GeV/ $c^2$ ,  $\Gamma_Z = 2.494 \pm 0.002$  GeV and  $N_\nu = 2.984 \pm 0.008$  [15].

#### The $b$ and $c$ partial widths

The partial widths for  $Z^0$  decay into  $b\bar{b}$  or  $c\bar{c}$  events can also be measured. Of the five types of quarks that the  $Z^0$  can decay into, the  $b$  decay mode is the easiest to identify. The average LEP and SLD results are:  $R_b = \frac{\Gamma_b}{\Gamma_{had}} = 0.2164 \pm 0.0007$  and  $R_c = \frac{\Gamma_c}{\Gamma_{had}} = 0.1674 \pm 0.0038$  [15].

#### B hadron lifetimes

Because of the weak force,  $b$  quarks are unstable, and will eventually decay into lighter quarks. This gives all  $B$  hadrons a finite lifetime, which is long enough to be measured with a detector. In principle, the Standard Model can predict the lifetime of any particular type of  $B$  hadron exactly. In practice, calculations are often too difficult to solve and only approximations are available. Most of the uncertainties can be removed, however, by estimating the ratio of the lifetimes of different types of  $B$  hadrons. Current results are:  $\tau_{B^+} = 1.656 \pm 0.025$  ps,  $\tau_{B^0} = 1.562 \pm 0.029$  ps,  $\tau(B^+)/\tau(B^0) = 1.065 \pm 0.023$  [16].

#### QCD studies

There are different reasons why  $Z^0$  quark decays are useful for QCD studies:

1. the decays are relatively clean, involving (initially) the simple system of two quarks;

### 1.3 A summary of $Z^0$ physics

---

2. the measurements at SLC and LEP can be compared to those from lower energy experiments to study how QCD phenomena scale with energy;
3. measurements of the lifetime of  $b$  hadrons and  $\tau$  leptons can be used to confirm QCD calculations.

In  $e^+e^-$  experiments a couple of aspects of the strong interaction are of particular interest. The first is the structure of events in terms of jets, from which we can extract the strong coupling  $\alpha_s$ , the quantum numbers of quarks and gluons, and test predictions of the theory in terms of numbers of jets and the distributions of angles between them. The second is the “fragmentation” or “hadronization process”, by which quarks and gluons materialize as hadrons. In addition to fundamental inclusive tests of QCD, new fragmentation studies involving the dependence on the flavor of the primary quark, differences between quark and antiquark jets, and dependence on the mass of the final state hadrons have been performed at SLD. Many QCD calculations assume massless quarks, and therefore they can be tested using the light-quark sample. Some other calculations predict interesting differences between heavy and light-quark jets. The polarized electron beam at the SLC causes the quark jet in  $Z^0 \rightarrow q\bar{q}$  events to point preferentially in a certain direction. In this way quark jets can be separated from antiquark jets and their properties compared. By identifying the types of the final state hadrons, the mass-dependence of the fragmentation process can be studied as well as the way the quantum numbers of the initial quark are transmitted to the final state. SLD has excellent identification capabilities for charged pions, kaons and protons using Čerenkov ring-imaging, which allows the study of these hadrons as well as the reconstruction of many unstable higher mass states with a good

## 1.4 The Asymmetries

---

signal to noise ratio [17].

### 1.4 The Asymmetries

There are four types of asymmetry that can be measured at SLC and/or LEP:

1. the left-right asymmetry;
2. the  $\tau$  polarization asymmetry;
3. the forward-backward asymmetry;
4. the forward-backward polarized asymmetry.

At energies below or beyond the  $Z^0$  mass, these asymmetries are due to the interference of the electromagnetic vector and the weak axial interactions, whereas at the  $Z^0$  pole they are due to the interference of the weak vector and axial interactions.

#### 1.4.1 The left-right asymmetry

According to (1.4), the number of  $Z^0$ s created depends on the polarization of the beam. The *left-right asymmetry* is defined as:

$$A_{LR}^0 \equiv \frac{\sigma_L - \sigma_R}{\sigma_L + \sigma_R} = \frac{2c_V^e c_A^e}{c_V^{e^2} + c_A^{e^2}} = \frac{2[1 - 4 \sin^2 \theta_W^{eff}]}{1 + [1 - 4 \sin^2 \theta_W^{eff}]} = A_e, \quad (1.6)$$

where  $\sigma_L$  and  $\sigma_R$  are the  $e^+e^-$  production cross sections for  $Z^0$  bosons at the  $Z^0$  pole energy with left-handed and right-handed electrons respectively. Because the left-right asymmetry is not dependent on final state couplings, all  $Z^0$  hadronic and  $\tau^+\tau^-$  decays

## 1.4 The Asymmetries

---

can be used <sup>1</sup>, which is a great advantage with respect to other Standard Model tests that can only use a small fraction of observable events. Furthermore,  $A_{LR}$  does not depend on the detector acceptance since there is no dependence on integration boundaries: one can simply sum over all final states (hadronic and leptonic) even if the apparatus has inhomogeneities in acceptance.

$A_{LR}$  does not show a strong dependence on initial state radiative corrections either, but it is a very sensitive function of  $\sin^2 \theta_W^{eff}$  ( $\delta A_{LR} \simeq -8\delta \sin^2 \theta_W$ ) and depends upon virtual electroweak radiative corrections including those which involve the Higgs boson and those arising from new phenomena outside the scope of the Standard Model. Presently, the most stringent upper bounds on the SM Higgs mass are provided by measurements of  $\sin^2 \theta_W^{eff}$ .

The SLD results for the complete 1992-1998 dataset are [18]:

$$A_{LR}^0 = 0.15138 \pm 0.00216, \tag{1.7}$$

$$\sin^2 \theta_W^{eff} = 0.23097 \pm 0.00027.$$

This is the most precise measurement of  $\sin^2 \theta_W$  presently available, and is smaller by 2.7 standard deviations than the recent average of measurements performed at LEP [15].

### 1.4.2 The $\tau$ polarization asymmetry

The  $\tau$  lepton is the only fundamental fermion whose polarization is experimentally accessible at LEP. The average value of the final state  $\tau$  lepton polarization without

---

<sup>1</sup>the  $e^+e^-$  final states are excluded because their asymmetry is diluted by the  $t$ -channel photon exchange sub-process, and  $\mu^+\mu^-$  events are excluded too on the ground that they deposit little energy in the calorimeter (the event selection is calorimeter based).

## 1.4 The Asymmetries

---

polarized beams is given by:

$$P_\tau = \frac{-A_\tau - A_e(2 \cos \theta / (1 + \cos^2 \theta))}{1 + A_\tau A_e(2 \cos \theta / (1 + \cos^2 \theta))}. \quad (1.8)$$

A measurement of the polar angle distribution of the  $\tau$  polarization can be compared with (1.8), and  $A_\tau$  and  $A_e$  can be determined. Since the denominator of equation 1.8 is very close to unity, it is possible to have independent measurements of the two parameters: the average polarization constrains the value of  $A_\tau$  whereas the angular dependence provides information on  $A_e$ . This measurement is however inferior to the left-right asymmetry, because it can only use  $\tau$  decays and because of the systematic uncertainties related to the  $\tau$  channel identification. The latest LEP measurements are:  $A_\tau = 0.1425 \pm 0.0044$  and  $A_e = 0.1483 \pm 0.0051$  [15].

### 1.4.3 The forward-backward asymmetry

The linear term in  $\cos \theta$  in the formula for the cross section (1.4) introduces a forward-backward asymmetry, (even in the absence of polarized beams), which is defined as the normalized difference of the cross sections with the final state fermion entering the front part of the detector ( $\sigma(\cos \theta) > 0$ ) or the back ( $\sigma(\cos \theta) < 0$ ):

$$A_{FB}^f \equiv \frac{\sigma_f(\cos \theta > 0) - \sigma_f(\cos \theta < 0)}{\sigma_f(\cos \theta > 0) + \sigma_f(\cos \theta < 0)} = \frac{3}{4} A_f A_e \quad (1.9)$$

(in the case of full solid angle acceptance).

The forward-backward asymmetry is very small for charged leptons and increases in value in the quark sector: in Table 1.5 are listed the Standard Model predictions together with the sensitivities to  $\sin^2 \theta_W$ . It has to be stressed that the forward-backward asymmetry

## 1.4 The Asymmetries

---

Fermions	$A_{FB}$	$\delta A_{FB}/\delta \sin^2 \theta_W$
$\mu, \tau$	0.012	1.5
$u, c$	0.063	4.2
$d, s, b$	0.089	5.6

**Table 1.5:** Forward-backward asymmetries sensitivities to  $\sin^2 \theta_W$ .

only measures the combination  $\frac{3}{4}A_e A_f$  where most of the dependence on  $\sin^2 \theta_W$  comes from  $A_e$ , in the case of quark final states; therefore, one has to use theoretical/experimental values of  $A_e$  when measuring  $A_f$ . Finally,  $A_{FB}$  is a very rapid function of  $\sqrt{s}$ , especially around the  $Z^0$  pole, so that radiative corrections due to QED and QCD effects have to be measured very precisely.

### 1.4.4 The polarized forward-backward asymmetry

In the presence of polarized beams it is possible to introduce a new definition of forward-backward polarized asymmetry :

$$\tilde{A}_{FB}^f \equiv \frac{1}{\mathcal{P}} \frac{(\sigma_{\mathcal{P}_F} - \sigma_{-\mathcal{P}_F}) - (\sigma_{\mathcal{P}_B} - \sigma_{-\mathcal{P}_B})}{(\sigma_{\mathcal{P}_F} + \sigma_{-\mathcal{P}_F}) + (\sigma_{\mathcal{P}_B} + \sigma_{-\mathcal{P}_B})}, \quad (1.10)$$

(where  $\sigma_{\pm\mathcal{P}_F}$  ( $\sigma_{\pm\mathcal{P}_B}$ ) is the integrated cross section for  $\cos \theta > 0$  ( $< 0$ ) for a certain polarization  $\pm\mathcal{P}$ ), which at the  $Z^0$  pole becomes:

$$\tilde{A}_{FB}^f = \frac{3}{4} \frac{2c_A^f c_V^f}{c_V^{f2} + c_A^{f2}} = \frac{3}{4} A_f. \quad (1.11)$$

Unlike the unpolarized forward-backward asymmetry previously defined, this quantity is completely independent of the  $Z^0$  couplings to the initial state electron; it is therefore possible to study the corrections to the decay  $Z^0 f \bar{f}$  vertex independently from those at the production vertex  $Z^0 e^+ e^-$ , being potentially sensitive to new particles with different

## 1.5 Radiative corrections and mass effects

---

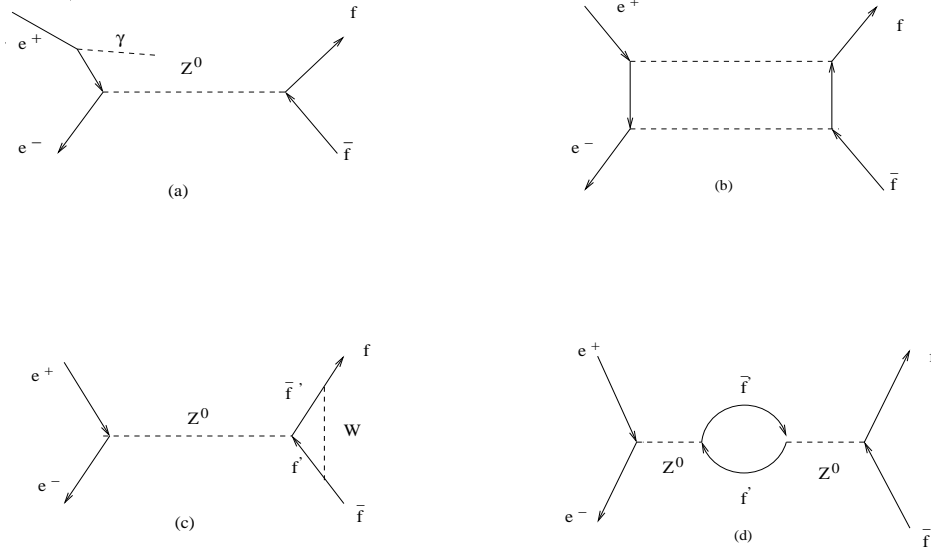


**Figure 1.1:** Examples of higher level diagrams for  $e^+e^- \rightarrow f\bar{f}$ .

couplings at the two vertices. The experimental asymmetry is related to the theoretical expression by:

$$\tilde{A}_{FB}^{f\text{exp}} = P_e \tilde{A}_{FB}^f = \frac{3}{4} P_e A_f. \quad (1.12)$$

## 1.5 Radiative corrections and mass effects

Radiative effects change the Born level cross sections and the asymmetries, so they have to be accounted for in the models used in the different analyses.

The  $\tilde{A}_{FB}^b$  dependence on  $\sin^2 \theta_W$  is very small and varies slightly with radiative corrections (this is because  $A_b$  is not particularly sensitive to vacuum polarization effects and because the  $b$  quark coupling to the photon is relatively weak).

Higher-order corrections to the Eq. 1.12 can be separated into two classes, examples of which are illustrated in fig. 1.1:

## 1.5 Radiative corrections and mass effects

---

- purely electromagnetic corrections: they comprise Feynman diagrams with either external photons (radiated from the external fermions) or virtual photons, which start and terminate on the external fermions (fig. 1.1.a). These include box diagrams (fig. 1.1.b) with the exchange of either two virtual photons or one virtual photon and one virtual massive boson.
- electroweak corrections: they comprise oblique corrections to the vector boson propagator (fig. 1.1.d), vertex diagrams (fig. 1.1.c) and also box diagrams with two massive bosons exchanged.

Box diagrams involving weak bosons, that would spoil the property of  $\tilde{A}_{FB}^f$  of depending only on the final state couplings are extremely small [19]. Oblique corrections (vector bosons self-energies) contribute to the renormalization of the final state couplings and at the  $Z^0$  resonance they affect all measurements in the same way as an effective change in the value of  $\sin^2 \theta_W$ . Therefore, the oblique-corrected value of the polarized forward-backward asymmetry can be simply related to the corrected value of the left-right asymmetry [20]:

$$\delta^{obl} \tilde{A}_{FB}^f = k \cdot \delta^{obl} A_{LR}$$

where  $k = 3/4$  for  $f = \mu, \tau$ ,  $9/25$  for  $f = u, c$  and  $1/15$  for  $f = d, s, b$ . The ratio of proportionality  $k$  is given exactly by the derivative of the Born expressions with respect to  $\sin^2 \theta_W$ , showing that in the case of quarks these corrections are much smaller than in the case of leptons. Peskin and Takeuchi have parametrized these effects in a model independent manner using 3 independent variables S,T,U [21].

Standard Model vertex corrections are small too, as will be illustrated in the next chapter:

## 1.5 Radiative corrections and mass effects

---

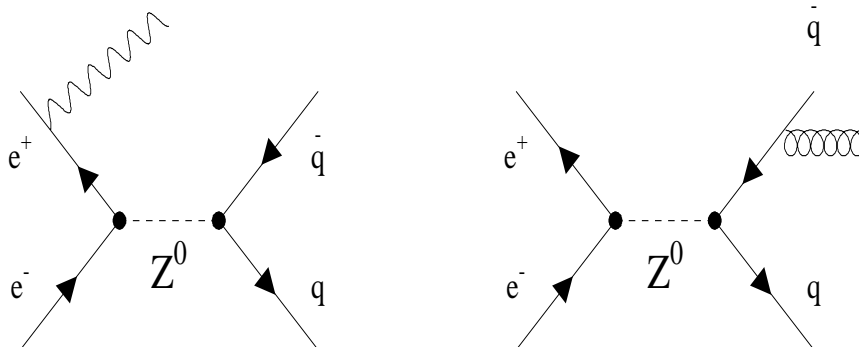


**Figure 1.2:** Lowest order Bremsstrahlung contributions to the  $e^+e^- \rightarrow Z^0 \rightarrow q\bar{q}$  process.

for this reason the predicted value of  $A_b$  is known with only a small uncertainty due to the  $m_{top}$  and  $m_{Higgs}$  masses and any deviation from it would be a signal of new physics.

Energy emission by charged accelerated particles (*Bremsstrahlung*) can be of two types (see fig. 1.2): photon emission in the initial state and gluon emission in the final state (photon emission in the final state is suppressed by the quark fractional charge and by a factor  $(\alpha_{EM}/\alpha_s)^2$  (where  $\alpha_{EM}$  and  $\alpha_s$  are respectively the electromagnetic and strong coupling constants).

Photons emitted in the initial state reduce the energy in the centre of mass and boost the decay products in the lab system. This broadens the  $Z^0$  resonance curve and shifts its peak towards higher energies, breaking the symmetry of the curve (see fig. 1.3).

However, in contrast with the case of the unpolarized asymmetries, the forward-backward polarized asymmetry is a parity-violating quantity and has a very smooth dependence on  $\sqrt{s}$  near the  $Z^0$  peak. These two facts lead to expect that QED effects, that are parity

## 1.5 Radiative corrections and mass effects

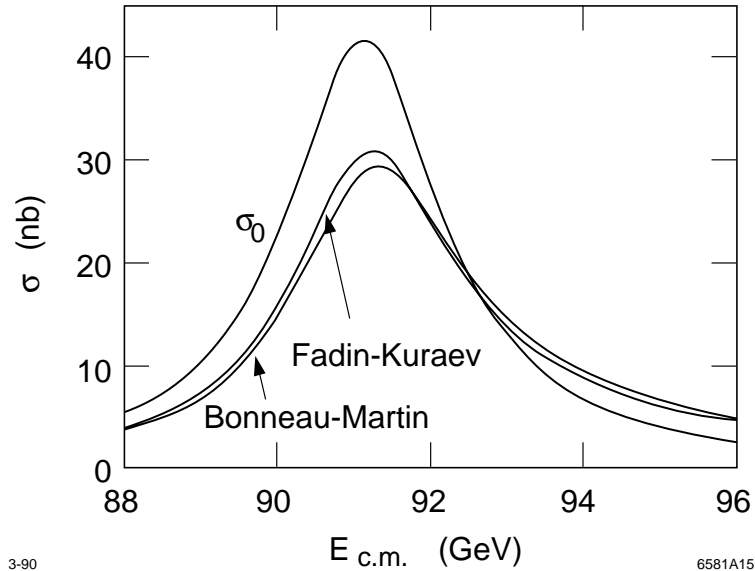


**Figure 1.3:** Corrections to the  $Z^0$  lineshape for initial state radiation. The non-corrected curve is indicated with  $\sigma_0$ .

Type of correction	$\tilde{A}_{FB}^f$	Unpolarized $A_{FB}$
Photon exchange	< 0.1%	< 0.1%
Vertex corrections	< 0.1%	5 – 6%
Initial state radiation	< 0.1%	3 – 4%
Box diagrams	< 0.1%	< 0.1%
Oblique corrections	$\sim 1\%$	1.5%

**Table 1.6:** Electroweak effects on forward-backward asymmetries, as calculated in [23].

conserving and that result in an effective shift of the centre-of-mass energy, should be of no relevance [22]. A summary of these corrections, as derived from numerical simulations [23] is given in Table 1.6.

Electroweak radiative effects account for a relative downward shift of 0.23% in  $A_b$ , and the measurement in this thesis will be corrected for this.

Final state gluon emission only changes the width of the curve, since it allows a larger number of final states into which the  $Z^0$  can decay, reducing its average lifetime. The most

### 1.5 Radiative corrections and mass effects

---

important effect of the final state radiation in the measurement of the asymmetries is the smearing of the primary quark direction. These corrections to the polar angle distribution have been calculated in first order perturbative QCD for polarized beams by J. Stav and H. Olsen [24], in the case of massive quarks. The cross-section therefore becomes:

$$\begin{aligned}
\frac{d\sigma_f}{d\cos\theta} &= \frac{3\pi}{2} \left( \frac{\alpha}{4\sin^2\theta_W} \right)^2 \frac{\beta}{\Gamma^2} \left\{ (v^2 + a^2 - 2avP_e) \right. \\
&\times \left[ (v_f^2 + a_f^2) \left( 1 + \frac{\bar{m}_f^2}{2} \right) \left( 1 + \frac{4\alpha_s}{3\pi} F_1(\bar{m}_f) \right) - \frac{3}{2} \alpha_f^2 \bar{m}_f^2 \left( 1 + \frac{4\alpha_s}{3\pi} F_4(\bar{m}_f) \right) \right] \\
&\times (1 + \cos^2\theta) \\
&+ (v^2 - a^2 - 2avP_e) \left[ (v_f^2 + a_f^2) \left( \frac{\bar{m}_f^2}{2} + \frac{4\alpha_s}{3\pi} F_2(\bar{m}_f) \right) - \alpha_f^2 \frac{\bar{m}_f^2}{2} \left( 1 + \frac{4\alpha_s}{3\pi} F_5(\bar{m}_f) \right) \right] \\
&\times (1 - 3\cos^2\theta) \\
&\left. + 4a_f v_f \beta [2av - (v^2 + a^2)P_e] \left( 1 + \frac{4\alpha_s}{3\pi} F_3(\bar{m}_f) \right) \cos\theta \right\}, \tag{1.13}
\end{aligned}$$

where  $\bar{m}_f = 2m_f/M_Z$ ,  $\beta = \sqrt{1 - \bar{m}_f^2}$ ,  $a$ ,  $v$ ,  $a_f$ ,  $v_f$  are the coupling constants of the  $Z^0$  to  $e$  and to the quark  $f$  respectively and  $P_e$  is the polarization. The expressions for the form factors  $F_i(\bar{m}_f)$  ( $i=1,2,3,4,5$ ) are the following:

$$\begin{aligned}
F_1(\bar{m}_f) &= \frac{3}{4}(1 + 3\bar{m}_f^2), \\
F_2(\bar{m}_f) &= \frac{3}{4} \left[ \frac{2}{3} - \frac{\pi^2}{6} \bar{m}_f - \bar{m}_f^2 \left( \frac{1}{3} + \frac{\pi^2}{9} + \ln \frac{\bar{m}_f}{2} + \frac{1}{3\ln^2 \frac{\bar{m}_f}{2}} \right) \right], \\
F_3(\bar{m}_f) &= \frac{3}{4} \left[ \frac{8}{3} \bar{m}_f + \bar{m}_f^2 \left( \frac{7}{3} + \frac{\pi^2}{18} - \frac{2}{3} \ln \frac{\bar{m}_f}{2} + \frac{1}{3} \ln^2 \frac{\bar{m}_f}{2} \right) \right], \\
F_4(\bar{m}_f) &= \frac{3}{4} \left( 3 + 4\ln \frac{\bar{m}_f}{2} \right) \\
F_5(\bar{m}_f) &= \frac{3}{4} \left( 5 + 4\ln \frac{\bar{m}_f}{2} \right). \tag{1.14}
\end{aligned}$$

### 1.5 Radiative corrections and mass effects

---

The polarized forward-backward asymmetry therefore becomes:

$$\begin{aligned}
\tilde{A}_{FB}^f|_{O(\alpha_s)} &= 2P_e\beta A_f \left( 1 + \frac{4\alpha_s F_3(\bar{m}_f)}{3\pi} \right) \cos\theta / & (1.15) \\
&\left\{ 1 + \bar{m}_f^2 + \frac{4\alpha_s}{3\pi} \left( F_1(\bar{m}_f) \left( 1 + \frac{\bar{m}_f^2}{2} \right) + F_2(\bar{m}_f) \right) \right. \\
&+ \cos^2\theta \left( 1 - \bar{m}_f^2 + \frac{4\alpha_s}{3\pi} \left( F_1(\bar{m}_f) \left( 1 + \frac{\bar{m}_f^2}{2} \right) - 3F_2(\bar{m}_f) \right) \right) \\
&- \frac{2a_f^2}{v_f^2 + a_f^2} \bar{m}_f^2 \left( 1 + \frac{\alpha_s}{3\pi} (3F_4(\bar{m}_f) + F_5(\bar{m}_f)) \right. \\
&\left. \left. + \frac{\alpha_s}{\pi} \cos^2\theta (F_4(\bar{m}_f) - F_5(\bar{m}_f)) \right) \right\}
\end{aligned}$$

The correction is a function of the polar angle and varies between 0 and 5% (6%) for the  $b$  ( $c$ ) quark.

For zero mass quarks the second order QCD corrected forward-backward left-right asymmetry is [25]:

$$\tilde{A}_{FB}^f = \left( \tilde{A}_{FB}^f \right)_0 F_{QCD} = \left( \tilde{A}_{FB}^f \right)_0 \left\{ 1 - c_1^f \frac{\alpha_s}{\pi} + c_2^f \left( \frac{\alpha_s}{\pi} \right)^2 + O \left[ \left( \frac{\alpha_s}{\pi} \right)^3 \right] \right\}, \quad (1.16)$$

where  $f = b, c$ . The coefficients  $c_1^f$  are roughly equal to 0.79 for the  $b$  quark and 0.92 for the  $c$  quark, but they have been derived for a full angular coverage (so we use Eq. 1.15 instead). At  $O(\alpha_s)^2$  we have implemented recent calculations by Ravindran and van Neerven [25] for  $\mu = M_Z$  (CM energy),  $m_b = 4.50$  GeV/ $c^2$  and  $m_c = 1.50$  GeV/ $c^2$ . They obtain for the second order coefficients:

$$c_2^b = -8.89 + F_{gl. splitt.}^b \quad (1.17)$$

$$c_2^c = -11.5 + F_{gl. splitt.}^c$$

The first term in these expressions accounts for hard gluon emission, whereas the second one is due to the *gluon splitting* effect, i.e. the emission of a virtual gluon in an  $e^+e^- \rightarrow q\bar{q}$

## 1.5 Radiative corrections and mass effects

---

event, with  $q \neq f$ , which then decays into a  $f\bar{f}$  pair. This quantity depends on the event selection and analysis procedure and it has been evaluated with a Monte Carlo study.

The transition from the fixed pole mass to the running mass approach does not introduce large changes in the values of  $\tilde{A}_{FB}^f$  for  $f = b, c$  (as long as  $\mu \gg m_f$ ); also a variation of the renormalization scale does not lead to large effects, which are comparable to the ones between the running mass/pole mass approaches.

# Chapter 2

## Measurement of the Polarized Forward-Backward Asymmetry at SLD/SLC

### 2.1 Introduction

As described with more details in the first chapter, parity violation in the  $Zf\bar{f}$  coupling is given by the observable:

$$A_f = \frac{g_L^2 - g_R^2}{g_L^2 + g_R^2} = \frac{2c_V^f c_A^f}{(c_V^f)^2 + (c_A^f)^2} \quad (2.1)$$

where  $g_L = (c_V^f + c_A^f)/2$  and  $g_R = (c_V^f - c_A^f)/2$ . This is complementary to other quantities proportional to  $(c_V^f)^2 + (c_A^f)^2$  (e.g.  $R_b$ ) in the complete determination of the strength of the vertex couplings. For  $Zb\bar{b}$  and  $Zc\bar{c}$  vertices in particular,  $A_b$  and  $A_c$  are more sensitive

## 2.1 Introduction

---

to the right-handed coupling, whereas  $R_b$  and  $R_c$  are more sensitive to the left-handed one (since  $g_L \gg g_R$ ).

Experimentally,  $A_f$  can be measured through the forward-backward asymmetry for fermion production in the process  $e^+e^- \rightarrow Z^0 \rightarrow f\bar{f}$ , which is given in the Born approximation by:

$$A_{FB}^f(z) = \frac{\sigma^f(z) - \sigma^f(-z)}{\sigma^f(z) + \sigma^f(-z)} = A_e A_f \frac{2z}{1+z^2}, \quad (2.2)$$

where  $z = \cos \theta$  is the direction of the quark  $f$  with respect to the electron beam.

In the presence of polarized incident electrons one can define a left-right forward-backward asymmetry:

$$\tilde{A}_{FB}^f(z) = \frac{[\sigma_L^f(z) - \sigma_L^f(-z)] - [\sigma_R^f(z) - \sigma_R^f(-z)]}{[\sigma_L^f(z) + \sigma_L^f(-z)] + [\sigma_R^f(z) + \sigma_R^f(-z)]} = |P_e| A_f \frac{2z}{1+z^2}, \quad (2.3)$$

where  $P_e$  is the longitudinal polarization of the electrons.  $\tilde{A}_{FB}^f$  eliminates the dependence on the initial state, making it possible to measure directly the final state couplings. Furthermore, with a polarization of the electron beams around 73% (as achieved at SLD/SLC [18]), the statistical gain on the sensitivity to  $A_f$  is approximately  $(P_e/A_e)^2 \sim 25$  with respect to the measurement of the unpolarized forward-backward asymmetry  $A_{FB}^f$ . Measuring the  $Z^0$  couplings to fermions is an important precision test of the Standard Model since possible new physics beyond it could manifest itself via radiative corrections to these couplings.

## 2.2 $A_b$ sensitivity to New Physics

---

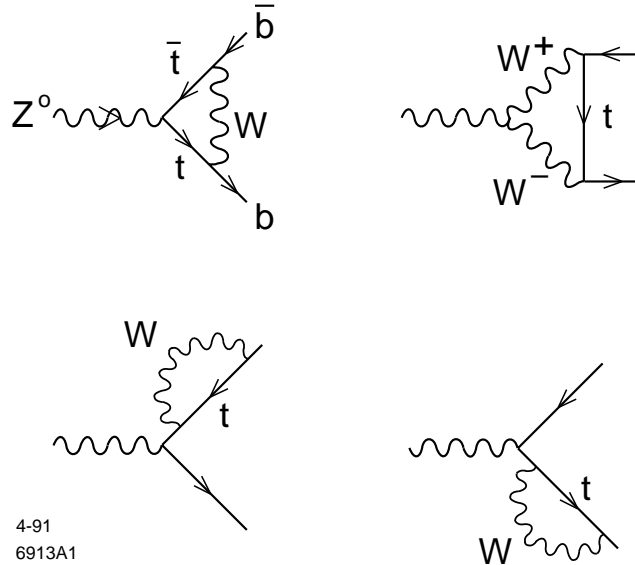


Figure 2.1: Standard Model corrections to the  $Z^0 \rightarrow b\bar{b}$  vertex.

## 2.2 $A_b$ sensitivity to New Physics

Since the coupling asymmetry  $A_f$  is greater for the  $b$  quark than for the  $c$  quark, and  $b\bar{b}$  events are more easily identifiable than  $c\bar{c}$  events, we expect the  $A_b$  measurement to be more precise than  $A_c$  and therefore in this paragraph, we will mostly refer to it.

The two observables  $A_b$  and  $R_b$  completely determine the  $Zb\bar{b}$  vertex through knowledge of the two parameters  $c_V^b$  and  $c_A^b$  (or  $g_L^b$  and  $g_R^b$ ).  $A_b$  in particular is interesting because of its stability, due to the low sensitivity to the center of mass collision energy and to the value of  $\sin^2 \theta_W$ . Moreover,  $A_b$  is also insensitive to the one-loop vertex corrections shown in fig. 2.1. This is due to the fact that  $W^\pm$  bosons only couple to left-handed fermions, whereas  $A_b$  is mostly sensitive to the right-handed coupling. Therefore  $A_b$  proves to be an ideal measurement to probe physics beyond the Standard Model, since any deviations

## 2.2 $A_b$ sensitivity to New Physics

---

from the value predicted by the theory could only be explained as a signal of new physics.

### 2.2.1 Z bosons beyond the Standard Model

Certain models based on more extensive gauge groups [26] predict the existence of further  $Z'$  bosons. Their effect on  $A_b$  could only be relevant if the interaction energy corresponded to the  $Z'$  resonance and the  $Z'$  strongly coupled to both the initial and final states. At the  $Z^0$  pole the interference effect would disappear at the Born level, and only in the presence of a mixing effect between the  $Z'$  and the  $Z^0$  would the  $Z'$  reveal itself through a propagator correction.

### 2.2.2 The Minimal SuperSymmetric Model

The MSSM [27] is an extension to the Standard Model where each SM particle is associated to a supersymmetric partner with the same quantum numbers (but squarks and sleptons have zero spin and gauginos have half-integer spin) and where two Higgs doublets are required to give masses to the up and down like quarks. Corrections to  $R_b$  and  $A_b$  in this model have been calculated by Boulware and Finnell [28].  $A_b$  should not be too sensitive to these, unless the vacuum expectation values of the two Higgs doublets are very different from each other. Letting  $v_1$  and  $v_2$  describe these values, with  $\tan \beta \equiv v_2/v_1$ , if  $v_1 \ll v_2$  the  $b$  quark Yukawa coupling constant  $\lambda_b$  is proportional to  $m_b/\cos \beta \simeq m_b \tan \beta$ , and is therefore relevant in the limit of  $\tan \beta$  being large. In this situation, supersymmetric contributions from the one-loop diagrams shown in fig. 2.2 become important. Two other parameters have to be considered in the  $A_b$  corrections: the  $\mu$  coupling between the two

## 2.2 $A_b$ sensitivity to New Physics

---

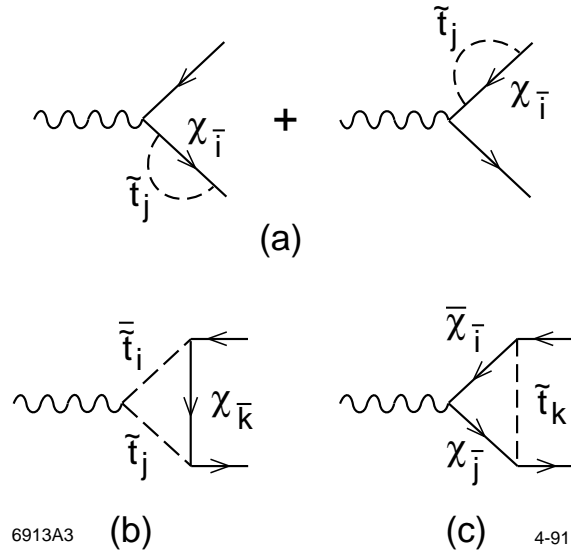


**Figure 2.2:** Diagrams contributing to  $Z^0 \rightarrow b\bar{b}$  in the MSSM model.

Higgs fields and a mass parameter  $M$  of the Wino particle responsible for supersymmetry breaking. The corrections to  $A_b$  as a function of these variables are shown in fig. 2.3.

### 2.2.3 Anomalous couplings

Effects on the  $Z^0$  couplings to the  $b$  quark due to the presence of anomalous electric and magnetic dipole moments have been studied recently [29]. Two further parameters  $\kappa$  and  $\tilde{\kappa}$  have to be added to the Standard Model Lagrangian, which describe the real parts of the form factors of the magnetic and electric dipoles calculated at  $\sqrt{s} = M_z$ . The new Lagrangian would become:

$$\mathcal{L}_{int} = \frac{g}{2 \cos \theta_W} \bar{f} \left[ \gamma_\mu (v_f - a_f \gamma_5) + \frac{i}{2m_f} \sigma_{\mu\nu} q^\nu (\kappa_f - i\tilde{\kappa}_f \gamma_5) \right] f Z^\mu, \quad (2.4)$$

## 2.2 $A_b$ sensitivity to New Physics

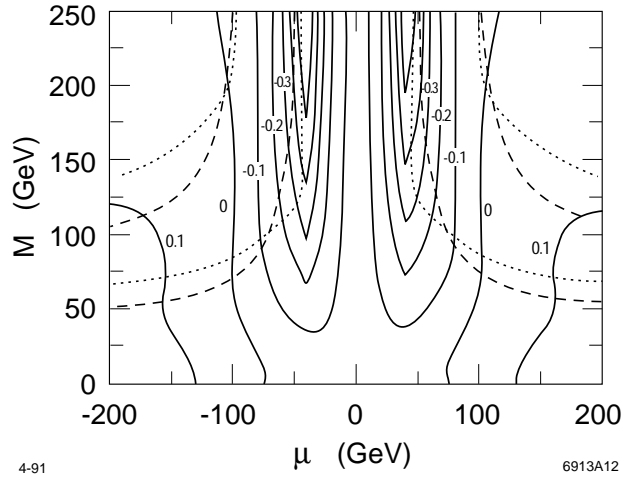


**Figure 2.3:** The contour lines show a hundred times the contribution to  $A_b$  by diagrams with neutralinos, with  $\tan\beta = 70$ .

where  $g$  is the weak coupling constant,  $m_f$  the fermion mass in the final state and  $q$  the  $Z^0$  four-momentum. In the limit  $m_f \ll m_Z$  the polarized cross-section becomes:

$$\frac{d\sigma}{d\cos\theta} \propto (1 - A_e P_e) \left[ 1 + \cos^2\theta + 2(A_e - P_e) \left( A_f + \frac{2\kappa_f a_f}{v_f^2 + a_f^2} \right) \cos\theta + \frac{1}{v_f^2 + a_f^2} \left( \frac{m_Z^2}{4m_f^2} (\kappa_f^2 + \tilde{\kappa}_f^2) \sin^2\theta + \kappa_f^2 + \tilde{\kappa}_f^2 + 4v_f \kappa_f \right) \right] \quad (2.5)$$

and the value for  $A_b$ :

$$A_b = \frac{2(v_b a_b + \kappa_b a_b)}{v_b^2 + a_b^2 + \frac{3}{4} \left( \frac{m_Z^2}{4m_b^2} (\kappa_b^2 + \tilde{\kappa}_b^2) + \kappa_b^2 + \tilde{\kappa}_b^2 + 4v_b \kappa_b \right)}. \quad (2.6)$$

Non-zero values of  $\kappa_b$  and  $\tilde{\kappa}_b$  have been found to push the Standard Model predictions for  $A_b$  closer to the data (by lowering its value) but the statistics available was not sufficient to make a claim for new physics.

## 2.3 Measuring the Forward-Backward Asymmetry

For the reasons advanced at the beginning of this chapter, we will focus here on the  $A_b$  measurement and the phenomenology of  $b\bar{b}$  events:  $A_c$  will only play a secondary role in this analysis.

Measuring the left-right forward-backward asymmetry can be essentially broken down in three steps:

1. identifying  $e^+e^- \rightarrow Z^0 \rightarrow b\bar{b}$  events;
2. measuring the angle  $\theta$  of the  $b$  quark and/or the  $\bar{b}$  (which has the opposite asymmetry to the  $b$  quark) for each of these events;
3. combining the angles measured from many events and fitting them to the asymmetry function  $\tilde{A}_{FB}^f(\theta)$ .

Step (2) is complicated by hadronization and final state radiation. When the  $Z^0$  decays into  $b\bar{b}$ , the two quarks, through hadronization, combine into two  $B$  hadrons, followed by lighter and lower momentum hadrons which together form particle *jets*. QCD final state radiation (gluons) and groups of hadrons that are given large transverse momentum during hadronization can form other jets in an event.

Due to the complexity of this topology, it is important to develop special strategies for measuring the  $b$  or  $\bar{b}$  quark direction. If an analysis method identifies the  $B$  hadron, its direction can be used as a good approximation to the quark direction, as long as it is possible to determine whether the  $B$  hadron contains a  $b$  or  $\bar{b}$  quark. Otherwise, if the method can identify the jet that contains the  $B$  hadron, then the jet direction can be used

### 2.3 Measuring the Forward-Backward Asymmetry

---

as the quark direction, again assuming that  $b$  and  $\bar{b}$  jets can be distinguished. Finally, if the method uses some global event quantity that does not distinguish jets, then the *thrust axis* (the average direction of the momentum flow in an event) can be used. Although this is often a poor approximation to the quark direction, its error can be well modelled and accounted for.

Different techniques have been used at SLD to measure the coupling asymmetries  $A_b$  and  $A_c$  respectively, based on the identification of kaons from  $B \rightarrow D \rightarrow K$  decays, jet charge and vertex charge reconstruction (for  $A_b$ ), on the exclusive reconstruction of  $D^+$  and  $D^{*+}$  mesons, the identification of soft pions from  $D^{*+} \rightarrow D^0 \pi^+$  decays and a fully inclusive method (for  $A_c$ ), and finally on the identification of semileptonic  $B$  and  $D$  decays (for both). Here is a brief description of these techniques.

#### 2.3.1 The Jet Charge Method

This method is based upon the fact that since  $b$  quarks have negative charge, (as opposed to their antiquarks), the sum of track charges in the  $b$  hemisphere is on average smaller than that in the opposite hemisphere (see fig. 2.4).

$b\bar{b}$  events are selected with the requirement that the event contain at least one secondary vertex with mass greater than 2 GeV/ $c^2$ . Using all charged tracks, the two quantities  $Q_{sum}$  and  $Q_{diff}$  are formed [30]:

$$Q_{sum} = \sum_{tracks} q_i |(\vec{p}_i \cdot \hat{T})|^\kappa, \quad (2.7)$$

$$Q_{diff} = - \sum_{tracks} q_i \cdot sgn(\vec{p}_i \cdot \hat{T}) |(\vec{p}_i \cdot \hat{T})|^\kappa, \quad (2.8)$$

where  $q_i$  and  $\vec{p}_i$  are the charge and momentum of track  $i$  respectively and  $\hat{T}$  is a unit

### 2.3 Measuring the Forward-Backward Asymmetry

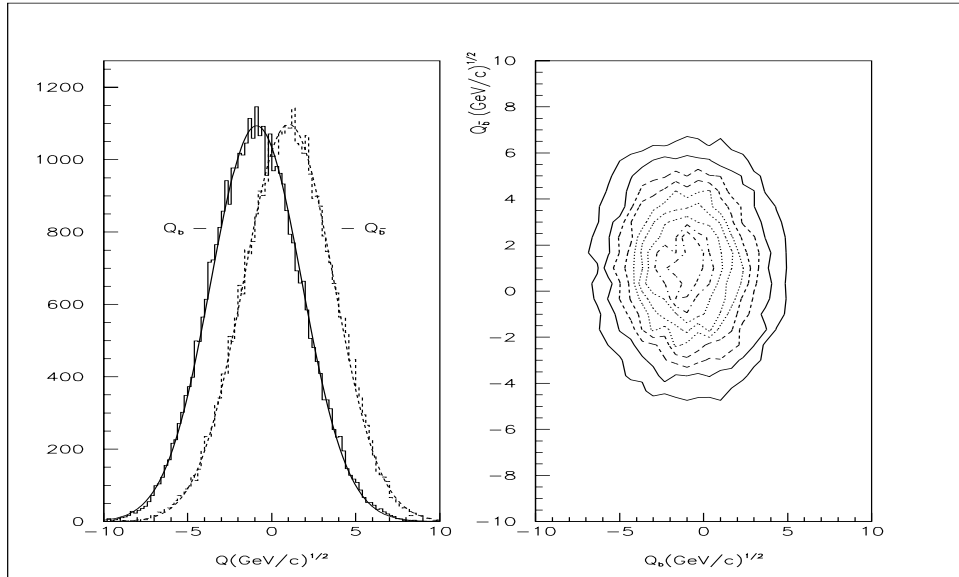


**Figure 2.4:** In the left plot histograms of  $Q_b$  and  $Q_{\bar{b}}$  (from Monte Carlo) and Gaussian fits are shown. In the right one is the contour plot of the  $Q_b$ ,  $Q_{\bar{b}}$  joint distribution.

vector chosen along the direction of the reconstructed thrust axis so that  $Q_{diff} > 0$ . The vector  $\hat{T}$  is therefore an estimate of the  $b$ -quark direction. For  $\kappa = 0$ ,  $Q_{diff}$  is simply the sum of the charges of all tracks and is dominated by tracks at low momenta produced by hadronization; for large  $\kappa$ , only tracks at high momenta (mostly coming from the  $B$  decay) contribute. Since on the other hand some low momentum tracks can carry most of the information about the primary quark charge, one needs to tune the parameter  $\kappa$ : the value assumed for this analysis is  $\kappa = 0.5$ . The probability that the sign of  $Q_{diff}$  accurately reflects the charge of the underlying quark is estimated directly from the data (*self-calibrated technique*), by defining two quantities  $Q_b$  and  $Q_{\bar{b}}$  as the unsigned momentum-weighted jet-charge sum of the tracks in the two hemispheres containing the  $b$  and  $\bar{b}$  quarks respectively:

$$Q_b = \frac{1}{2}(Q_{sum} + Q_{diff}) \quad Q_{\bar{b}} = \frac{1}{2}(Q_{sum} - Q_{diff}) \quad (2.9)$$

## 2.3 Measuring the Forward-Backward Asymmetry

---

The dependence on Monte Carlo is thus reduced to the correlation between the two hemispheres (of the order of 2.5% [30]), which is mainly due to charge conservation in the event. The main advantage of this method is that all  $b\bar{b}$  events can be used, with evident statistical gain.

### 2.3.2 The Vertex Charge Method

The determination of the sign of the quark is here done using the reconstructed vertex charge  $Q_{vtx}$  [31]. Only hemispheres with an invariant mass above 2 GeV/ $c^2$  and  $Q_{vtx} \neq 0$  are considered. Because the  $b$  quark is negatively charged, a quark hemisphere is indicated by  $Q_{vtx} < 0$ . Only the sign of the charge is used, the magnitude is ignored; double-tagged events with disagreeing hemispheres are discarded. The probability to correctly reconstruct the sign of the charge is increased by the use of a new technique of *VXD-only tracking* whereby vectors with more than 3 hits in the vertex detector and that have not been linked to the drift chamber are used along with fully reconstructed tracks. This enhances the probability for a correct  $Q$  to about 85% [31]. The purity of the tag is calibrated from the double-tag rate (fraction of double-tagged events that are in agreement) while the analyzing power (effectiveness of the quark/antiquark tag) is given by the opposite-sign rate. Latest values are  $\Pi = 0.96$  and  $AP = 0.65$  respectively [31].

This is so far the most precise technique at SLD for the  $A_b$  measurement.

## 2.3 Measuring the Forward-Backward Asymmetry

---

### 2.3.3 $A_b$ with a kaon tag

This technique uses kaon tracks identified with information from the Čerenkov detector to select  $b \rightarrow c \rightarrow s$  decay chains and separate  $B$  from  $\bar{B}$  [32]. Two flavour tags are defined. A heavy tag is defined for hemispheres with an invariant mass above 2 GeV/ $c^2$ ; the intermediate mass region, between 0.5 and 2 GeV/ $c^2$  contains a mixture of  $b$  and  $c$ , where the  $b$  part is largely  $B$ 's which decay so quickly that the tracks from the  $W$  are lost, so only the  $D$  tracks are left. Because the cascade K's are among these tracks, these vertices are useful too, and a light tag is defined for hemispheres with vertices not passing heavy tag cuts. Efficiencies for both tags are found by comparing the single  $vs$  double-tagged event rates.  $b\bar{b}$  events are selected by requiring at least one heavy-tagged hemisphere.

The determination of the direction of the quark is done using the kaon charge  $Q_K$ , that is the total charge of the CRID-identified kaon tracks in the vertex. Because of the cascade nature of the tag the signals for  $b \rightarrow c \rightarrow s$  and  $c \rightarrow s$  have the same sign, which reduces sensitivity to the  $c$  background fraction. A hemisphere with two oppositely-charged K tracks is considered uncharged, for a total tag efficiency of  $\sim 25\%$  [32].

The probability to correctly discriminate between quark/antiquark is calibrated from the data, by using events with both hemispheres  $b$ -tagged (at least one heavy) and with non-zero charge in each hemisphere. We find  $p^{corr} = 70.7 \pm 1.4\%$  to be compared with a Monte Carlo prediction of 72.4% [32].

## 2.3 Measuring the Forward-Backward Asymmetry

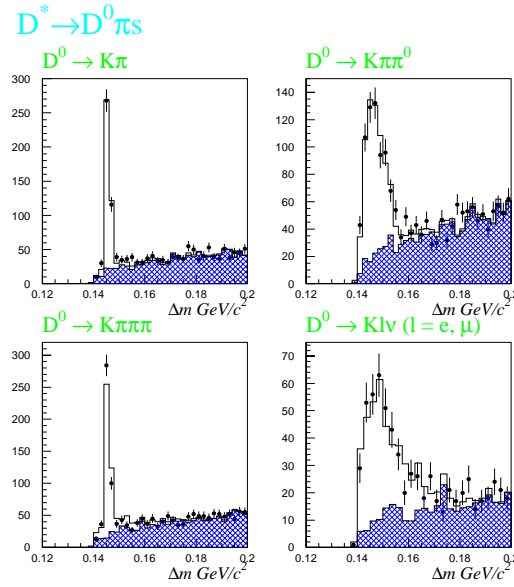


**Figure 2.5:** The mass-difference distributions for the channel  $D^{*+} \rightarrow D^0 \pi^+$  for the four  $D^0$  decay modes. The solid circles indicate the experimental data and histograms are MC signal (open) and Random Combinatoric Background (double hatched).

### 2.3.4 $A_c$ with exclusive charmed mesons reconstruction

Six different decay modes are reconstructed in this method [33], four from the  $D^{*+} \rightarrow D^0 \pi^+$  chain, followed by the  $D^0$  decaying into the  $K^- \pi^+$ ,  $K^- \pi^+ \pi^-$ ,  $K^- \pi^+ \pi^+ \pi^-$  and  $K^- l^+ \nu$  channels respectively, and two other decay modes from  $D^+ \rightarrow K^- \pi^+ \pi^-$  and  $D^0 \rightarrow K^- \pi^+$  (see fig. 2.5).

A  $b$ -tag veto, consisting in the rejection of events with a vertex having invariant mass greater than  $2 \text{ GeV}/c^2$ , exploits the optimal performance of the mass-tag used in the  $B$  physics sector to actually reject 57% of  $b\bar{b}$  events while preserving 99% of  $c\bar{c}$  events. Kinematic and event topology information are combined to further reject  $b$  and  $uds$  background, by using cuts on  $x_D$  (fraction of the beam energy carried by the  $D$  meson) and on the  $xy$  impact parameter of the  $D^0$  momentum vector w.r.t the IP (to reject

### 2.3 Measuring the Forward-Backward Asymmetry

---

$D$  decays in  $b\bar{b}$  events, since these  $D$ 's have significant  $p_T$  relative to the  $B$  parent flight direction and do not appear to originate from the IP). Finally cuts on the mass difference  $\Delta M = M_{D^*} - M_{D^0}$  are applied to select the signal events in the peak, while the sideband regions are used to estimate combinatorial background in the signal region and its asymmetry.

The charge of the quark is given by the sign of the  $D^*$  (or  $K^-$ ), while the quark direction is approximated by the  $D$  meson direction.

This analysis has a very low reconstruction efficiency ( $\sim 4\%$ ), but benefits from a high correct sign probability, a good determination of the underlying  $c$  quark direction and low systematic errors.

#### 2.3.5 $A_c$ analysis with inclusive soft pions

In this analysis [33],  $c$ -quarks are identified by the presence of soft pions from the decay  $D^{*+} \rightarrow D^0 \pi_s^+$ . Since this decay has a small Q value of  $m_{D^*} - m_{D^0} - m_\pi = 6 \text{ MeV}/c^2$ , the maximum transverse momentum of  $\pi_s$  with respect to the  $D^{*+}$  flight direction is only 40 MeV/c, i.e. the  $\pi_s$  is typically produced along the  $D^*$  jet flight direction ( $p_t \sim 0$ ).  $b\bar{b}$  events are rejected with the same criteria described for the exclusive  $D^*$  analysis. After identifying the  $D^{*+}$  candidates, soft-pions with momentum  $p$  between 1 and 3 GeV/c (to reject soft pions from  $b\bar{b}$  events, which have a lower momentum), and with an impact parameter  $< 2\sigma$  from the IP (to reject pions decaying from a  $D$  in a  $b\bar{b}$  cascade event) are selected. The pion transverse momentum  $p_t$  to the jet axis is calculated and the signal region is defined for  $p_t^2 < 0.01 \text{ GeV}^2/c^2$ , where a signal-to-background ratio

## 2.3 Measuring the Forward-Backward Asymmetry

---

of 1:2 is observed. The MC signal and background shapes are fitted to two functions and the relative normalization of the two is estimated by applying this fit to the data. The direction of the primary quark is derived from the jet axis and the charge of the primary  $c$ -quark is determined by the charge of the  $\pi_s$ .  $A_c$  is then extracted using an unbinned maximum likelihood fit, assuming the background asymmetry to be consistent with zero.

### 2.3.6 $A_c$ with inclusive charm tagging

This measurement uses a vertex tag technique, where the selection of a  $c$  hemisphere is based on the reconstructed mass and momentum of the charm hadron decay vertex [34]. A charm tag is defined by requiring:  $0.55 < M_{vtx} < 2 \text{ GeV}/c^2$ ,  $P_{vtx} > 5 \text{ GeV}/c$ ,  $15M_{vtx} - P_{vtx} < 10$  (fragmentation cut, which uses the fact that  $D$  hadrons from direct charm have a higher momentum than those from  $B$  hadron decays to reject  $b\bar{b}$  events in the low mass region). A charm event is defined to be one with at least one charm-tagged hemisphere and no bottom tagged hemisphere ( $M_{vtx} > 2 \text{ GeV}/c^2$ ), which gives an efficiency of  $\sim 28\%$  and a purity of  $\sim 83\%$ . There are two methods to determine the charge of the quark, from the vertex charge or the kaon charge. In the first case one uses the fact that the charge is positive for  $c$  vertices and negative for  $\bar{c}$  vertices. In the second case one uses the total charge of the CRID-identified kaon tracks in the vertex. Efficiency is  $\sim 25\%$  for the kaon tag and  $\sim 50\%$  for the vertex charge. A hemisphere is considered charged if it has either tag nonzero, but hemispheres with the two tags in disagreement are considered uncharged. The probability to correctly reconstruct the quark charge is calibrated from the data by using events with both hemispheres charm-tagged and nonzero charge in

## 2.3 Measuring the Forward-Backward Asymmetry

---

each hemisphere. We find  $p^{corr} = 94.2 \pm 1.2\%$  [34]. A maximum likelihood fit is used to determine  $A_c$ , using the thrust axis as an estimate for the quark direction.

### 2.3.7 Measurement of $A_b$ and $A_c$ with identified leptons

This last technique is the object of the present thesis and will be discussed in more details in the following chapters. The fundamental idea is that muons and electrons can be used to identify  $b\bar{b}$  and  $c\bar{c}$  events, once they are separated from the sources of background, mainly leptons coming from light quark decays or electron-positron pairs produced by high energy photon interactions with the detector material. The latter ones can be easily distinguished because they typically originate far from the IP and the four-momentum sum of each pair has zero invariant mass. Leptons from light quarks are separated using kinematic information (total and transverse momenta) and topological information (mass of the reconstructed secondary decay vertex).

Since  $B$  ( $D$ ) hadrons decay semileptonically only in  $\sim 22\%$  (20%) of the cases, this method suffers from statistical loss and furthermore requires a certain understanding of the detector for lepton identification; its main advantage lies in the fact that theoretical uncertainties are limited to the momentum spectrum of  $B$  and  $D$  hadronic decays and to the  $b$  and  $c$  quarks hadronization. It is therefore necessary that the Monte Carlo simulation describes very accurately the lepton momentum spectra, in order to associate them correctly to their decay sources (see Chapter 4).

# Chapter 3

## The Experimental Apparatus

### 3.1 The Stanford Linear Collider

The Stanford Linear Collider (SLC) was originally conceived as a quick and relatively inexpensive way of adapting a pre-existing accelerator in order to produce  $Z^0$  particles before LEP started to be operational [35]. In fact, its rather unconventional design (as compared to the more common technology of storage rings) presented many more problems than expected, and as a consequence, the machine came into function years after schedule and initially with a much smaller luminosity than designed. It was only in the latest 1997-1998 run that the design operating conditions were met and that SLC, as the only high energy  $e^+e^-$  linear collider, proved to be a major achievement in particle accelerator technology and a test bed for new advancements in the field.

At SLC bunches of electrons and positrons have only one chance to collide per cycle, at a rate of 120 Hz as compared to the millions of times per second at LEP; the key features

## 3.1 The Stanford Linear Collider

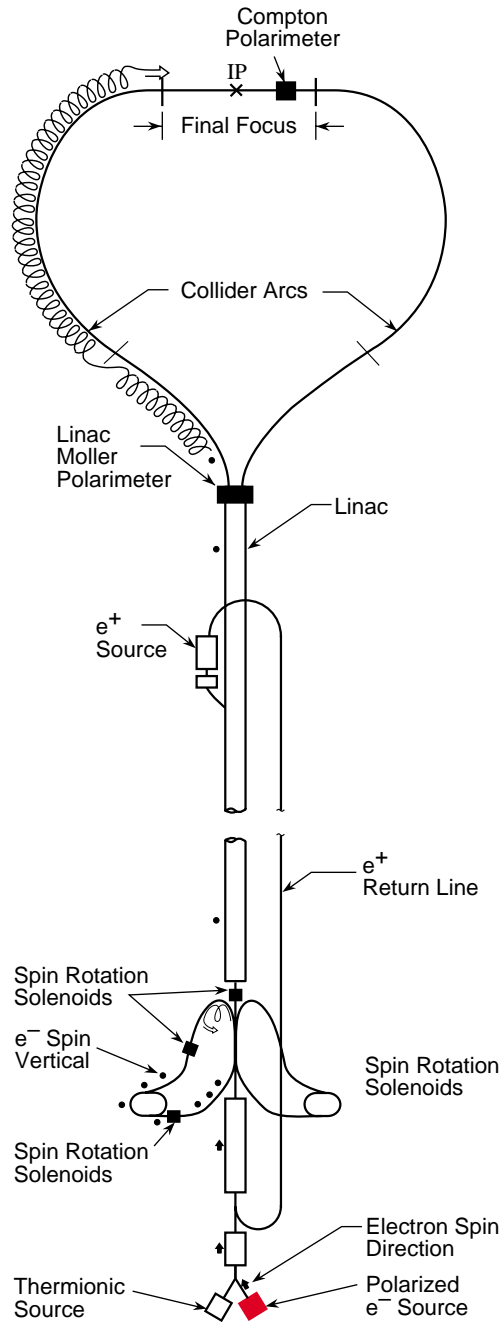


**Figure 3.1:** Scheme of the SLC accelerator.

### 3.1 The Stanford Linear Collider

---

that make SLC competitive are essentially two:

1. the possibility to produce polarized electron beams,
2. the tiny dimensions of the beams in the interaction region.

The layout of the SLC is shown in fig. 3.1. We can distinguish:

- the polarized electron source;
- a first accelerating sector that brings the particles to an energy of 1.2 GeV;
- two small storage rings that are used to damp the beam phase-space to suitable dimensions;
- the pre-existing linac;
- the positron source;
- two long arcs of magnets that are used to separate and transport the electron and positron beams to a single interaction point;
- and finally an elaborate focusing system that reduces the sizes of the beams before their collision.

At the beginning of the machine cycle, two bunches of polarized electrons are produced by photo-emission from a strained gallium arsenide cathode hit by circularly polarized laser light and they are injected into the linac [36]. The linear accelerator (*linac*) is a two miles long sequence of conventional copper wave-guides driven by eight 60 MWatt peak power 2856 MHz RF klystrons. The microwaves produced by the klystrons create an alternating

### 3.1 The Stanford Linear Collider

---

field in the cavities, which is in phase with the passage of the electrons (out of phase in case of the positrons). These particles receive an acceleration along the linac with a gradient of 17 MeV/m, which eventually produces a single beam energy of up to 50 GeV. After receiving a preliminary acceleration to 1.2 GeV, the electron bunches enter into the North Damping Ring, where their transverse emittance (the phase space they occupy) is reduced in order to increase the luminosity [37] and obtain micron-size beams at the IP. It is in the *damping rings* that beams are made flat: without any coupling between the oscillations in the two transverse dimensions, stable orbits in a horizontal ring are expected to occupy a larger region in the horizontal direction than in the vertical one. At the IP the relative ratio is around 4.6:1 [38]. After 8.3 ms of damping they are extracted from the NDR and re-injected, together with the positron bunch coming from the South Damping Ring, into the main section of the accelerator. About two thirds of the way down the linac, the trailing electron bunch is stripped off and directed against the positron generator target, a thick piece of tungsten-rhenium alloy used for pair production [39]. Positrons are filtered out of the resulting shower with an electric field and brought back to the front part of the linac, where they are injected into the SDR and stored for two cycles of the machine. The other two bunches (electron and positron) are accelerated up to 46.5 GeV approximately and separated in the beam switch yard, where they enter the North and South arcs respectively. Here they are subjected to a dipole magnetic field which bends the beams with a 280 m effective radius in such a way to minimize the energy loss due to synchrotron radiation (this amounts to  $\sim 1$  GeV) [40]. The final 114 m section of the arcs is basically straight, and contains the SLC final focus, where the two beams are further compressed

### 3.1 The Stanford Linear Collider

---

and focused for collisions through a rather complex apparatus of magnetic lenses <sup>1</sup>. Once every 1800 beam crossings or so, an electron (one of the  $3 \times 10^{10}$  in a bunch) interacts with a positron to produce a  $Z^0$  particle.

Machine backgrounds are mainly of two types: electrons and positrons produced by synchrotron radiation (via high energy photons scattering against atomic electrons in the pipeline or in the detector itself), which generally leave spiralling tracks in the inner part of the detector because of their low energy, and accelerator muons produced via the *Bethe-Heitler* [41] mechanism, which travel parallel to the beams. This background can be reduced with the use of collimators.

#### 3.1.1 Luminosity

The SLC luminosity has been steadily increasing since 1993 until reaching, during the last run, roughly half its design value ( $L = 6 \times 10^{30} \text{ cm}^{-2} \text{ sec}^{-1}$  [42]). In the 1993-1996 runs a total integrated luminosity of  $7.0 \text{ pb}^{-1}$  was obtained, to be compared with one of  $12 \text{ pb}^{-1}$  in the 1997-1998 final run, which is nearly double the previous data sample. The improvement in the performance is mostly due to changes in the tuning procedures and to some hardware upgrades, in particular optics for correcting chromatic aberrations in the final focus and RF techniques for achieving small emittance in the damping rings.

The luminosity  $L$  is given by :

$$L = \frac{N^+ N^- f}{4\pi \sigma_x \sigma_y} H_d, \quad (3.1)$$

---

<sup>1</sup>The typical widths for a flat beam configuration at the IP is  $\sim 2 \mu\text{m}$  by  $< 1 \mu\text{m}$  ( $x, y$ ).

### 3.1 The Stanford Linear Collider

---

<i>Parameter</i>		<i>1993</i>	<i>1994-95</i>	<i>1996</i>	<i>1997-98</i>
Horizontal beam size	$\sigma_x(\mu m)$	2.6	2.1	2.0	1.7
Vertical beam size	$\sigma_y(\mu m)$	0.8	0.6	0.8	0.9
Horizontal divergence	$\theta_x(\mu rad)$	300	300	370	460
Vertical divergence	$\theta_y(\mu rad)$	200	200	260	260
Energy spread	$\sigma_E/E(\%)$	0.30	0.12	0.16	0.13
Bunch intensity	$n_{e\pm}(10^{10})$	3.0	3.5	3.5	3.5
Electron polarization	$P_e(\%)$	63.0	77.2	76.5	73.2
Integrated luminosity	$L_{int}(pb^{-1})$	1.6	3.5	1.9	12.1
Total integrated luminosity	$L_{tot}(pb^{-1})$	1.6	5.1	7	19.1
Number of hadronic $Z^0$	$N_Z$	50k	100k	50k	350k

**Table 3.1:** Typical beam parameters at the SLC IP for the different running periods. Sizes and divergences are given as single bunch RMS values; the beam polarization is luminosity weighted over each running period.

where  $N^\pm$  are the number of electrons and positrons at the interaction point,  $f$  is the collision rate,  $\sigma_{x,y}$  are the average horizontal and vertical beam sizes, and  $H_d$  is the disruption enhancement factor which depends on beam intensities and sizes. (A significant disruption effect was found in the last run, which is due to the fact that when beams collide, each beam is focused by the field of the other beam, causing the transverse size to shrink.  $H_d$  was measured to be as large as 2. [43]) Since the current is limited by instabilities to be around  $3.5 \times 10^{10}$  particles per bunch, the luminosity can only be improved by reducing the beam emittance  $\epsilon$  and increasing the angular divergence  $\theta$  at the IP ( $\sigma_{x,y} = \epsilon_{x,y}/\theta_{x,y}$ ). Permanent sextupoles were therefore installed in the linac, and permanent octupoles were added to the final focus optics in February 1998. Table 3.1 lists some of the beam parameters for the different runs, and fig. 3.2 shows the integrated luminosity per run and the luminosity per week.

### 3.1 The Stanford Linear Collider

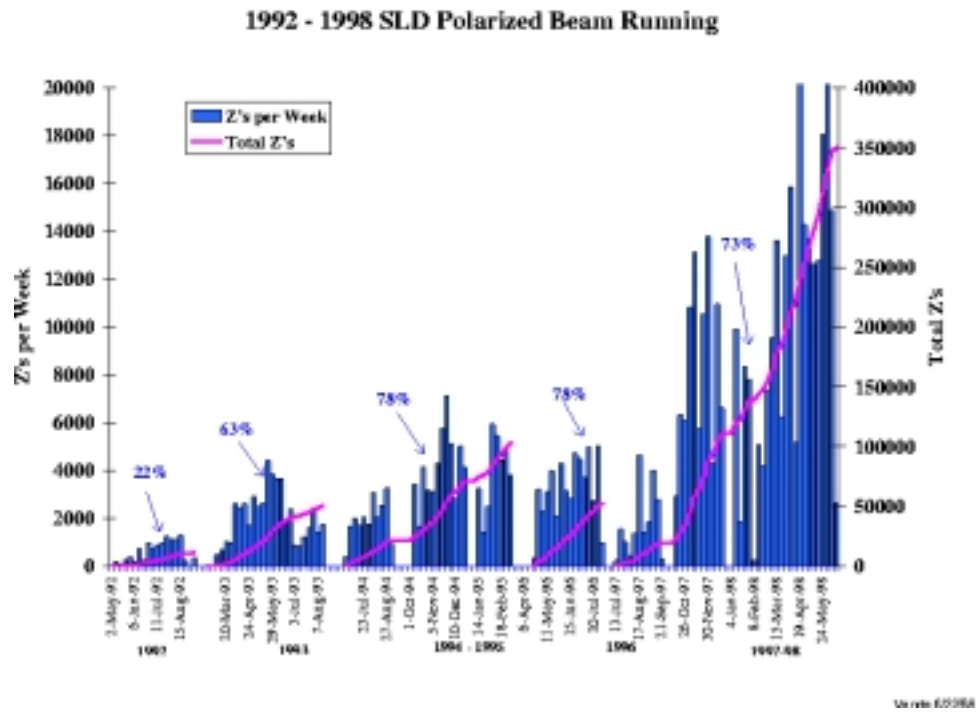


**Figure 3.2:** Luminosity history over all SLD runs. The histogram shows the accumulated events per week, while the solid curve shows the integrated luminosity. The average polarization values are also shown.

### 3.1 The Stanford Linear Collider

---

#### 3.1.2 Polarized Electron Source

Polarized electrons are produced at SLC by photo-emission from the surface of a strained-lattice GaAs cathode when hit by a circularly polarized laser beam [44]. Fig. 3.3 shows the GaAs band structure, with the energy levels at the top of the valence band and the bottom of the conduction band. A circularly polarized photon near the band gap energy of 1.52 eV will excite a transition. In conventional GaAs, two transitions producing opposite spin electrons are possible from the degenerate  $P_{3/2}$  energy level at a rate of 3 to 1 as given by the Clebsch-Gordon coefficients; this allows for a maximum longitudinal polarization of 50%. By growing a thin layer of GaAs on top of a substrate of GaAsP, a mechanical strain is applied which breaks the crystal symmetry and the energy levels degeneracy so that higher polarizations can be achieved. The relative thickness of the various cathode layers has a significant effect on the performance of the source (due to rescattering of the electrons in the active material). By reducing the active layer from 300 nm to 100 nm in 1994, the average polarization increased from 63% in 1993 to 77% in 1994. Also, the quantum efficiency of the cathode degrades in time so that it is necessary to apply a thin layer of caesium every 3 to 4 days in order to reduce the work function of the surface.

The wavelength of the laser is set around 860 nm to maximize the polarization of the produced electrons. By reversing the helicity of the polarized light, the helicity of the electrons is inverted too: during SLC running the polarization of the incident photons is selected by a pseudo-random sequence on each machine cycle in order to average out any periodic effects in the accelerator performance. Fig. 3.4 shows the setup at the electron

## 3.1 The Stanford Linear Collider

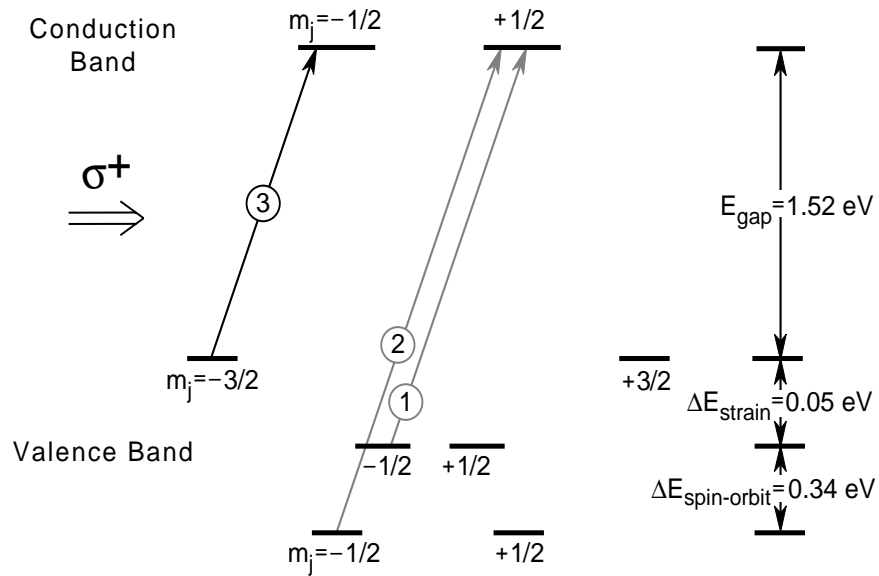


**Figure 3.3:** Energy levels of the valence and conduction bands for strained GaAs. The Clebsch-Gordon coefficients for the various spin transitions in the case of a right-handed incident photon are also shown. In bulk GaAs, spin-orbit interactions separate the  $P_{1/2}$  and  $P_{3/2}$  energy levels to provide a maximum polarization of 50%. With a strained lattice, the degenerate  $P_{3/2}$  can also be separated and a polarization of nearly 100% can be achieved.

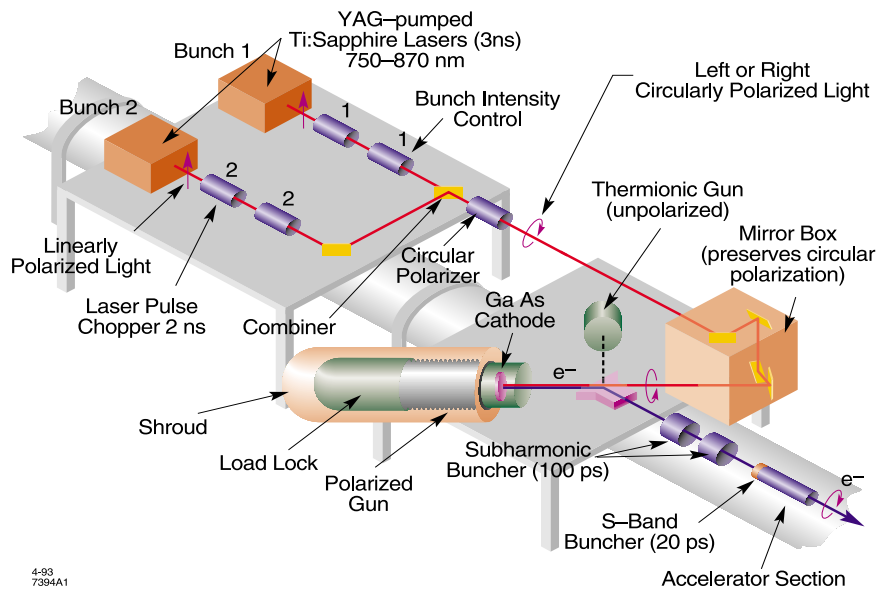


**Figure 3.4:** The polarized source optical system.

### 3.1 The Stanford Linear Collider

---

source.

#### 3.1.3 Spin transport

Special care must be taken to avoid any polarization losses when the electron bunches enter the north damping ring. In a magnetic field, the spin precession of a relativistic particle is described by:

$$\frac{d\theta_{spin}}{d\theta_{bend}} = \gamma \frac{g-2}{2} \quad (3.2)$$

where  $\theta_{bend}$  is the bend angle,  $\theta_{spin}$  is the precession angle of the component of the spin vector perpendicular to the magnetic field with respect to the momentum vector, and  $\gamma = E/m$ . Consequently any polarization component lying in the bend plane is averaged out to zero. To avoid that, the electron spin needs to be aligned with the magnetic field upon entering the damping ring, initially through a rotation that brings  $s_z$  to  $s_x$ , followed by a second rotation that brings  $s_x$  to  $s_y$  (vertical axis). As soon as the electrons are extracted from the damping ring, their polarization is brought back along the momentum direction.

Unfortunately the SLC arcs are not flat, but they follow the bumps in the surrounding terrain; as a consequence, the bending magnetic fields are not all vertical and parallel to each other, and therefore the electron spin precession does not occur around a unique axis. In particular, the final orientation of the spin vector at the interaction point depends on the trajectory followed inside the arcs so that one can choose an ideal orbit which maximizes the longitudinal component of the polarization in the collision region [45].

### 3.1 The Stanford Linear Collider

---

#### 3.1.4 Polarimetry

A Compton polarimeter [46], located 33 m downstream from SLD, is the main instrument in measuring the electron beam polarization. A circularly polarized 2.33 eV photon beam is scattered off the exiting 45.6 GeV electron bunch; due to their large boost, the scattered electrons remain with the main outgoing beam until they reach the first series of magnets of the SLC South Arc. These introduce a momentum dependent kink in the trajectories of the electrons, which are thus swept off the SLC beam line, into a Compton Čerenkov Detector (CKV).

The polarization measurement uses the difference in the Compton scattering cross sections in the cases when the electrons and photons collide with their polarization vectors aligned (forming a  $J_z = 3/2$  spin state) or opposed (forming a  $J_z = 1/2$  spin state). This difference is reflected in an asymmetry in the energy spectrum of the scattered electrons which is given by :

$$A_C^i = |P_e||P_\gamma|a^i, \quad (3.3)$$

where  $P_e$  is the longitudinal electron polarization,  $P_\gamma$  is the photon circular polarization and  $a^i$  is the analyzing power of each CKV channel.

Data from the Compton polarimeter is acquired continuously during normal SLC operation. A  $\sim 1 - 3\%$  statistical level polarization measurement takes about three minutes to complete. Each hadronic event is therefore associated with a time weighted polarization value which is given by the average of the single polarization measurements taken within an hour of the hadronic event, with a weight provided by a Gaussian function acting as

### 3.1 The Stanford Linear Collider

---

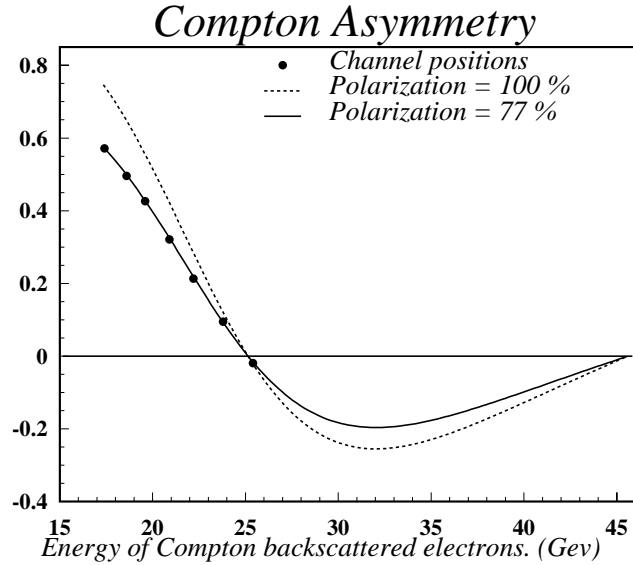


**Figure 3.5:** The Compton asymmetry versus the energy of the backscattered electrons is shown for 100% and 77% polarization [47].

1992	$P_e$	=	0.224	$\pm$	0.006
1993	$P_e$	=	0.626	$\pm$	0.012
1994-95	$P_e$	=	0.772	$\pm$	0.005
1996	$P_e$	=	0.765	$\pm$	0.005
1997-98	$P_e$	=	0.729	$\pm$	0.004

**Table 3.2:** Luminosity weighted polarization results [47].

a time filter in giving more weight to measurements that are closer in time to the event. The arithmetic average of all such Gaussian weighted polarization results forms the luminosity weighted polarization average, whose values for the different run periods are listed in table 3.2.

#### 3.1.5 Energy Spectrometer

The beam energy at SLC is measured on every machine pulse with a pair of spectrometers located in the extraction lines just before the beam dumps [48]. The vertical

### 3.2 The SLC Large Detector

---

separation between the synchrotron light swaths emitted by the beam in passing through the magnets (inversely proportional to the energy of the beam) is measured by a wire imaging synchrotron radiation detector (WISRDR). The uncertainty on a single beam measurement is around 22 MeV; averaging over many beam pulses and taking into account the correlations between the two detectors results in a 25 MeV total error on the center of mass collision energy at SLD. The luminosity weighted values for the 1993 and 1994-98 years were measured to be  $(91.26 \pm 0.02)$  GeV and  $(91.28 \pm 0.02)$  GeV respectively.

### 3.2 The SLC Large Detector

The SLC Large Detector (SLD) was built for studying high precision physics at the  $Z^0$  boson resonance through the full reconstruction of recorded events [49]. An isometric view is shown in Fig. 3.6 and a quadrant view in Fig. 3.7. The SLD coordinate system is defined in spherical coordinates  $\theta$  and  $\phi$ , centered on the IP, where  $\theta$  is the angle from the plane perpendicular to the beam axis (which lies along the  $z$  direction) and  $\phi$  is the angle from the horizontal. Positive  $\theta$  is in the direction of the electron beam.

Different subsystems provide simultaneous measurements of charge, momentum, energy and species of the observable particles created by the decay of a  $Z^0$ :

- a luminosity monitor (LM) [63], which measures small angle Bhabha scattering rates and derives the luminosity from the Bhabha cross section;
- excellent resolution vertex detectors (VXD2 and VXD3) [50] [51];
- a drift chamber (DC) [53], to reconstruct charged track trajectories and momenta in

### 3.2 The SLC Large Detector

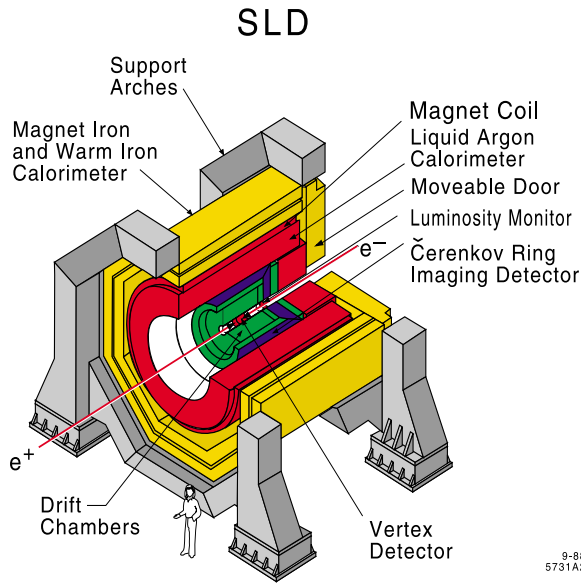


**Figure 3.6:** Isometric view of the SLD detector, with the endcaps removed for clarity.

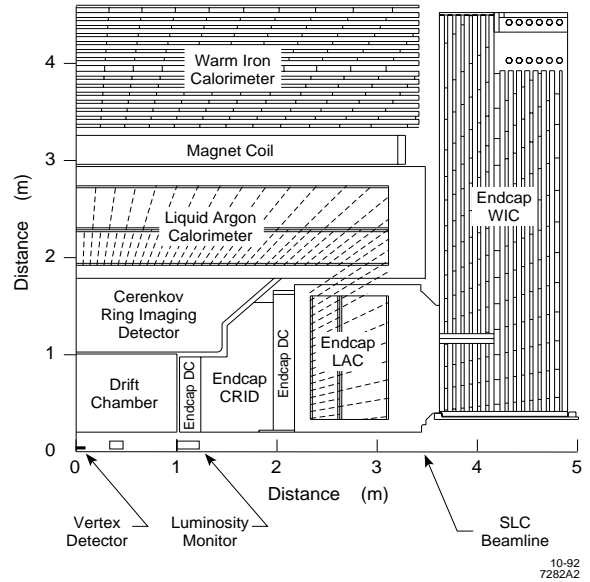


**Figure 3.7:** Quadrant view of the detector with the IP in the bottom left corner. The detector is both radially and longitudinally symmetric.

a 0.6 Tesla magnetic field provided by a Magnetic Coil;

- a Čerenkov Ring Imaging Detector (CRID) [56], for particle identification;
- a Liquid Argon Calorimeter (LAC) [59], for hadronic and electromagnetic calorimetry;
- a Warm Iron Calorimeter (WIC) [61], which serves as a magnetic flux return, a particle detector for muons and for catching the hadronic energy tails.

The detector provides an almost full solid angle coverage around the interaction point in every component, and it can be divided into a central part with cylindrical symmetry and octagonal basis (*barrel*) and two lateral parts for small angle coverage (*endcaps*). In this chapter we will give an overview of the different sub-detectors, placing particular emphasis

## 3.2 The SLC Large Detector

---

on the vertex detector, the CRID and the WIC, as these systems are critical to the analysis described in this thesis.

### 3.2.1 The Vertex Detectors

The vertex detector performance has proved to be crucial for the physics done at SLD; in particular the small dimensions of the SLC beam pipe made it possible for it to be placed at a starting radius of 25 mm from the beam axis, therefore giving the opportunity to extrapolate charged tracks coming from the IP or from secondary decay vertices with very high precision and to fully reconstruct the particles decay sequence, even for very short-lived ones.

Two vertex detectors have been used in data-taking at SLD: VXD2 (1992-95) [50] and its upgraded version VXD3 [51] (1996-98). Both are Charged-Coupled Devices (CCD) based detectors, designed to provide high vertexing resolution (CCDs are used as the medium for detecting the deposition of ionization from charged particles passing through the devices). They are housed in a low-mass cryostat and operated at  $\sim 190^\circ$  K to suppress dark current and the loss of charge transfer efficiency due to radiation damage. The vertex detector and the cryostat make up the R20 module which is clamped to the ends of the CDC by means of support cones. The analog output is read locally and the data are then transmitted to analog-to-digital converters. CCD readout is fairly slow, with an integrated time of  $\sim 160$  ms (or  $\sim 19$  beam crossings). However, since the typical trigger rate is of the order of 1 Hz, most of the CCD readouts are emptied before the next event is recorded. VXD2 is only briefly described here, whereas more details will be given in the description of VXD3

### 3.2 The SLC Large Detector

---

and the comparison between the two.

#### VXD2

Installed in 1992, VXD2 is a 120 million pixel detector and it is built from 480 individual CCD wafers placed on 60 ladders, which are in turn arranged in four radial layers in order to provide position measurements from a radius of 3.0 cm to 4.2 cm from the beam axis. Since every layer only covers 50% of the azimuthal angle ( $\phi$ ), they have been oriented so that each of them covers the gaps in the one immediately innermost (see fig. 3.8); the polar angle coverage is  $|\cos\theta| < 0.75$ . The typical track produces on average 2.3 hits with a radial separation of as little as 4 mm. This resulted in a poor lever-arm, which limited the impact parameter resolution at the SLD IP. The mean  $r - \phi$  and  $r - z$  values for VXD2 are :

$$\begin{aligned}\sigma_{r\phi} &= 11 \oplus \frac{70}{p \sin^{3/2} \theta} \mu m \\ \sigma_{rz} &= 38 \oplus \frac{70}{p \sin^{3/2} \theta} \mu m\end{aligned}\tag{3.4}$$

for a track of momentum  $p$  and polar angle  $\theta$  with respect to the  $z$ -axis.

The thickness of each layer is  $1.15\%X_0$ , which also limits the precision, especially for low-momentum tracks for which scattering in the detector material is a dominant effect.

#### VXD3

Advances in CCD technology permitted an upgrade in the detector design with the following main advantages with respect to VXD2:

- extended polar angle coverage;

### 3.2 The SLC Large Detector

---

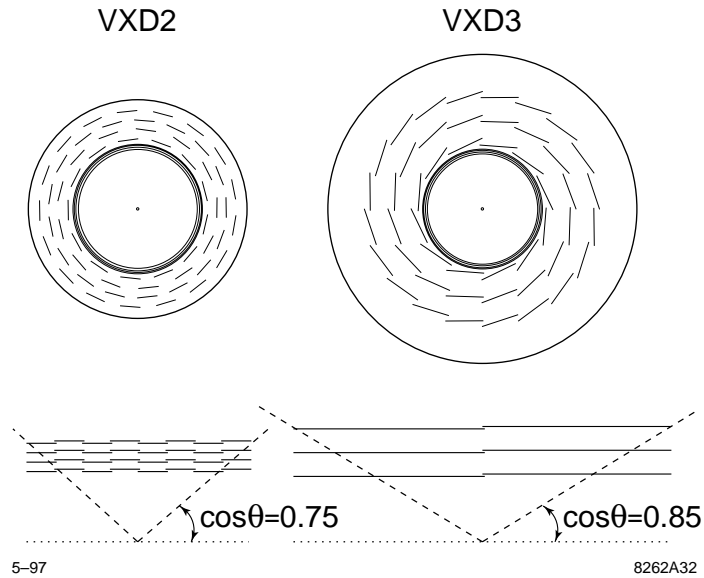


**Figure 3.8:** SLD vertex detectors

- full azimuthal coverage in each of the 3 layers, creating the possibility of VXD3 self-tracking, via the reconstruction of VXD-hit vectors for VXD tracks with  $\geq 3$  hits;
- larger radial lever-arm and reduced material in each layer for significantly improved impact parameter resolution.

VXD3 was built using customized CCDs (in contrast to VXD2), which were designed to accommodate specific detector requirements. In particular it was possible to manufacture larger wafers with no degradation in signal transport nor in readout time. The 307 Mpixel detector has three overlapping layers, placed at a radius of 2.8, 3.8, 4.8 cm respectively from the beam line. There are a total of 48 ladders, each of which carries 2 CCDs, one on top and one on the bottom: every CCD contains  $4000 \times 800$  pixels of size  $20 \times 20 \mu m^2$ .

### 3.2 The SLC Large Detector

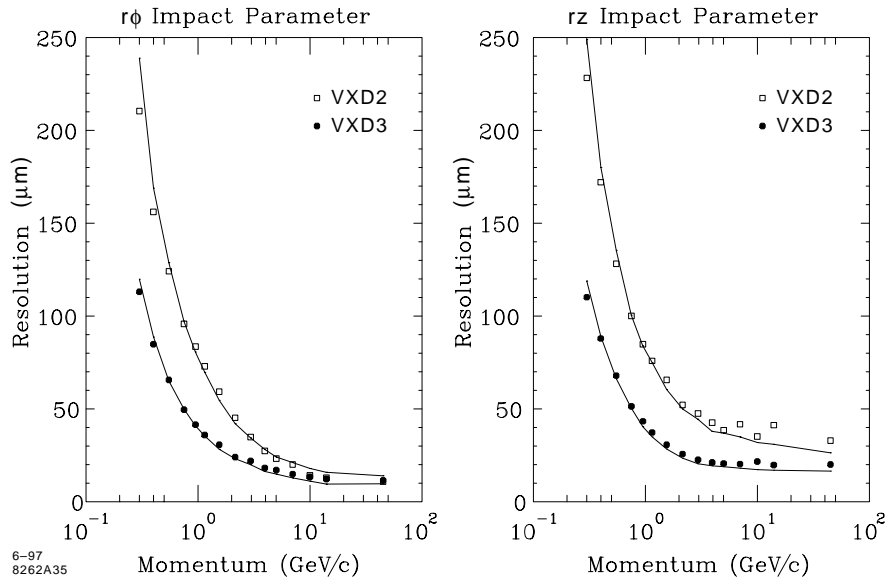


**Figure 3.9:** Track impact parameter resolutions as a function of momentum for VXD2 and VXD3 [51].

The layer thickness was reduced to 0.4% radiation lengths, with great improvement in the impact parameter resolution, as is shown in fig. 3.9. The measured VXD3 impact parameter resolution has been calculated to be [52]:

$$\begin{aligned}\sigma_{r\phi} &= 10.7 \oplus \frac{33}{p \sin^{3/2} \theta} \mu m \\ \sigma_{rz} &= 23.5 \oplus \frac{33}{p \sin^{3/2} \theta} \mu m\end{aligned}\tag{3.5}$$

In addition, the active layer length along the beam axis was increased by a factor of 1.7 to 16 cm, allowing an angular coverage out to  $|\cos \theta| = 0.85$  for 3 hits. Furthermore, the full azimuthal coverage in each of the three layers has opened the possibility of a vertex detector self-tracking independent of the CDC, thus improving the overall tracking efficiency.

### 3.2 The SLC Large Detector

---

Parameter	VXD2	VXD3
# of layers	4	3
# of ladders	60	48
# of CCDs	480	96
# of pixels ( $\times 10^6$ )	110	306
CCD active size (cm)	$1.3 \times 0.9$	$8.0 \times 1.6$
active z length (cm)	9.2	15.9
# hits per track	2.3	3.2
% of $\phi$ covered/layer	60	100
2 hit $\cos \theta_{max}$	0.74	0.90
3 hit $\cos \theta_{max}$	-	0.85
readout rate (MHz)	2	5
readout time (msec)	160	$\leq 100$
$X_0$ per layer	1.15%	0.36%

**Table 3.3:** Comparison between VXD2 and VXD3.

#### 3.2.2 The Drift Chamber

##### The mechanical design

The SLD Drift Chamber (CDC) [53] is designed to provide high resolution position and momentum measurements for charged tracks produced in an event. The CDC is a 2 m long cylindrical annulus, with its inner radius at 20 cm and the outer one at 100 cm, which operates in a uniform solenoidal magnetic field of 0.6 Tesla. The CDC wires, strung longitudinally between the two end-plates, are radially grouped into 10 *superlayers* of drift cells. The orientation of the wires alternate among axial layers (A) and stereo layers (U and V-type), resulting in an overall pattern AUVAUVAUVA (see fig. 3.10).

Wires in the axial layer are parallel to the beam axis, while those in stereo layers are tilted at an angle of +42 mrad and -42 mrad for U and V layers respectively. Every cell is about  $5 \times 5.9 \text{ cm}^2$ , and contains a set of 8 sense wires surrounded by 24 guard wires

### 3.2 The SLC Large Detector

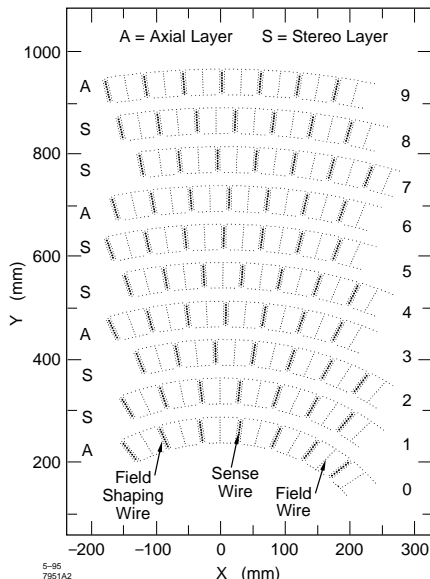


**Figure 3.10:** The CDC superlayers.

and 27 field shaping wires which define the cell boundaries.

The CDC is filled with drift gas in a mixture of 75%  $CO_2$ , 21% Argon, 4% Isobutane and 0.2%  $H_2O$ . A voltage of up to 7 kV is applied to the field wires in order to establish a precise electrostatic field, that causes the electrons liberated in the ionization process at the passage of a charged track to drift towards the sense wires at a uniform velocity of 8  $\mu\text{m}/\text{ns}$ . A further voltage difference of 3 kV between guard and sense wires provides gain amplification as the electrons avalanche down onto the sense wires (see fig. 3.11).

The transverse distance of a track from an individual sense wire is measured to an intrinsic resolution of 70  $\mu\text{m}$ , but the uncertainties in the wire locations and changes in the drift speed degrade the resolution to about 100  $\mu\text{m}$ . Both ends of the sense wires are instrumented with electronics, so that *charge division* can be used to measure the  $z$  coordinate of a hit. The resolution on the  $z$ -position, which is important for the measure-

### 3.2 The SLC Large Detector

---

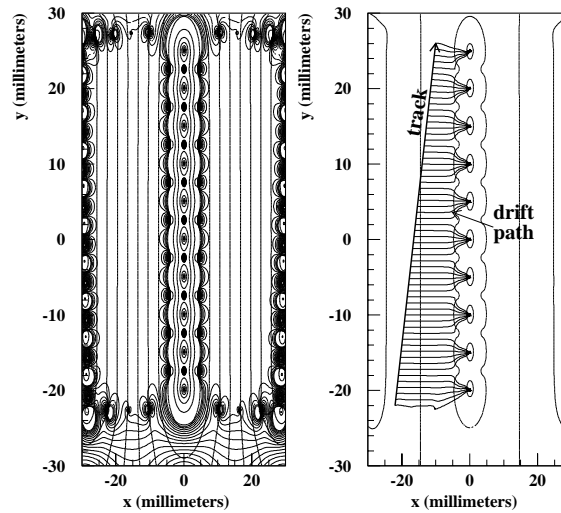


**Figure 3.11:** The field map for a CDC cell. The figure on the left shows the lines of constant potential (bold) and the lines of constant strength (thin) within a cell. The figure on the right shows a drift path of charges caused by a charged track passing through the cell.

ment of the track polar angle, was found to improve by increasing the stereo angle, but at the same time the resolution on the position of the projected hit in the  $x - y$  plane would become worse. A compromise between the two criteria limits the stereo angle to lie between 35 and 50 mrad.

#### Track reconstruction

The track-finding process begins at the superlayer level. Hits within a cell which lie on a straight line form a track-segment called *vector hit* (VH); there must be at least three hits in the cell to form a track segment. Pattern recognition then links these vector hits together to form candidate tracks. The linking algorithm operates in the  $x - y$  plane. In the first pass, only combinations with 10 VHs are considered, and the one with the

### 3.2 The SLC Large Detector

---

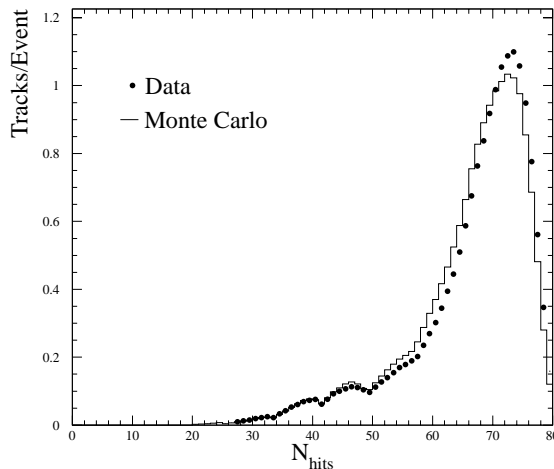


**Figure 3.12:** Distribution of number of hits on a track.

best  $\chi^2$  is taken as a candidate track. Its VHs are removed from the list and 9 VHs combinations are taken into account; the process is repeated until all tracks of at least 3 VHs are found. As a last step, a track-fitting procedure is applied. Starting with the estimated track parameters from the pattern recognition, the track fitter swims a helical trajectory through the detector, considering the effects due to multiple scattering, energy loss and local variations in the magnetic field. A  $\chi^2$  is formed comparing the proposed trajectory with the current parameters and their errors and its local minimum is sought iteratively using these parameters, their errors and their correlations.

Fig. 3.12 shows the distribution of the number of hits found per track in comparison to MC [55].

### 3.2 The SLC Large Detector

---

#### Momentum resolution

Both the intrinsic resolution and multiple scattering contribute to the total momentum resolution of the CDC. Muon tracks in  $Z^0 \rightarrow \mu^+ \mu^-$  decays are used to determine the first term because of their large identical momentum (45.6 GeV) and because they tend to leave hits in almost every layer (in the central region). A Gaussian fit to their  $q/p$  distribution (where  $q$  is the charge and  $p$  the momentum) provides the intrinsic resolution for the curvature measurement. Cosmic rays with varying momenta which pass through the central part of the CDC are used to measure the scattering term. The measured CDC track resolution is [54]:

$$\sigma_{1/p_{\perp}} = \frac{\sigma_{p_{\perp}}}{p_{\perp}^2} = \sqrt{\frac{0.0095^2}{p_{\perp}^2} + 0.0049^2} \quad (3.6)$$

The combined CDC+VXD resolution is [54]:

$$\sigma_{1/p_{\perp}} = \frac{\sigma_{p_{\perp}}}{p_{\perp}^2} = \sqrt{\frac{0.0095^2}{p_{\perp}^2} + 0.0026^2} \quad (3.7)$$

The geometry of the CDC provides uniform acceptance up to  $|\cos \theta| < 0.65$ , and some tracks can be reconstructed out to a production angle of  $|\cos \theta| < .87$ . For  $|\cos \theta| < 0.65$  the CDC can detect tracks with momentum above 4 GeV/c with a uniform 96% efficiency, degrading to 93% at 100 MeV [55].

#### 3.2.3 The Čerenkov Ring Imaging Detector (CRID)

Particle identification is extremely important for the capability of tagging heavy hadrons and their flavours. At SLD, this is achieved by using the CRID [56], which exploits the Čerenkov effect to provide separation among  $e$ ,  $\mu$ ,  $\pi$ ,  $k$  and  $p$  over a full range of

### 3.2 The SLC Large Detector

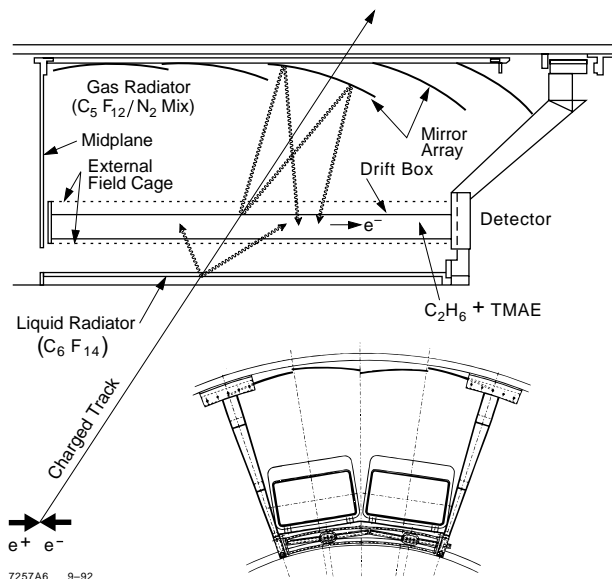


**Figure 3.13:** Geometry of a CRID module: radial view (lower image) and photoelectrons being detected on both sides of the TPC (upper image).

momentum (0.3-45 GeV).

The Čerenkov effect consists in the emission of electromagnetic radiation by charged particles passing through a medium with refractive index  $n$ , when their velocity  $\beta c$  exceeds the speed of light  $c/n$  in the medium. The wavefront of the Čerenkov radiation is shaped like a cone whose aperture  $\theta_C$  is given by  $\cos \theta_C = 1/(\beta n)$ , where  $n$  is the refractive index of the medium. The measurement of the Čerenkov angle combined with the momentum information provided by the CDC gives an estimate of the mass of the particle, and therefore its type.

The barrel CRID is a cylindrical annulus which contains 40 modules installed azimuthally around the CDC to provide complete coverage for the barrel region. Each module is divided into two independent longitudinal sections, each with a readout at its outer end (see fig. 3.13). Each CRID module consists of three parts: the radiator, the mirrors and the

### 3.2 The SLC Large Detector

---

drift box. The radiator is the medium where charged particles radiate Čerenkov light. This is then reflected and focused back by 400 mirrors onto 40 TPCs. These drift boxes contain  $C_2H_6$  gas and 1% of a photo-sensitive medium called TMAE, which provides good quantum efficiency for converting Čerenkov photons into photo-electrons (this however makes these chambers extremely sensitive to beam-related backgrounds, so that the CRID had to be turned off in particularly noisy conditions of running, with the consequence that CRID information is only available for 80% of the data). The photo-electrons are then drifted into a uniform electric field of 400 V/cm towards the multi-wire proportional chambers (MWPC) located at the end of the drift box furthest from the IP, where charges are read out. The coordinate location of a hit is obtained from the drift time ( $z$ ), the wire address ( $\phi$ ) and the charge division along the height of the box ( $r$ ). By plotting the Čerenkov angle as a function of the track momentum, one can distinguish several thresholds for each particle type, beyond which they are identified by the presence of a ring of the expected radius.

In order to obtain particle ID over a wide momentum range, there are two separate radiators in the CRID: a liquid one, composed of  $C_6F_{14}$ , with an index of refraction  $n = 1.2780$ , which provides good separation in the momentum range from 0.5 to 3 GeV/c; and a gaseous one, composed of  $C_5F_{12}$ , with an index of refraction  $n = 1.0026$ , which covers the high momentum range up to 35 GeV/c. A typical track leaves approximately 8-10 hits in the gas and 13-16 in the liquid [57]. The Čerenkov angle resolution for a track is better than 1 mrad: uncertainties are due to variations in the refractive index, multiple scattering, aberrations of the image of the ring and momentum smearing due to changes in the par-

### 3.2 The SLC Large Detector

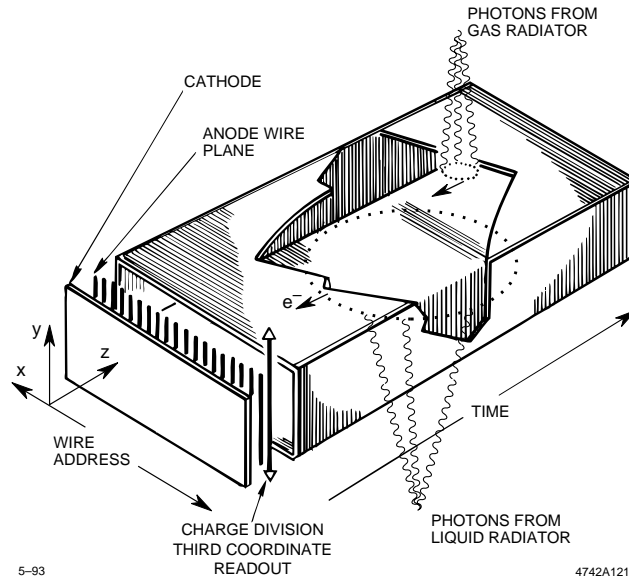


**Figure 3.14:** Schematic view of a TPC and MWPC detector for a CRID module.

ticle flight direction. Fig. 3.15 shows the CRID efficiency matrix. Information from the CRID, stored in likelihood functions for different particle probabilities, will be crucial for this analysis in the muon selection algorithm.

#### 3.2.4 Calorimetry

The main objective of calorimetry is the measurement of the energy of a particle; this is particularly crucial for neutral particles, which escape the detection of the tracking system, whereas it only adds relatively further information for charged particles. However, due to different showering characteristics (such as electromagnetic *vs* hadronic shower deposition, transverse spread or longitudinal depth), the energy deposition in the calorimeter can be used to provide particle identification for electrons or muons. Moreover, spatial and angular information provided by the calorimeter, combined with momentum

### 3.2 The SLC Large Detector

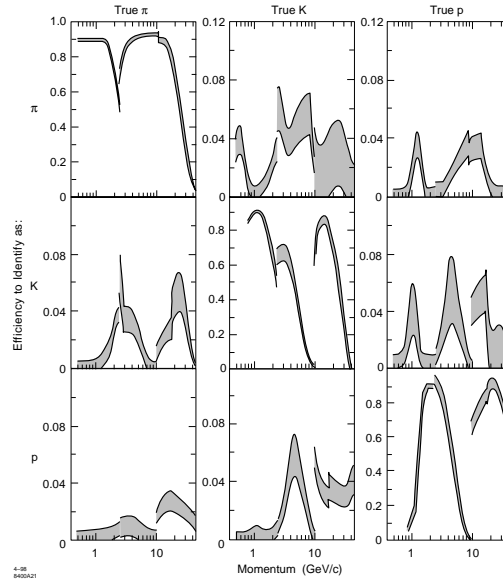


**Figure 3.15:** The CRID efficiency matrix. The diagonal plots show the efficiency for correctly tagging a particle. The two peaks represent the efficiencies for the liquid (left) and gas (right) radiators. The off-diagonal are the mis-ID efficiencies. The bands represent the error bars with the center of the band representing the central value for the efficiency [58].

information, is very useful in determining several event variables such as the thrust axis, the event shape and the jet axes. Another important function of the calorimeter is to provide the measurement of the total observed event energy, whereby one can extract the missing energy of neutrinos: therefore, the calorimeter should be as hermetic as possible to minimize leakage of particles.

SLD employs a hybrid structure, composed of a Liquid Argon Calorimeter (LAC) [59] and a Warm Iron Calorimeter (WIC) [61], which provides the magnetic flux return and muon identification.

### 3.2 The SLC Large Detector

---

#### The Liquid Argon Calorimeter

The barrel LAC is a 6 m long cylindrical annulus just outside the CRID, with an inner radius of 1.8 m and an outer radius of 2.9 m, which covers an angular region up to  $|\cos\theta| < 0.84$ . It is composed of long modules (see fig. 3.16), which are stacked around the CRID in the azimuthal plane ( $\phi$ ). The modules are made of planes of lead radiator immersed in a liquid argon bath and they are radially divided into four sections: two inner electromagnetic (EM) sections and two outer hadronic (HAD) sections. These are further segmented into readout towers that project back to the IP both azimuthally ( $\phi$ ) and along the beam axis ( $z$ ). In  $\phi$  the towers have a fixed angular width of 33 mrad and 66 mrad for the EM and HAD sections respectively (each module spans 4 EM towers and 2 HAD towers in width, matching the edges). In  $z$  the towers have a fixed angular size of 36 mrad for the EM section and 72 mrad for the HAD section.

The LAC is a conventional sampling calorimeter: particles entering the LAC interact with the lead and produce a secondary shower of low energy particles which ionize the argon. The lead plates are held alternatively at ground or high voltage, producing a field to collect the liberated charge in the argon. Since the argon supplies no charge amplification, the charge observed is proportional to the energy deposited. The energy deposited in the calorimeter is converted into an electronic signal, which is read out and converted back into units of energy.

The EM section provides a total of 21 radiation lengths of material, which will absorb  $\sim 98\%$  of the energy from a 50 GeV electron. The EM and HAD sections together provide a total of 2.8 absorption lengths of material, which will contain 90% of the energy from a

### 3.2 The SLC Large Detector

---

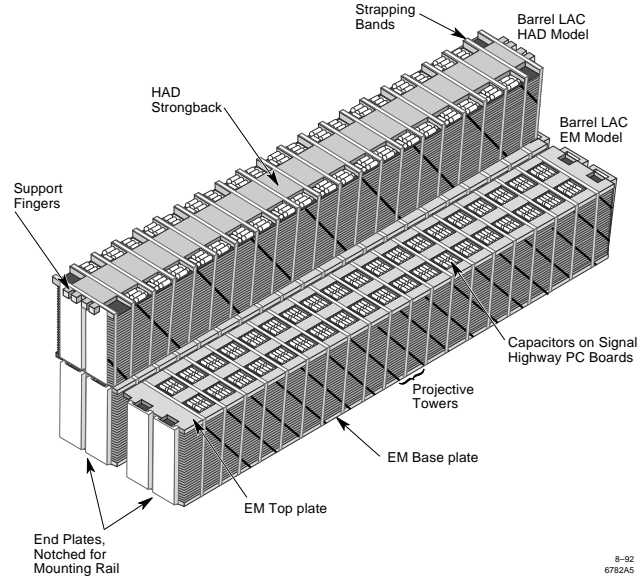


**Figure 3.16:** View of a LAC module, showing the inner EM and the outer HAD sections.

hadronic shower. The segmentation of the LAC modules allows for spatial determination of the energy shower. The energy resolution of the LAC has been shown to be  $\sim 15\%/\sqrt{E}$  GeV for EM showers and  $\sim 60\%/\sqrt{E}$  GeV for hadronic showers [60].

Two endcap calorimeters cover the region  $0.82 < |\cos \theta| < 0.99$  and are made of 16 modules containing both an EM and a HAD sections. Endcap modules differ from barrel modules in geometry but they are functionally identical. The EM resolution in the endcaps is  $\sim 25\%/\sqrt{E}$  GeV [60], comparatively worse than in the barrel, due to the presence of more material related to the cryogenic system. A gap is also present in the coverage of the hadronic section, as is visible in fig. 3.7.

### 3.2 The SLC Large Detector

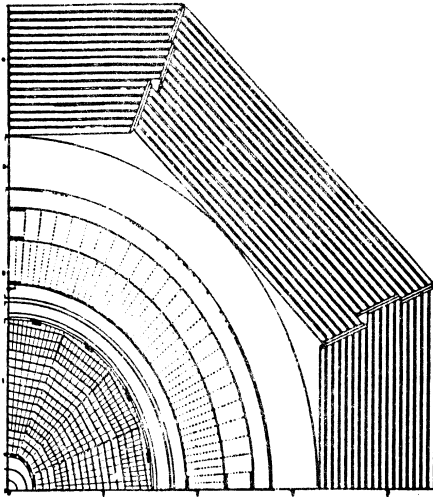


**Figure 3.17:** Quadrant section of the WIC barrel.

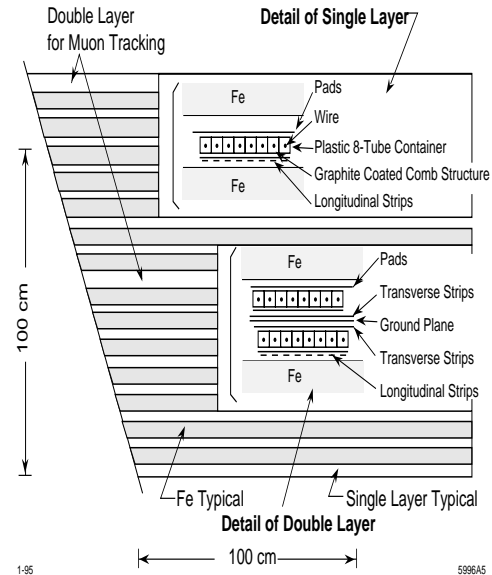


**Figure 3.18:** Cut-away view of the WIC.

#### The Warm Iron Calorimeter

The Warm Iron Calorimeter (WIC) is the outermost system of SLD: located just outside the magnetic coil, the WIC provides a flux return for the solenoid, it measures the remaining 10% of the energy deposited which is not detected by the LAC and provides muon identification. The WIC is also divided into a barrel and two endcap regions. The barrel is 6.8 m long and runs from 3.3 m to 4.5 m in radius. It contains 8 azimuthal sections (*octants*), each of which is further divided in two semi-octants (*coffins*), slightly displaced horizontally with respect to each other to minimize gaps. Every coffin is made of seven 5 cm thick iron layers which are separated by 3.2 cm thick gaps instrumented with a system of Iarocci tubes operated in limited streamer mode (see fig. 3.17 and fig. 3.18).

A limited streamer tube (LST) is essentially composed of a cylindrical structure (cathode) with diameter on a mm scale and filled with gas, at the center of which runs a wire (an-

### 3.2 The SLC Large Detector

---

ode), which is kept at high voltage and has dimensions of the order of microns. Electrons produced by ionization in the gas drift towards the anode under the effect of the electric field; when they are in proximity of the wire, where the field is more intense, secondary ionization occurs along with avalanche multiplication (primary and secondary avalanches form the streamer). Moving away from the anode the field decreases gradually until there are no more the conditions for a secondary ionization. The electric field is furthermore distorted by the distribution of the positive ions within the tube: the limited streamer mode would result from a delicate balance between the two effects.

At SLD there are about 40000 LSTs which are grouped by eight in modules: their active section is  $9 \times 9 \text{ mm}^2$  with a  $100 \mu\text{m } B_e C_u$  wire running at the centre of it, and the voltages applied are around 4.75 kV. The tubes are filled with gas, which is a mixture of 2.5% argon, 9.5% isobutane and 88% carbon dioxide. Different criteria led to the choice of this particular composition: mainly the need to maximize gain and efficiency while keeping voltages as low as possible, together with a requirement of non-inflammability of the mixture and of stability of the response. External readout is organized through two systems of electrodes, which pick up the charge by induction and are connected to the data acquisition system: copper strips, both parallel and orthogonal to the anode direction, have the function of reconstructing the trajectories of the ionizing particles (in  $r - \phi$  and  $z$  respectively), whereas quadrangular pads measure the total charge released by the streamer and therefore the energy. The central layer (8 and 9) and the outside layer (16 and 17) of the barrel are double layers, instrumented with two planes of streamer tubes, one with both longitudinal and perpendicular strips, and the other with perpendicular strips and pads;

### 3.2 The SLC Large Detector

---

this is to measure two space points (midpoint and outermost point).

The endcaps are divided into an internal and an external part, octagonal shaped and containing seven layers of iron each. The inner endcap is made up of three horizontal parts, with the tubes running horizontally; the outer endcap is made up of two vertical parts with the tubes running vertically. On its external sides the outer endcap has double layers, one with double width longitudinal and transverse strips and the other with pads and transverse strips.

Barrel and endcaps, however, fail to provide a complete angular coverage for muon identification. In order to meet some earthquake safety standards, the WIC dimensions had to be sacrificed with respect to the original design report. The consequence of this is a gap between barrel and endcaps that the introduction of 45 degree chambers attempted to cover. These are 30 pieces of detector placed around the WIC that were meant to work as “patches” for the existing gaps, bringing up to about 60% the efficiency in the region between barrel and endcaps, that otherwise would only have been around 25%. In fact, due to the complexity of their geometry, the relative software and simulation have never been available, and therefore their information is not included in this analysis.

The spatial resolution of a strip is the standard deviation of the residuals distribution obtained from a fit that does not include the hits of the strip in question. The intrinsic resolution is given by:

$$\sigma = L/\sqrt{12} \tag{3.8}$$

where L is the width of the strips. For longitudinal strips in the barrel  $\sigma \sim 0.29$  cm; the measured resolution is of course worse than that, approximately 0.4 cm.

## 3.2 The SLC Large Detector

---

Calibration was done with cosmic rays and  $Z^0$  decays in  $\mu^+\mu^-$ : considering tube inefficiencies and imperfect angular coverage the total average efficiency per plane is roughly 80 – 85% [62] [54].

### 3.2.5 The Luminosity Monitor

The SLD luminosity monitor (LUM) [63] is used to measure the  $Z^0$  production rate on an online (real time) basis through the detection of  $e^+e^-$  pairs that have undergone Bhabha scattering at the SLC IP. Since the cross-section for Bhabha scattering is precisely calculable in QED, and since it occurs much more often than  $Z^0$  production, its rate provides the most precise measurement of delivered luminosity at the IP by the linear collider. The luminosity calorimetry was designed to:

- provide a high precision measurement of the absolute luminosity;
- extend the electromagnetic calorimetry coverage down to small angles;
- tag electrons.

The LUM, shown in fig. 3.19, consists of two silicon-tungsten calorimeters which are arranged in projective towers with a high degree of segmentation and located 1 m downstream from the IP along the beam axis. Each calorimeter contains two separate modules: the Luminosity Monitor Small Angle Tagger (LMSAT), to cover the region between 28 and 68 mrad, and the Medium Angle Silicon Calorimeter (MASiC), for the region between 60 and 200 mrad <sup>2</sup>. Electromagnetic showers that develop in the tungsten layers create

---

<sup>2</sup>This calorimeter was intended to extend the coverage of the LAC, but was in fact never used.

### 3.2 The SLC Large Detector

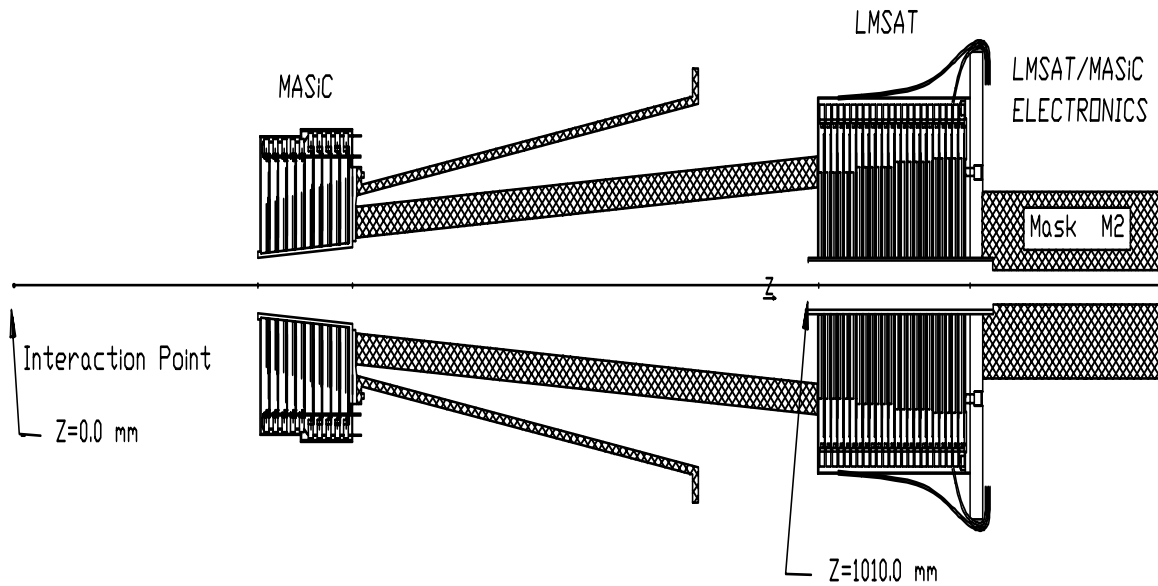


**Figure 3.19:** A side view of the SLD LUM, showing the LMSAT and the MASiC.

electron-hole pairs in the fully depleted silicon detectors; the showers are then collected by charge sensitive preamplifiers. The measured energy resolution is 6% at 50 GeV [64]. Table 3.4 lists the luminosity results for the separate SLD runs and the combined results for the two periods which use different vertex detectors.

	Integrated luminosity ( $pb^{-1}$ )		
1993	1.777	$\pm 0.005(stat)$	$\pm 0.018(syst)$
1994-95	3.699	$\pm 0.007(stat)$	$\pm 0.037(syst)$
<i>VXD2</i>	5.476	$\pm 0.004(stat)$	$\pm 0.055(syst)$
1996	1.860	$\pm 0.005(stat)$	$\pm 0.019(syst)$
1997	3.790	$\pm 0.007(stat)$	$\pm 0.037(syst)$
1998	8.321	$\pm 0.011(stat)$	$\pm 0.083(syst)$
<i>VXD3</i>	13.971	$\pm 0.006(stat)$	$\pm 0.140(syst)$

**Table 3.4:** SLC luminosity results for the various run periods [55].

## 3.2 The SLC Large Detector

---

### 3.2.6 Data Acquisition

Details of the data acquisition [65] vary somewhat for each SLD subsystem, but in general the analog signals are digitized by front end electronics modules mounted directly on the detector. These data are then shipped serially over optical fiber links to the FASTBUS based processing modules. These modules apply various calibrations to the raw data, and perform a variety of basic analysis tasks including waveform hit finding, rudimentary particle tracking and the calculation of other quantities to provide information for the trigger decision. This is made for every SLC beam crossing, and for all triggered interactions the data are collected from the different subsystems, packaged into an event, and written to a shared event pool on the SLDACQ Vax. At this stage, the various on-line processes can access this information to provide monitoring information and graphical one-event displays, and from this pool the events are eventually written to tape.

Trigger criteria are briefly summarized here:

- energy trigger: requires at least 8 GeV of total deposited energy in the LAC. Only towers above the threshold of 60 (12) ADC counts in the EM (HAD) section contribute, corresponding to 246 MeV (1.298 GeV);
- tracking trigger: requires at least 2 charged tracks, separated by an opening angle  $\delta\phi > 20^\circ$ , passing through  $\geq 9$  superlayers of the CDC. In addition, the CDC cell hits must match a configuration in a pattern map calculated for all charged tracks with  $p_\perp > 250$  MeV/c;
- HAD trigger: is a combination of the previous two;

### 3.2 The SLC Large Detector

---

- Muon trigger: requires one charged track with 9 CDC superlayer hits and calorimetric hits in the opposite WIC octant;
- WAB trigger: records wide angle Bhabha events by requiring two charged back-to-back tracks in the CDC;
- Bhabha trigger: requires at least 12.5 GeV of energy deposit in both the North and South EM2 sections of the LUM;
- random trigger: occurs every 20 seconds, writing down data for background studies, independent of the status of the other triggers.

A typical SLD event is roughly 250-300 kbytes.

# Chapter 4

## The SLD Monte Carlo

### 4.1 Introduction

Many analyses at SLD rely on Monte Carlo models of both the detector and underlying physical aspects involved in the process under study. On one hand, these models are necessary for determining measurement biases induced by real detectors with finite acceptances, efficiencies and resolutions; on the other hand, analyses are often sensitive to physical properties which are not directly an object of study (for example, the  $A_b$  measurement with leptons with respect to the  $B$  and  $D$  hadrons momentum spectra). These properties need to be modelled according to the results of other experiments, using the uncertainties affecting them to calculate systematic errors in the final result.

The SLD Monte Carlo consists of an event generator, which models the underlying physics of  $Z^0$  decay, and a detector simulation model. The SLD event generator is JETSET 7.4 [66], incorporating Lund string fragmentation. Half of the events are generated with an electron

## 4.1 Introduction

---

beam polarization of +100% and half with -100%, with the positron beam unpolarized. In order to simulate the left-right asymmetry, a fraction of the right-handed events must be eliminated, given by:

$$f_{\text{toss}} = \frac{2|P_e|A_e}{1 + |P_e|A_e} \quad (4.1)$$

where  $|P_e| = 1.0$ .

JETSET implicitly includes initial and final state photon radiation and uses a parton shower model for final state gluon radiation. The fragmentation function, describing the energy of a hadron as a function of the beam energy, is parametrized in light-flavoured events by the Lund symmetric function [67]:

$$f(z) \propto z^{-1}(1-z)^a e^{-bm_{\perp}^2/z}, \quad (4.2)$$

where  $z = 2E/\sqrt{s}$ ,  $m_{\perp}$  is the “transverse mass” ( $m_{\perp}^2 = E^2 - p_{\parallel}^2$ ) and  $a, b$  are parameters that can be tuned to reproduce the momentum distribution of final state particles in the data (examples of tuned values are 0.18 and 0.34  $\text{GeV}^{-2}$  [68]).

Because of their large mass, the fragmentation behaviour in heavy quarks is very different from that of light quarks. The function used in this case is the Peterson function [69]:

$$f(z) \propto \frac{1}{z(1 - (1/z) - \epsilon_q/(1-z))^2}, \quad (4.3)$$

where the parameter  $\epsilon_q$  is fixed at 0.060 for  $c$  quarks [71] and 0.006 for  $b$  quarks [70]. The stiffness of the  $b$  fragmentation function is one of the features that allows a momentum-weighted charge measurement of  $A_b$  to be effective, because weighing the track charges with their momenta de-emphasizes the role of fragmentation tracks (tracks originating from the hadronization process).

## 4.1 Introduction

---

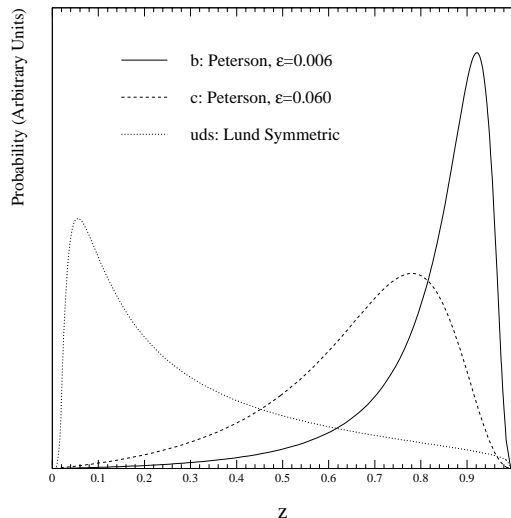


**Figure 4.1:** Fragmentation functions for uds, c, and b quarks. A value of  $m_{\perp} = 300 \text{ MeV}/c^2$  has been assumed for the Lund symmetric function.

### 4.1.1 The Event Generator

JETSET is used in the SLD generator to decay all heavy unstable particles except the  $B^0$ ,  $B^-$  and the  $B_s$  and their antiparticles. This strategy was chosen because the decay particle spectra of JETSET for those mesons disagree with available data from CLEO and ARGUS. Rather than retune JETSET, the CLEO decay simulation package was implemented. This package consists of a full table of decay channels for every particle in question, according to the world averages for the decay branching ratios. For every decay the model randomly chooses a channel with probability proportional to these branching ratios. For semileptonic decays  $B \rightarrow l\nu X$  momenta are chosen according to the ISGW model, developed by the CLEO collaboration [72] and modified for the SLD environment with the incorporation of a fraction of  $B \rightarrow D^{**}l\nu$  decays. SLD's branching fractions for the semileptonic decay modes are shown in table 4.1. The momentum spectrum distribution

## 4.1 Introduction

---

Decay mode	Branching fraction ( $e, \mu$ )	Branching fraction ( $\tau$ )
$B \rightarrow Dl\nu$	2.554%	0.4%
$B \rightarrow D^*l\nu$	5.874%	1.1%
$B \rightarrow D^{**}l\nu$	2.532%	1.0%
Total	10.96%	2.5%

**Table 4.1:** SLD semileptonic B meson decay branching modes.

of leptons from  $B$  semileptonic decays as measured by CLEO is reproduced in fig. 4.2 together with the SLD Monte Carlo results.

These distributions are of particular interest for this analysis, if interpreted in terms of transverse momentum distributions. In fact leptons from  $B$  cascade decays tend to have charge of opposite sign with respect to leptons from  $B$  direct decay. Since the charge is used to determine the sign of the asymmetry, it is very important to accurately simulate the momentum spectrum of the two categories of decay.

The hadronic decays of the  $B$  mesons are considerably less well constrained, but fortunately a large fraction (45%) of hadronic  $B$  decays can be tabulated in known exclusive modes. The charmonium states in particular leave distinctive leptonic signals, and knowledge of the branching fractions of charmonium into leptons allows inference of the charmonium content of  $B$  meson decay. This is particularly important since charmonium states contribute to wash out the observed asymmetry. But a large portion of hadronic decays must be modeled in a more inclusive manner, and the parameters of the model tuned to bring the inclusive spectra in agreement with available data. Comparisons of the CLEO/SLD decay model with data from CLEO and ARGUS are shown in table 4.2 and fig. 4.3.

Most distributions agree fairly closely, except the very high momentum tail of the

## 4.1 Introduction

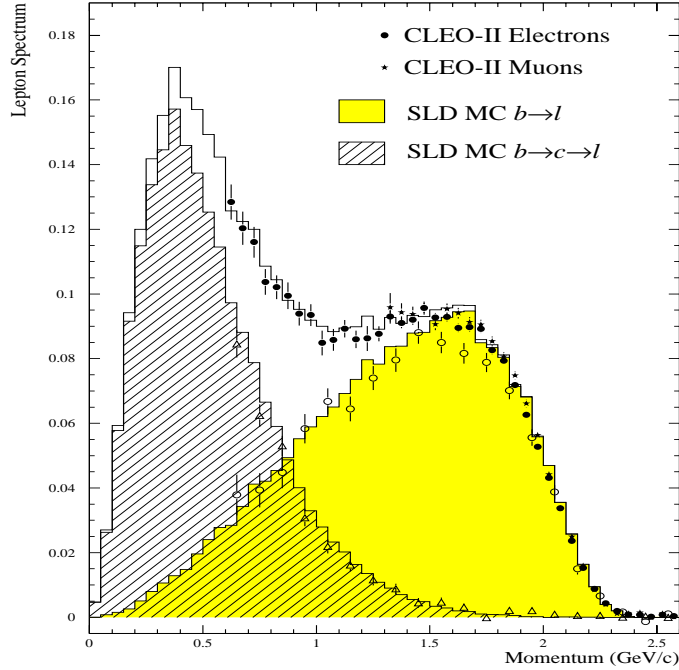


**Figure 4.2:** Lepton momentum distribution in  $B^0$ ,  $B^\pm$  meson decays according to CLEO results in comparison with the decay model adopted at SLD. The Monte Carlo contributions from prompt  $B \rightarrow l$  and  $B \rightarrow D \rightarrow l$  are shown shaded and hatched respectively. CLEO results are represented by open circles for leptons from direct decays, by triangles for leptons from cascade decays, by solid circles (electrons) and stars (muons) for the total spectrum [73].

Branching fraction	CLEO $\Upsilon(4S)$ DATA	CLEO/SLD model
$\text{BR}(B \rightarrow D^0 X)$	$(62.1 \pm 2.6)\%$	64.8%
$\text{BR}(B \rightarrow D^+ X)$	$(23.9 \pm 3.7)\%$	26.6%
$\text{BR}(B \rightarrow D_s^+ X)$	$(10.0 \pm 2.5)\%$	10.7%

**Table 4.2:** Comparison of branching fractions of  $B$  mesons at the  $\Upsilon(4S)$  to the different  $D$  mesons. Data are the CLEO/ARGUS average in August 1994.

## 4.1 Introduction

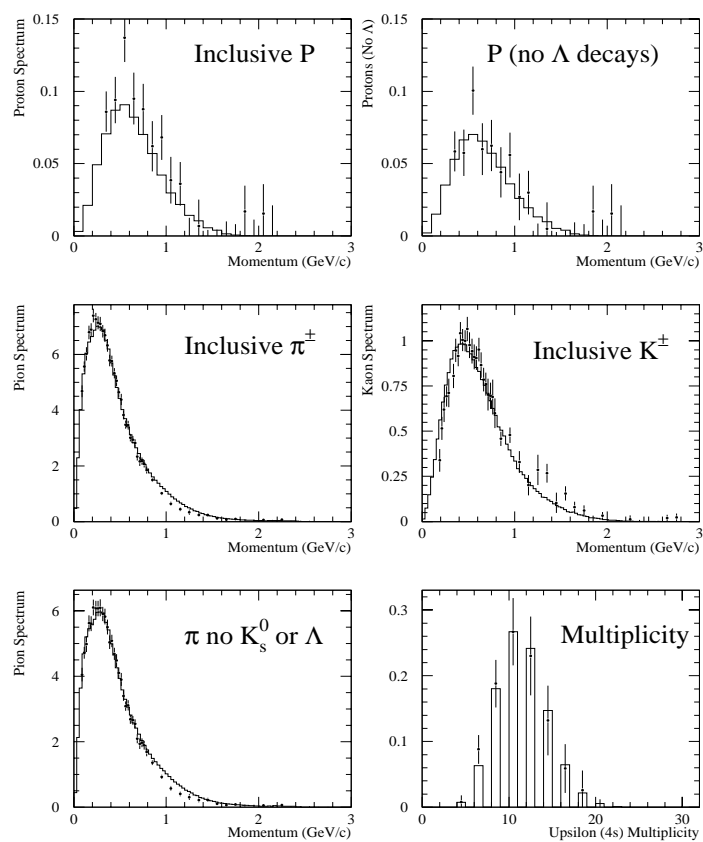


**Figure 4.3:** A comparison of the SLD-tuned CLEO  $B$  meson decay model (histogram) with inclusive particle spectra from ARGUS (points).

## 4.1 Introduction

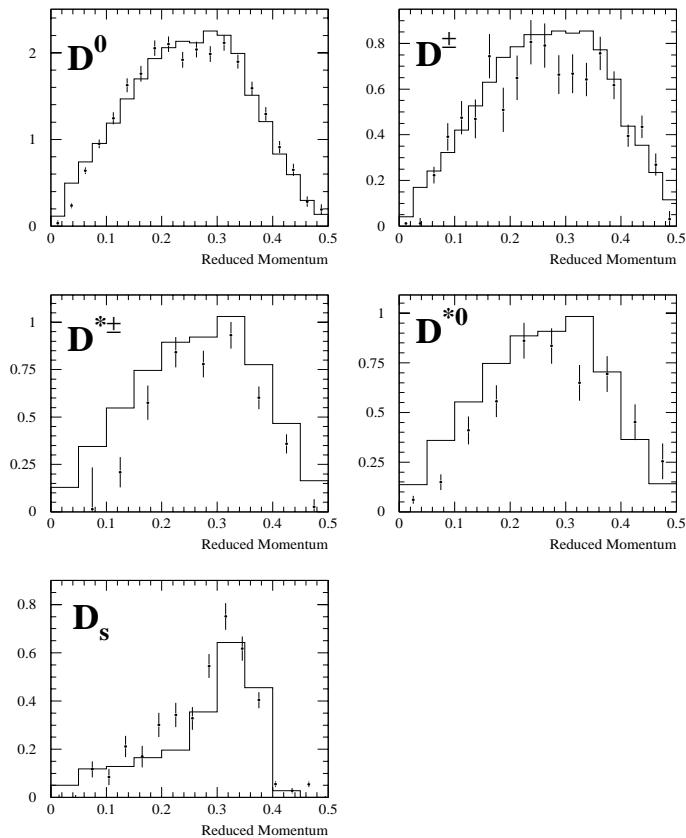


**Figure 4.4:** Comparison of the spectra of  $D$  mesons from  $B$  decay in the SLD Monte Carlo (histogram) against data measured by CLEO [75] (points).

inclusive pion spectrum. The total inclusive multiplicity observed by ARGUS is  $10.81 \pm 0.05$  (*stat*)  $\pm 0.23$  (*syst*) [74] as compared with 11.04 in the SLD tuned Monte Carlo. The comparison of the  $D$  momentum spectrum from  $B$  decays, in fig. 4.4 and 4.5, shows the advantages of using the CLEO model. There is good agreement between this and the available data, whereas JETSET shows a  $D$  spectrum that is too hard.

4.1 Introduction

---

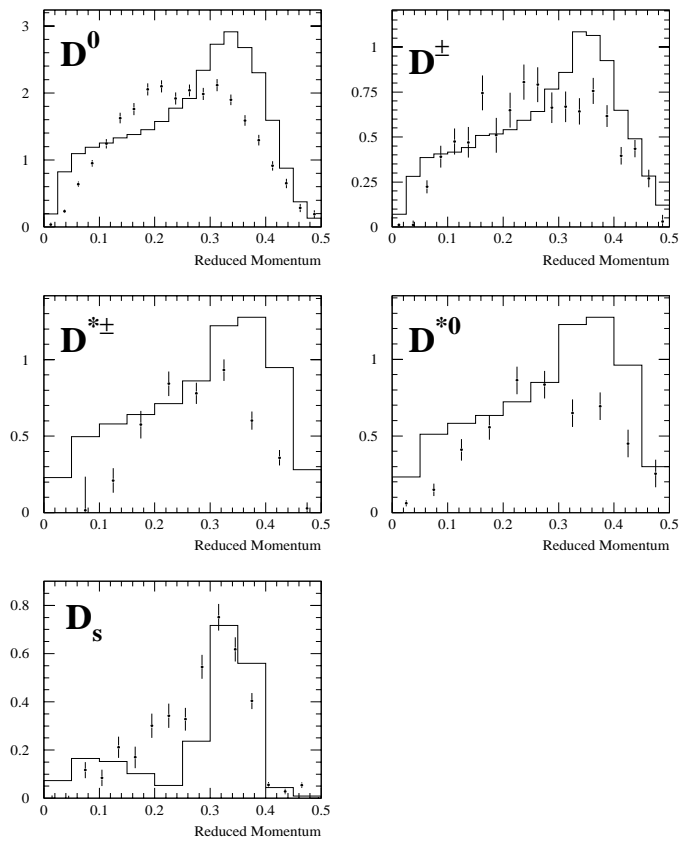


**Figure 4.5:** Comparison of the spectra of  $D$  mesons from  $B$  decay in the default JETSET 7.4 model (histogram) against data measured by CLEO [75] (points).

## 4.1 Introduction

---

### 4.1.2 Detector Simulation

The Monte Carlo needs to simulate the efficiency, acceptance and resolution effects for observables of interest, as well as the efficiency of the particle reconstruction algorithms applied to the data.

Resolution and efficiency of the detector subsystems depend on the amount and location of material that particles pass through. Multiple scattering degrades position and momentum resolution and electromagnetic or hadronic showers initiated in the detector before or within the tracking volume introduce extraneous particles. These interactions must be simulated to evaluate detector performance and to adjust the analyses for possible biases. As with other high-energy physics experiments, SLD uses version 3.21 of a particle-detector simulation package developed at CERN called GEANT [76]. GEANT starts with a list of particles from the  $Z^0$  decay generator, a detailed description of the detector material and a magnetic field map. It then traces the particle trajectories until they reach boundaries of detector material, at which point it calculates the interaction probability per unit of path length and randomly chooses or not to simulate an interaction of the particle with the detector. GEANT includes the software routines EGS4 [77] for simulating electromagnetic interactions and GEISHA [78] for simulating hadronic interactions. The next step is to simulate the detector response to all of the particles. The VXD digitization simulates the charge deposited in the silicon, as well as the efficiencies of the CCDs for recovering this charge and random misalignments. Digitization of the CDC involves interpolating each charged particle's track to the charge collection plane for each wire that is to receive a signal. The purpose is to find the closest distance from the track to the wire to calculate the

## 4.1 Introduction

---

time of the leading edge of the CDC pulse. The total ionization is calculated as a function of the particle type, momentum and path length. For the LAC, GEANT parametrized showers simulate energy deposition in the towers. Also simulated are dead towers and towers with low energy response.

Accelerator-related backgrounds are difficult to model, since they are highly variable and have characteristics very different from particles from  $Z^0$  decays (muons generated far upstream, low-energy electrons looping in the magnetic field...). These backgrounds can introduce hit-finding inefficiencies in the tracking chambers (through saturation of the CDC amplifiers by sprays of background particles) and add background energy to the calorimeter. The best way to simulate them is to measure them from the data. For each  $Z^0$  identified in the data sample, a random trigger taken at a nearby time is culled from the raw tapes. The signals from the random trigger are then merged with the digitized signals from the Monte Carlo simulation. Random triggered events that are simultaneous with physical events are not considered.

# Chapter 5

## Event Selection and B Tagging

This analysis is based on roughly 350,000 selected hadronic events produced in  $e^+e^-$  annihilations at the  $Z^0$  pole at the SLAC Linear Collider during the 1993-1998 runs.

The full SLD data sample can be divided into the following categories:

- $Z^0 \rightarrow q\bar{q}$  (hadronic) events: used for this measurement, they are characterized by a high track multiplicity and by an energy deposit which is approximately equal to the  $Z^0$  mass;
- $Z^0 \rightarrow \mu^+\mu^-$  (dimuon) events: they consist of two back-to-back high momentum charged tracks, with very small energy deposit in the calorimeter;
- $Z^0 \rightarrow \tau^+\tau^-$  events: they typically present 2 to 6 charged tracks, with a total energy deposit smaller than the  $Z^0$  mass because of the emission of high energy neutrinos;
- $Z^0 \rightarrow e^+e^-$  (or Bhabha) events: like dimuon events they too consist of two high

## Event Selection and B Tagging

---

momentum charged tracks, but unlike them, they do not pass the muon filter and leave a characteristic signature of two compact high energy clusters deposited in the LAC;

- two-photon events: they are generated in the process  $e^+e^- \rightarrow e^+e^- + \gamma\gamma$ ,  $\gamma\gamma \rightarrow f\bar{f}$ . The  $e^+e^-$  in the final state generally travel unobserved down the beampipe, while the detected  $f\bar{f}$  are characterized by a low energy deposition. They occur rather frequently, but only few are energetic enough to trigger the detector. Their cross section has been calculated to be  $\sim 5$  nb at the  $Z^0$  [79], and their contamination of the hadronic sample is of the order of  $\leq 0.02\%$  [80].
- $e^+e^- \rightarrow \gamma\gamma$  events (QED  $t$ -channel photon-photon final-state production): their signature is again two back-to-back 45 GeV electromagnetic hits, just as for wide-angle Bhabhas. They sum up to approximately 0.2% of the total  $Z^0$ -peak cross section.
- Photon mediated and interference events: at the  $Z^0$  pole, the photon-mediated  $s$ -channel cross section is finite but dominated by the  $Z^0$  resonance. In addition,  $\gamma - Z^0$  interference has a small contribution off-pole. Including only hadronic and tau decays, the contribution of the  $\gamma$  and  $\gamma - Z^0$  events is 0.12% of the cross section at the  $Z^0$  peak [81]. A correction to the polarized forward-backward asymmetry to account for the contribution of these events will be included in the final results.
- *beam wall* background: slightly off-energy particles in the SLC accelerator which strike the surface of the SLD's beam pipe and produce several low-energy tracks.

## Event Selection and B Tagging

---

These events are exceedingly rare and they are distinguished by low total energy and a displaced vertex in the  $z$  direction. They are therefore easy to identify, even if the simultaneous occurrence of such events from each beam could resemble a valid  $Z^0$  decay.

- SLC muon background: the SLC produces muons when stray electrons and positrons collide with the beampipe. Some of these muons are transported by the accelerator and strike the SLD in a nearly horizontal direction. If enough of these muons strike at once, they deposit enough energy to trigger the detector and become part of the data sample.
- *beam splash* background: occasionally SLC has a momentary equipment failure that produces one or a series of bad electron or positron bunches. By the time this bunch reaches SLD, it has collided with many parts of the accelerator and produced a splash of energy. These events are characterized by enormous deposits of energy in the calorimetry and a large number of uncorrelated hits in the charged tracking system.
- cosmic rays: they can in principle deposit substantial energy in the LAC. The dominant process leaving significant energy (20 GeV) is radiation by a muon of a hard photon.

## 5.1 Hadronic event selection

---

### 5.1 Hadronic event selection

Trigger thresholds at SLD have been kept as low as possible in order to maximize the efficiency for collecting  $Z^0$  events. Recorded events are then subjected to offline filters. The *EIT pass-1* filter is used to eliminate a large fraction of such background events. This filter selects events using calorimetry information only, which is processed much faster than tracking information. EIT pass-1 [82] is based on three LAC quantities:

- NEMHI, the number of LAC EM towers with signals above the high threshold of 60 ADC counts. This is equivalent to  $\sim 250$  MeV from minimum-ionizing particles (min-I);
- EHI, the sum of the energy deposited in all EM (HAD) towers with signals greater than the high thresholds of 60 (12) ADC counts. This is equivalent to 250 MeV (1.3 GeV) min-I;
- ELO, the sum of the energy deposited in all EM (HAD) towers with signals greater than the low thresholds of 8 (12) ADC counts. This is equivalent to 33 MeV (130 MeV) min-I.

The filter requires that each event satisfy:

1.  $NEMHI \geq 10$ ;
2.  $EHI > 15$  GeV min-I;
3.  $ELO < 140$  GeV min-I;
4.  $NEMHI > 0$  for both North and South hemispheres;

## 5.1 Hadronic event selection

---

$$5. \quad 3 \times (ELO - 70) < 2 \times EHI$$

The first two cuts select events which deposit high energy in the calorimeter, the others are meant to remove the different types of background.

Events surviving the EIT Pass-1 filter are classified by the EIT Pass-2 filter into hadronic,  $\mu$ -pair or WAB event candidates.

A further selection based on tracking information is then applied, to reject all the residual non-hadronic contamination in the sample and to insure that most basic distributions in the data are reproduced by Monte Carlo events. The SLD IP and the resolution of track impact parameters need to be determined before applying the cuts. The centroid of the SLD IP is reconstructed from tracks in thirty sequential hadronic decays to a precision of  $\sigma_{r\phi} \simeq 4 \pm 2 \mu\text{m}$  (1997-8) [83]. The IP position along the beam axis is determined event by event using charged tracks with a resolution of  $\sigma_z \simeq 30 \mu\text{m}$  (1997-8) [83]. Including the uncertainty on the IP position, the resolution on the charged-track impact parameter ( $d$ ) is  $\sigma_{r\phi}^d = 7.8 \oplus 33/(p \sin^{3/2} \theta) \mu\text{m}$  (1998) [52] in the plane perpendicular to the beam-axis and  $\sigma_z^d = 9.7 \oplus 33/(p \sin^{3/2} \theta) \mu\text{m}$  (1998) [52] in the plane containing the beam axis ( $\theta$  is the track polar angle with respect to the beam-line).

We define as “high quality” tracks those that satisfy:

- $|\cos \theta| < 0.80$  (barrel region of the detector);
- Distance Of Closest Approach to the IP in the  $r\phi$  plane  $DOCA_{r\phi} < 5 \text{ cm}$ ;
- Distance of Closest Approach to the IP in the  $rz$ -plane  $DOCA_z < 10 \text{ cm}$ ;
- $p_{\perp} > 150 \text{ MeV}/c$  (transverse momentum relative to the beam axis).

## 5.1 Hadronic event selection

---

An event is selected as a candidate hadronic event if it satisfies:

1.  $\geq 5$  high-quality charged tracks. This is used to reject nearly all leptonic  $Z^0$  decays, except for  $\tau^+\tau^-$  events, which can sometimes have 6 tracks or more.
2.  $|\cos \theta_{thrust}| < 0.71$ . The *thrust axis* [85]  $\hat{t}$  of an event is defined as the axis that maximizes the thrust  $T$  of the event:

$$T = \frac{\sum_{clusters} |\vec{p} \cdot \hat{t}|}{\sum_{clusters} |\vec{p}|} \quad (5.1)$$

where the 3-momentum  $\vec{p}$  of the energy cluster is calculated assuming the IP as origin and the pion mass for the particle that caused the energy deposition.  $\theta_{thrust}$  is the angle between the thrust axis (determined from calorimeter clusters) and the beam axis. This rejects events in which a significant fraction of the energy is lost in the endcaps, which are poorly instrumented.

3.  $E_{vis} > 20$  GeV.  $E_{vis}$  is calculated by summing the energy of all high-quality charged tracks, assuming each of them has the charged pion mass of 139.57 MeV. This cut rejects  $\gamma\gamma$  events and leptonic events (including  $\tau^+\tau^-$ ).
4. VXD3 fully operational. This insures that tracks have a good spatial resolution (such as impact parameter resolution), which is critical to reconstruct vertexing information.

The efficiency for selecting a well-contained  $Z^0 \rightarrow q\bar{q}(g)$  event is estimated to be above 96% and independent of quark flavour [86]. The selected sample comprised  $\sim 350$ K events, with an estimated  $0.10 \pm 0.05\%$  background contribution dominated by  $Z^0 \rightarrow \tau^+\tau^-$

## 5.2 Jet Reconstruction

---

Run period	No. of events on tape	No. of selected events
1993-1995	295K	90646
1996	103K	34314
1997-1998	556K	217360
Total	954K	342320

**Table 5.1:** Number of selected hadronic events in the different running periods.

events [86]. Table 5.1 lists the number of selected events per running year. Fig. 5.1 gives the distributions for the number of “quality” charged tracks, the number of charged tracks linked to vertex detector hits, visible energy ( $E_{vis}$ ) and  $\cos(\theta_{thrust})$  for 1993-1998 data after all selection cuts have been applied. We observe good agreement between data and Monte Carlo: discrepancies are taken into account in the systematic errors.

## 5.2 Jet Reconstruction

The algorithm used in this analysis for jet reconstruction is the *JADE* [87] algorithm. For every pair of particles and/or clusters in the calorimeter, the quantity

$$y_{ij} = \frac{2E_i E_j}{E_{vis}^2} (1 - \cos \theta_{ij}) \quad (5.2)$$

is calculated, where  $E_i$  is the energy of the  $i^{th}$  particle,  $\theta_{ij}$  is the angle between the two particles and  $E_{vis}$  the energy of all detected particles. The pair with the minimum  $y_{ij}$  is found. If this value is below a certain threshold  $y_{cut}$ , the pair is combined into a single object with:

$$\vec{p}_k = \vec{p}_i + \vec{p}_j$$

$$E_k = E_i + E_j$$

## 5.2 Jet Reconstruction

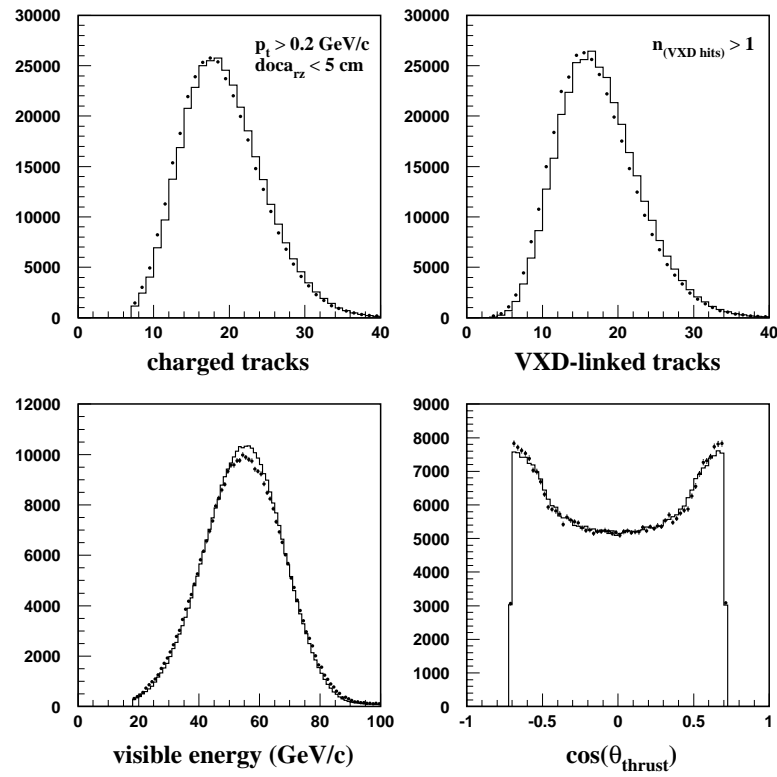


**Figure 5.1:** Distribution of several hadronic event selection variables. Data are represented by points and Monte Carlo by histograms.

## 5.2 Jet Reconstruction

---

and the whole procedure is repeated until  $y_{ij} > y_{cut}$  for every pair. The objects left are defined to be the jets.

This algorithm can be used with different options:

1. it can be used with tracks only: directions and momenta are measured very accurately at SLD, but there are limits in the angular coverage of the CDC which would affect the jet reconstruction, and moreover the contribution from neutral particles would be completely ignored;
2. it can be used with calorimetry clusters only: in this case the resolution would be worse than when using tracking information, but the angular region covered is larger and information from neutrals is included;
3. finally it can be used in a hybrid tracks/clusters scheme, using calorimetry information only for those clusters not associated with tracks (and therefore more likely to be neutrals). In this case however, a good understanding of the calorimetry and of its relation with the tracking system is necessary, and the limitations on the geometrical coverage of the CDC still persist.

The second option has been used in this analysis, for the only reason that it provides better coverage at high  $\cos\theta$ , where the asymmetry signal is higher.

Several studies have been done to optimize the value of  $y_{cut}$  in order to obtain a better reconstruction of the  $b(\bar{b})$  quark direction. For large values of  $y_{cut}$  less jets are found, and those are contaminated by fragmentation and final state QCD radiation. For small values, more jets are found and it becomes difficult to identify the  $b$  quark jet. From Monte Carlo

### 5.3 $B$ Hadron Selection

---

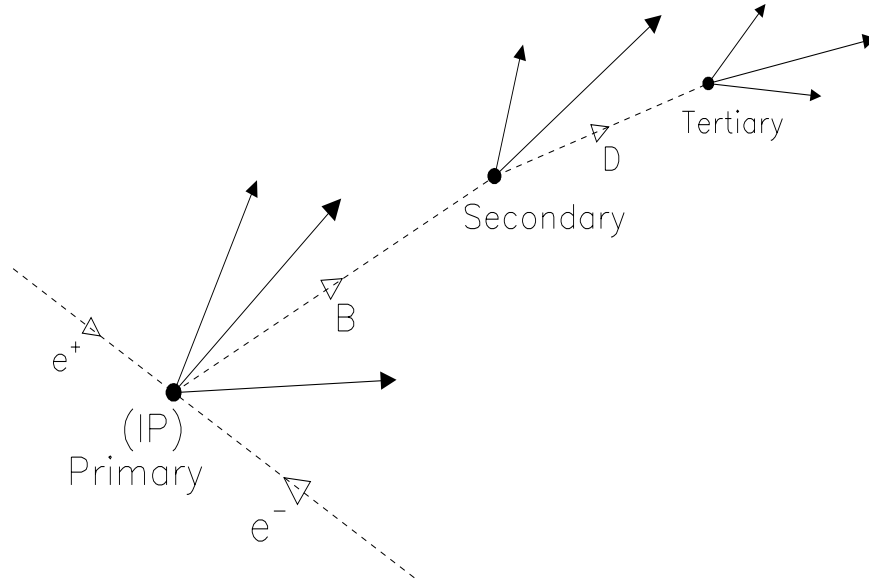


**Figure 5.2:** Tracks produced in a typical  $B$  decay hemisphere.

JETSET studies [54] a value of  $y_{cut} = 0.005$  was chosen for this analysis.

### 5.3 $B$ Hadron Selection

When a  $Z^0$  decays into a  $b\bar{b}$  pair, the two quarks hadronize into two  $B$  hadrons, as well as lighter hadrons, together forming *jets*. Events can be divided into two hemispheres, separated by a plane perpendicular to the thrust axis, and we typically expect one  $B$  hadron into each hemisphere, with tracks coming either from the IP or from a secondary or tertiary vertex. Fig. 5.2 shows a typical reconstructed  $B$  decay hemisphere, where the  $B$  hadron decays into a  $D$  hadron and other tracks, and the  $D$  hadron subsequently decays into three visible tracks (neutral particles are not shown).

Semileptonic decays can either be direct, when the lepton track comes from the  $B$  secondary vertex, or cascade, when the  $B$  hadron decays into a  $D$  hadron which then decays

### 5.3 *B* Hadron Selection

---

into a lepton. These two classes of events give opposite sign contributions to the polarized forward-backward asymmetry and should therefore be well separated.

*B* hadrons are tagged by dividing the event into two hemispheres (as described above), and by applying a topological vertexing algorithm [84] to a well selected set of tracks in each hemisphere. A more stringent set of cuts is applied to select these “flavour-tagging” tracks (a subset of the “quality” tracks used for hadronic event selection), which need to satisfy (1996-1998 data):

- $|\cos \theta| < 0.87$ ;
- at least 2 hits in VXD3 and 23 hits in the CDC;
- a combined CDC/VXD3 track fit quality of  $\chi^2/N_{dof} < 8$ ;
- a momentum range  $0.25 < p < 55$  GeV/c;
- an impact parameter less than 0.3 cm in the  $r\phi$  plane and less than 1.5 cm along the  $z$  axis;
- a transverse impact parameter error of less than  $250\mu\text{m}$ .

#### 5.3.1 Vertexing algorithms

Two vertexing algorithms have been used in this analysis, one for the 1993-96 data and an upgraded version for the 1997-98 data. A brief description will be given of each of them.

In the original version of the package, vertices are reconstructed in a 3-D coordinate space

### 5.3 *B* Hadron Selection

---

by defining a vertex function  $V(\vec{r})$  at each position  $\vec{r}$  [84]. The helix parameters for each quality track are used to represent the 3D track trajectory as a Gaussian probability tube  $f_i(\vec{r})$ , where the width of the tube is the uncertainty in the measured track location close to the IP. Another function is also introduced to describe the position of the IP as a Gaussian ellipsoid, centred on the IP.  $V(\vec{r})$  is defined as a function of the  $f_i(\vec{r})$ , such that it is larger in regions of high track multiplicity. Maxima are found in  $V(\vec{r})$  and clustered into resolved spatial regions. Tracks are then uniquely associated to one or the other of these candidates with an iterative procedure that eventually reconstructs the entire geometry of the event, distinguishing primary from secondary and possibly tertiary vertices according to their relative distances from the IP. The most significant vertex (the one with the highest probability  $V(\vec{r})$ ) is chosen as “seed” vertex and the axis connecting it to the IP is drawn (see fig. 5.3). Every track which is not directly associated to this vertex is characterized by: (i) a 3-D impact parameter  $T$ , (ii) the distance  $L$  from the IP of the point of closest approach of the track to the vertex axis, taken along the axis itself, and finally (iii) the ratio of the two quantities  $L/D$ , which gives the relative decay length of the track with respect to the vertex flight distance.

Tracks satisfying the cuts:  $T \leq 1$  mm,  $L \geq 0.5$  mm,  $L/D \geq 0.3$  are attached to the seed vertex to form a secondary vertex. The total efficiency for reconstructing a secondary vertex in a  $Z^0 \rightarrow b\bar{b}$  event hemisphere is about  $\sim 50\%$  (in charm and light quark hemispheres it is about 15% and 3% respectively) [84].

### 5.3 *B* Hadron Selection

---

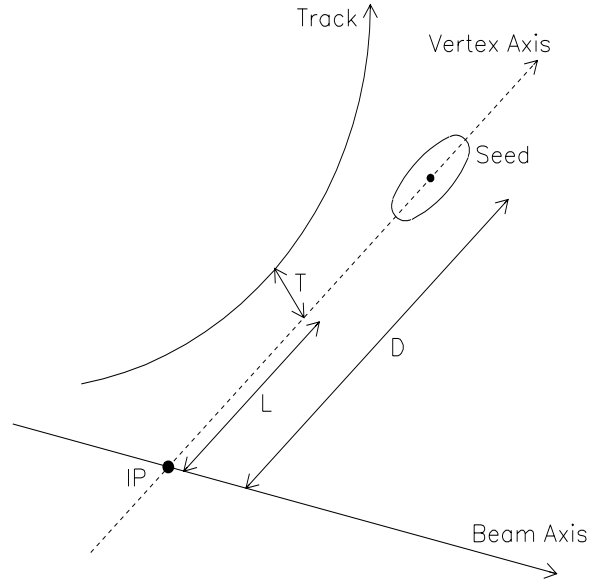


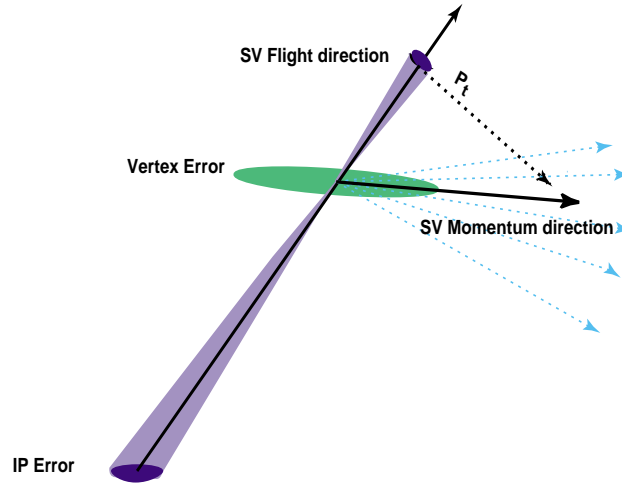
**Figure 5.3:** Topological parameters of a track:  $D$  is the distance of the secondary seed vertex from the IP along the line connecting them;  $T$  is the transverse distance of the track from the vertex axis calculated at the point of closest approach (POCA) and finally  $L$  is the distance from the IP of the projection of the POCA on the vertex axis.

#### Reconstruction of the vertex mass

One of the variables used in this analysis to select  $B$  events is the invariant mass of the reconstructed secondary vertices. Tracks are assigned the mass of a charged pion and a first “raw” value of the vertex mass is calculated out of the total momentum  $\vec{P}$  and energy  $E$  of these tracks according to:

$$M_0 = \sqrt{E^2 - P^2}.$$

This is then corrected to account partially for the contribution of neutral and missing charged particles. By comparing the vertex flight path and the momentum sum of the tracks associated to the secondary vertex, one calculates a minimum amount of missing transverse momentum to be added to the raw mass (see fig. 5.4). The new value therefore

5.3 *B* Hadron SelectionFigure 5.4: Illustration of the method to calculate  $P_t$ .

becomes:

$$M_{vtx} = \sqrt{M_0^2 + P_t^2} + |P_t|, \quad (5.3)$$

where  $P_t$  is the minimum track momentum necessary for the realignment of the vertex momentum and vertex flight directions, calculated by allowing the locations of the IP and the vertex to float to any pair of locations within the respective one-sigma error ellipsoids. We require the transverse momentum contribution to be less than the initial mass of the secondary vertex, to ensure that poorly measured vertices in light quark ( $uds$ ) events do not leak into the final sample by adding a large  $P_t$ . Distributions for the two mass definitions are shown in fig. 5.5 for MC and data events, with the MC flavour components separated. From the bottom figure it is evident how the  $uds$  component is isolated below  $0.55 \text{ GeV}/c^2$ , whereas charm hemispheres mostly populate the region between  $0.55$  and  $2 \text{ GeV}/c^2$ . The standard cut used for  $b$  tagging is that an event should contain a hemisphere with  $M_{vtx} \geq 2 \text{ GeV}/c^2$ , giving a 98% pure  $b\bar{b}$  event sample, with selection efficiency of

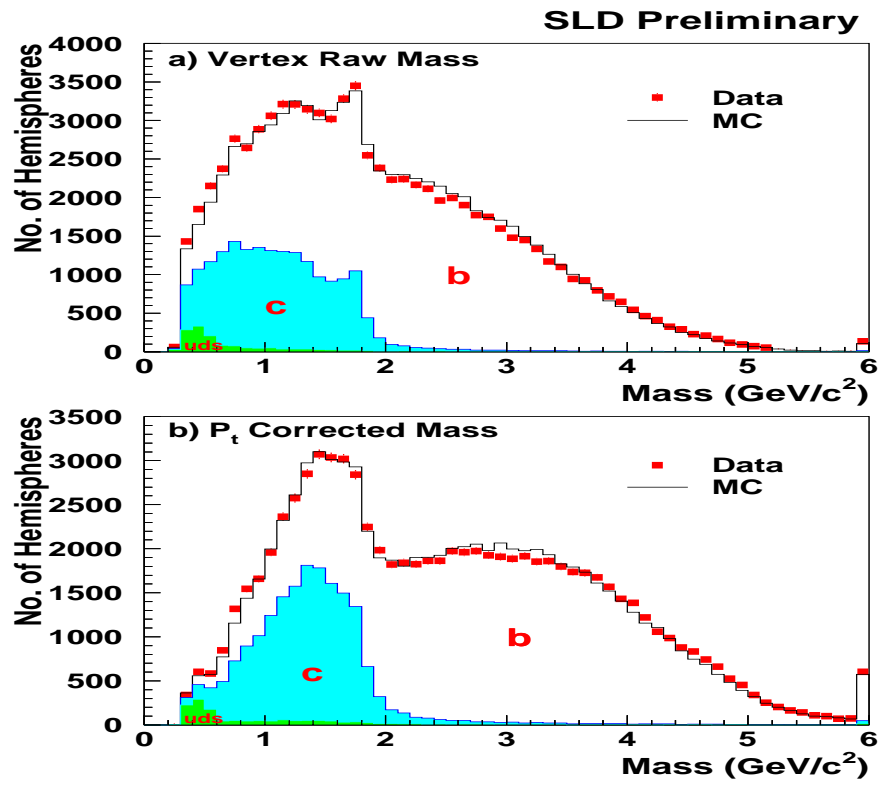
5.3  $B$  Hadron Selection

Figure 5.5: Distributions of the reconstructed raw and  $P_t$ -corrected vertex masses for data (dots) and Monte Carlo (histogram). Also shown is the Monte Carlo flavour composition. [88]

### 5.3 *B* Hadron Selection

---

about 50% (for a generic *B* hadronic event).

#### The “ghost” track algorithm

A significant improvement in impact parameter resolutions has been recently (1999) accomplished thanks to the introduction of a new track extrapolation program and of a Kalman filter algorithm [89] for CDC/VXD fit  $\chi^2$  calculation, which models better effects of multiple scattering in the detector material. The miss-distance near the beam line of the two back-to-back tracks in  $Z^0 \rightarrow \mu^+\mu^-$  events gives a clean estimator of the asymptotic track impact parameter resolution at high momentum, independent of the knowledge of the beam spot. Taking the projections of this quantity in the  $r\phi$  and  $rz$  planes, the impact parameter resolutions improved from [52]

$$\sigma_{r\phi} = 10.7 \mu\text{m} \quad \sigma_{rz} = 23.5 \mu\text{m} \quad (\text{original track fitter with VXD3}),$$

to

$$\sigma_{r\phi} = 7.8 \mu\text{m} \quad \sigma_{rz} = 9.7 \mu\text{m} \quad (\text{new track fitter with VXD3}).$$

Taking advantage of this improvement, a new algorithm has been developed at SLD to reconstruct *B* decays. This algorithm relies on the long *B* and *D* lifetimes and the kinematic fact that the large boost of the *B* decay system carries the cascade charm decay downstream from the *B* decay vertex. Monte Carlo studies show that in *B* decays producing a single *D* meson the cascade *D* decays on average  $4200\mu\text{m}$  from the IP, while the intermediate *B* vertex is displaced on average only  $46\mu\text{m}$  transversely from the line joining the IP to the *D* decay vertex. This kinematic stretching of the *B* decay chain into an

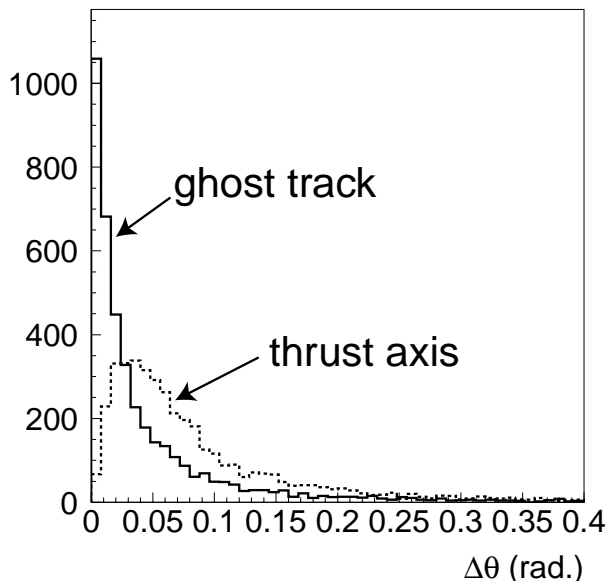
### 5.3 *B* Hadron Selection

---

approximately straight line is exploited by what is called the “ghost” track algorithm [90]. In the first stage, the best estimate of the straight line from the IP directed along the *B* decay chain is found. This line is promoted to the status of track by assigning it a finite width. This track, regarded as the “resurrected” image of the decayed *B* hadron, is called the “ghost” track. In a second stage, the selected tracks are vertexed with the “ghost” track and the IP to build up the decay chain along the ghost direction. Both stages will now be described in more detail.

Given a set of tracks in a jet or hemisphere, a new track *G* is created, which is initially identical to the jet or thrust axis and has a constant resolution width in both  $r\phi$  and  $rz$ . For each track  $i$ , a vertex is formed with the track *G* and the vertex location  $\vec{r}_i$ , fit  $\chi_i^2$  and  $L_i$  are determined, where  $L_i$  is the longitudinal displacement from the IP to  $\vec{r}_i$  projected onto the direction of the track *G*. The summed  $\chi^2$  ( $\chi_S^2$ ) is then formed, such that, when the direction of *G* is varied, the minimum of  $\chi_S^2$  provides the best estimate of the *B* decay direction. The width of the track *G* is then set such that the maximum  $\chi_i^2 = 1.0$  for all potential *B* decay candidate tracks ( $L_i > 0$ ).

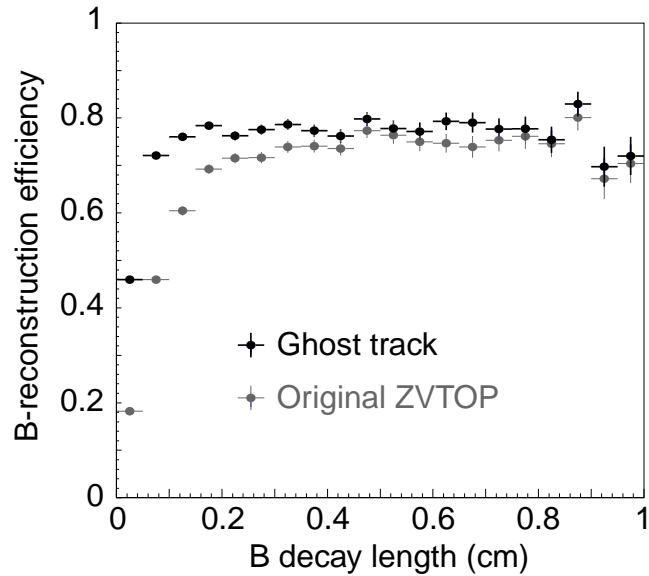
The second stage of the algorithm begins by defining a fit probability for a set of tracks to form a vertex with each other and with the ghost track (or IP). This probability then measures the likelihood of the set of tracks both belonging to a common vertex and being consistent with the ghost track. These probabilities are determined from the fit  $\chi^2$  which is in turn determined algebraically from the parameters of the selected tracks and the ghost track. The aim is now to find the most probable track-vertex associations. For a set of *N* tracks there are initially *N*+1 candidate vertices (*N* 1-prong secondary vertices

5.3 *B* Hadron Selection

**Figure 5.6:** Residual distributions between a true  $B$  direction and a “ghost” track/thrust axis. The “ghost” track gives a better  $B$  direction estimate than the thrust axis [52].

and the IP). Fit probabilities for all candidate vertex pairs fitted together with the ghost track are calculated. Probabilities of each track fit with the IP ellipsoid are calculated too. The highest probability is found and the corresponding candidate vertex pair of tracks are tied together to form a new candidate vertex for all future computations. This modifies the set of all candidate vertices and the procedure is repeated with the new set. At each iteration of combining the maximum probability contributors, the number of candidate vertices decreases by one. The iterations continue until the maximum probability is less than 1%. At this point the tracks and the IP have been divided into unique subsets by the associations thereby defining topological vertices. The ghost track algorithm improves the efficiency of  $B$  reconstruction especially at short decay length (see fig. 5.7).

The new “ghost” track algorithm has been used in this analysis for the 1997-98 data sample, and new versions of the vertex mass reconstruction procedure as well as of the L/D

5.3 *B* Hadron Selection

**Figure 5.7:** *B* reconstruction efficiency curves as a function of the *B* decay length. Black points indicate the ghost track algorithm and grey points the original topological vertexing algorithm. The ghost track algorithm improves the efficiency along the entire *B* decay length, in particular at short decay length [52].

geometrical definition had to be devised to be consistent with the new vertexing package output. The hemisphere raw tagging mass is now reconstructed out of all secondary tracks that have been associated to either the secondary or tertiary decay vertices and that satisfy  $T < 0.1$  cm and  $L/D \geq 0.25$  (see fig. 5.3), where  $D$  is the distance of the secondary vertex from the IP. We furthermore require that there are at least two such tracks. These tracks are then refitted together in a single vertex whose mass is then calculated with the same procedure described before, by assigning to every track the mass of a pion and correcting for the missing transverse momentum provided by neutral particles (or missing charged particles). The efficiency for tagging a *B* hadron ( $M_{vtx} \geq 2$  GeV/ $c^2$ ) in a hemisphere containing a muon track improves from  $\sim 56\%$  to about  $67\%$ , while the purity changes from  $98.5\%$  to  $95.5\%$  because of a slightly larger contamination of charm events at high

## 5.4 Muon Selection

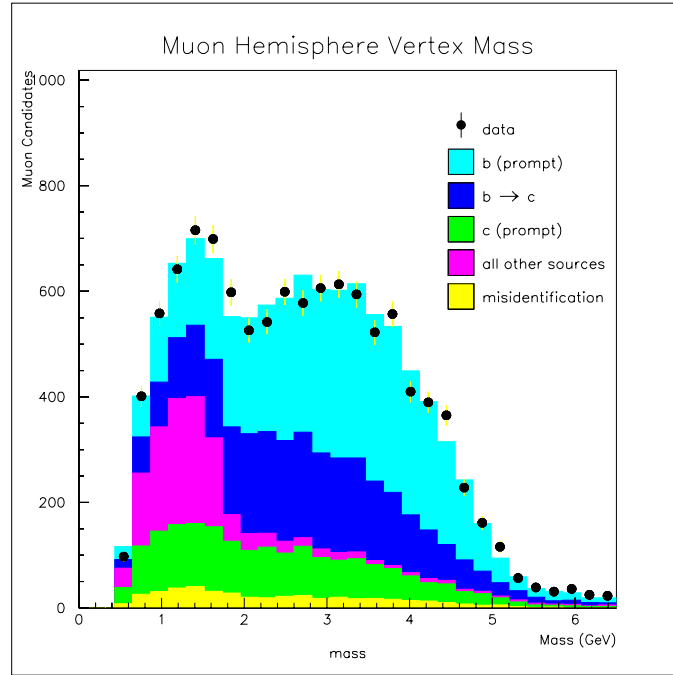


**Figure 5.8:** Vertex mass distribution for muon hemispheres in 1997-98 data (dots) and Monte Carlo (histogram).

mass (see fig. 5.8). For  $c\bar{c}$  events the tag efficiency ( $0.55 < M_{vtx} < 2 \text{ GeV}/c^2$ ) goes from  $\sim 24\%$  to  $\sim 37\%$  and the purity from  $\sim 36\%$  to  $\sim 39\%$ .

## 5.4 Muon Selection

Muons are identified at SLD by combining WIC and CRID information [91]. Some peculiar characteristics of muons simplify their identification in the WIC: their average lifetime is rather long, and due to the absence of nuclear interactions and small radiation losses, they are capable to survive larger depths of material compared to other particles and therefore penetrate the outermost parts of the detector.

## 5.4 Muon Selection

---

Since muons are not produced in  $Z^0$  hadronic decays in the same quantities as pions and kaons, background suppression is particularly important. There are different kinds of backgrounds in a detector like SLD:

- first of all charged pions and kaons can reach the WIC without decaying (*punch through*), and therefore show the same behaviour as muons. Even if the probability is rather small, this is compensated by the large number of kaons and pions produced in hadronic events (muons are only about 1% of the total sample of charged non-leptonic tracks).
- Pions and kaons can decay into a muon-neutrino pair before reaching the WIC. If the muon is sufficiently energetic it can traverse the WIC with a similar direction to the decayed hadron.
- The tails of hadronic showers can reach the WIC, contributing to misidentification;
- and finally cosmic muons and accelerator background muons can be confused with muons from the IP, but they can be excluded by cutting on the impact parameter.

The probability that a hadron survives  $x$  interaction lengths is approximately  $e^{-x}$ . Since there are 3.5 interaction lengths between the CDC and the WIC, and the WIC itself corresponds to 4 interaction lengths, the probability for a hadron to reach the WIC is roughly 3% and the probability to traverse it is only 0.06%. Furthermore, the momentum spectrum of kaons and pions *punch through* is much softer than the spectrum of muons coming from heavy quark decays. Background discrimination therefore becomes more important for momenta  $\leq 5$  GeV/c.

## 5.4 Muon Selection

---

### 5.4.1 Muon identification in the WIC

Muon identification is accomplished by measuring charged tracks in the CDC and correlating these tracks with hits in the WIC. There are several steps to be followed [54]:

1. each track measured in the CDC is extrapolated, with measurement and multiple scattering errors, to the inside of the WIC;
2. all WIC hits within four standard deviations of the extrapolated track are grouped into track patterns;
3. each track pattern is fitted, and those with a large  $\chi^2$  are discarded;
4. the extrapolated track is compared to each surviving hit pattern and favourable matches are saved;
5. the best combinations are kept in order of decreasing match quality.

Each WIC hit is represented as a line segment in space. The point of closest approach of the line of the hit to the extrapolated track direction is calculated. If the point is within 4 sigma bounds in each dimension of the extrapolated errors (on the assumption of fully correlated position and direction errors), the hit is kept. Hits are then grouped by parallel direction and combinations (*sub-patterns*) are found by requiring only one hit per chamber layer and successive hits in alignment within certain errors. Subpatterns for each group of hits in different directions are then combined into *patterns*. These patterns are then fitted together with the WIC fitter, which calculates a  $\chi^2$  by extrapolating a trajectory through the WIC, (taking into account the magnetic field, energy losses and correlations

## 5.4 Muon Selection

---

in the error matrix due to multiple scattering), and comparing it to the WIC hits. Fit parameters are found by an iterative search for the  $\chi^2$  minimum, after discarding patterns with a  $\chi^2/ndf > 5$ . The outputs of the WIC fitter are position and direction offsets of the best fit of a track through the hit pattern and the corresponding error matrix. Since the fitter coordinate system is defined relative to the point and direction of the track extrapolation, zero fit values correspond to a fit lined up with the extrapolated track. To form a track-matching  $\chi^2$  it is then necessary to add the extrapolated track error matrix and the fit error matrix together in the same coordinate system. The  $\chi^2$  per degree of freedom is then:

$$\chi^2 = \frac{1}{n} \sum_{i,j=1}^n p_i W_{ij} p_j,$$

where  $W$  is the weight matrix, equal to the inverse of the sum of the extrapolation and fit error matrices,  $p$  the fit parameters and  $n$  the number of degrees of freedom. Since the fitter operates in two dimensions,  $n$  is usually equal to 4, unless some information is missing. Patterns with a  $\chi^2 > 6$  are discarded. In case of ambiguities, when the same set of WIC hits has an acceptable match to more than one track or one track has an acceptable match to two distinct sets of WIC hits, the following criteria are adopted:

1. if two matches have different numbers of degrees of freedom, the one with the larger number is considered better;
2. if they have the same number of degrees of freedom, the match with the smaller  $Q$  is considered better, where  $Q$  is defined as

$$Q = \chi^2 - An,$$

## 5.4 Muon Selection

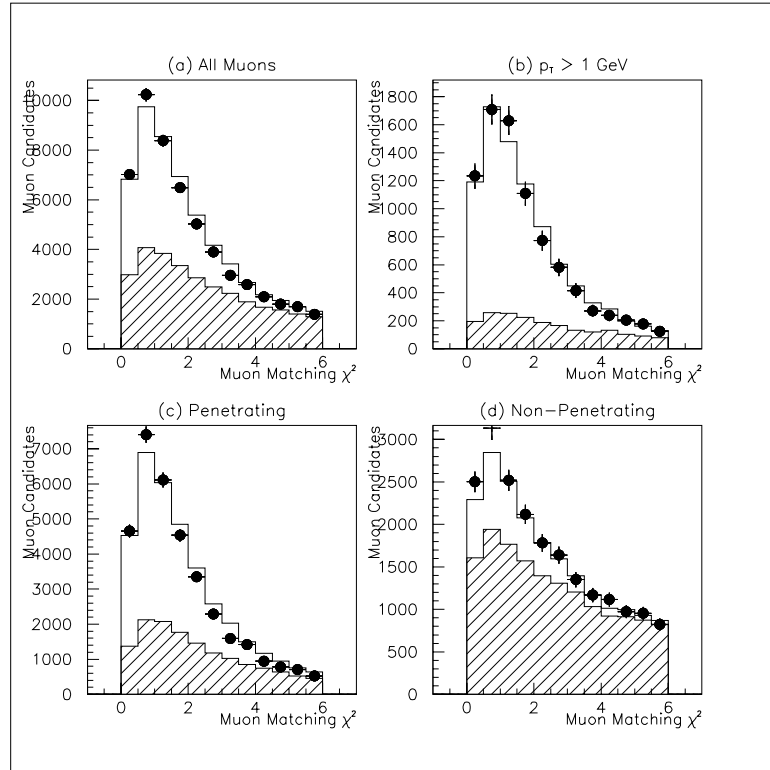


**Figure 5.9:** Muon matching  $\chi^2$  distributions for hadronic events after applying various cuts. Shown is data (points) and simulation of all muons (histogram) and background (hashed). (a) All muon candidates. (b) A 1 GeV/c cut in transverse momentum isolates muons from heavy quark decays and therefore produces a smaller fraction of background. (c) Penetration requirements remove much of the background. (d) Muon candidates that fail the penetration requirements are dominated by background [91].

where  $n$  is the number of WIC hits, and  $A$  is a constant factor set to 0.1 (*hit bonus*).

All surviving track-WIC matches are sorted by decreasing quality and the best match is identified as a muon candidate. The rest of the matches are processed in order of quality and any match that uses more than 67% of the hits or is associated with the same track as a better match is discarded. Remaining matches are considered possible muon candidates.

Greater purity can be achieved if each muon candidate is tested to see if it fully penetrates the WIC. The WIC fit of each candidate is therefore extrapolated through all the layers of

## 5.4 Muon Selection

---

the WIC, and any chamber intersected is checked for a hit, taking into account inefficiencies due to gaps or dead areas. If a muon candidate has at least two hits in the last four active strip layers it intersects, the candidate is marked as fully penetrating.

Shown in fig. 5.9 is the muon matching  $\chi^2$  for muon candidates in hadronic events under various cuts. The entire  $\chi^2$  is well simulated, including the signal peak at low  $\chi^2$  and the background in the tails. At low momentum the  $\chi^2$  is dominated by multiple scattering, whereas at high momentum it is dominated by tracking resolution. The  $\chi^2$  distribution is independent of momentum, confirming that these two effects have been correctly accounted for in the matching algorithm.

### 5.4.2 Muon Identification in the CRID

The use of CRID information is particularly effective for hadronic background rejection at low energies and more specifically for the separation of muons from pions and kaons *punch through*, when these latter ones traverse the CRID reaching the WIC or decay into muons just outside of the CRID. In this last case, either it is impossible to reconstruct the muon track, if its direction differs from that of the decayed hadron, or the track of the muon is associated to that of the hadron, which is however identified as such by the CRID.

CRID information is stored in likelihood functions for every particle hypothesis and only the difference between these quantities is of physical interest. Information from the CRID gas section only has been used in the muon identification algorithm for this analysis. This is in fact more accurate, and furthermore, information from the liquid radiator, being lim-

## 5.4 Muon Selection

---

ited to low momenta, is here marginal, since muons with  $p < 2$  GeV/c do not have enough energy to traverse the WIC.

### The CRID likelihood functions

Details of the procedure used to derive the likelihood functions have been given elsewhere [92]; only a brief description will be presented here.

The method is based on the observed photoelectron density in the coordinate space  $(x, y, z)$  or in the Čerenkov space  $(\theta, \phi, t)$ , where  $\theta$  and  $\phi$  are the spherical coordinates of the photon with respect to the track and  $t$  is the depth in the photon detector measured along the radius.

The hypotheses for the tracks in an event take into account the total number of observed photoelectrons and their spatial distribution. Let  $\bar{n}$  be the number of photons predicted by a certain hypothesis on the nature of the tracks,  $n$  the observed one and  $P(\vec{r}) = P(x, y, z)$  the probability for a photoelectron to be within a volume  $d^3\vec{r}$ : then  $\bar{n}P(\vec{r})$  is the number of photoelectrons predicted in that volume. The total probability (for all tracks) to obtain  $n$  photoelectrons distributed according to the data is the *likelihood*  $L$ . The best hypotheses for the single particles are those that maximize this function.

The likelihood  $L$  therefore depends on all the different hypotheses for all the charged tracks in the event. Since this would be too complicated to solve, at every step of the calculation the hypothesis for a single track is varied while those for all the other tracks are kept fixed. In this way there is no opportunity to compare hypotheses for two different particles, but

## 5.4 Muon Selection

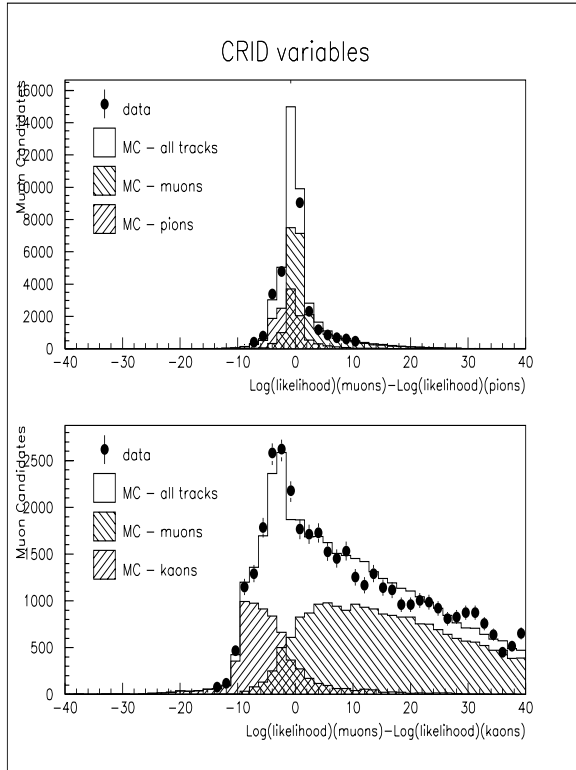


**Figure 5.10:** Differences in the logarithms of the likelihood function for muons and pions (top) and muons and kaons (bottom), for tracks with momentum  $> 2 \text{ GeV}/c$  [91].

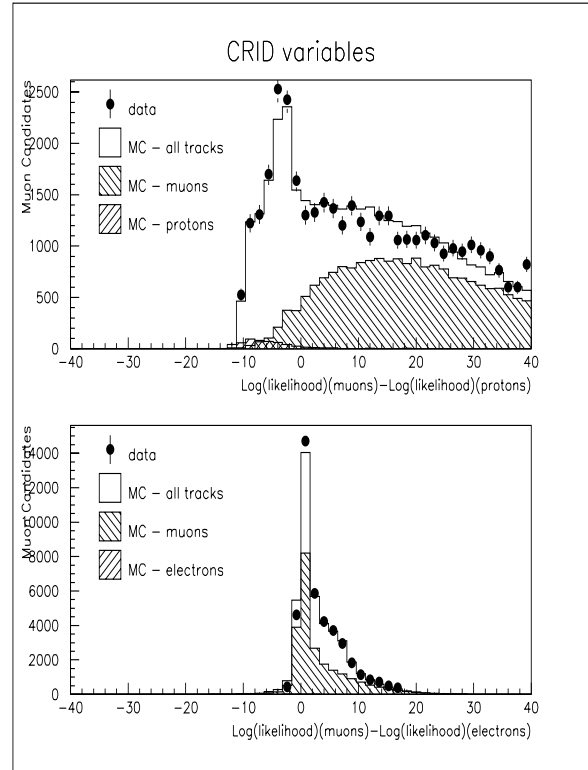


**Figure 5.11:** Differences in the logarithms of the likelihood function for muons and protons (top) and muons and electrons (bottom), for tracks with momentum  $> 2 \text{ GeV}/c$  [91].

the process is much simplified. The procedure is iterated until convergence.

Shown in fig. 5.10 is the difference in the logarithms of the likelihood functions for muons and pions and for muons and kaons, for tracks with  $p > 2 \text{ GeV}/c$ . Data and MC predictions are in good agreement: the muon/kaon separation is very neat, whereas the muon/pion is more difficult (although a better discrimination can be achieved at lower momenta, where threshold effects are more significant).

The separation of muons from protons and electrons is shown in fig. 5.11: background contaminations are in this case very small and not much information is given by the

## 5.4 Muon Selection

---

likelihood functions.

The CRID variables used in the muon identification algorithm are therefore only:

- $LLIK_\mu - LLIK_\pi$  (for pion rejection) and
- $LLIK_\mu - LLIK_k$  (for kaon rejection).

### 5.4.3 The Muon-*id* Algorithm

Along with the CRID likelihood variables, the other quantities used in the muon identification at SLD are:

- MISSPROB: the probability for a given penetrating track not to leave hits in a number of layers beyond 6.5 interaction lengths from the IP (or 4 layers at normal incidence) equal to the number of layers effectively missed (taking into account the average layer efficiency in the WIC). Most of the tracks with probability less than 4% come from the background.
- NMISS4L and NMISS6L: the number of hits missed by the track in the last 4 or 6 WIC layers. Most of the background is rejected by requiring at least 3(4) hits in the last 4(6) layers.
- CHI2MTCH: the CDC/WIC matching  $\chi^2$ , which gives information on the difference in direction between the track extrapolated from the CDC and the WIC fit, and therefore helps to distinguish muons coming from pions and kaons decayed before reaching the CRID. The tails of the distribution are dominated by backgrounds. The

## 5.4 Muon Selection

---

WIC  $\chi^2$  fit alone (CHI2WIC) gives some information too, even if less discriminant than CHI2MTCH.

- NWICASS: the number of hits in the WIC path associated to a certain track. Low values of this variable correspond to background particles that do not make it across the WIC.
- QUAL: a variable which contains information on the degree of penetration and isolation of the track. It is equal to 0 if the track is isolated and penetrating, to 1 if the track is not isolated but penetrating, 2 if the track is not penetrating but only isolated and 3 if the track is neither isolated nor penetrating. Other values indicate errors or misidentification.
- KMUONID: used for muon identification in the LAC, and separation from the pion background. It is the output of a neural net whose inputs are: the track momentum, the energy deposited in 4 calorimeter layers and the width of the energy cluster in  $\theta$  and  $\phi$ .

Since the discriminating power of the CRID likelihood variables strongly depends on the particle momentum, the cuts on all these quantities have been implemented in 8 different momentum intervals. Furthermore, since CRID information is only present in about 80% of the cases, the samples of tracks with and without this information have been kept separated. 16 sets of data have therefore been used to define the identification cuts and the procedure followed has been to maximize in each of these sets the product of the efficiency and purity ( $\epsilon \times \pi$ ), where the efficiency is given by the ratio of muons correctly

## 5.4 Muon Selection

---

MC Source	Track rejection due to cuts on	
	$LLIK_\mu - LLIK_\pi$ (%)	$LLIK_\mu - LLIK_K$ (%)
$\pi$	37%	9%
$K$	41%	51%
$p$	57%	52%
$e$	5%	5%
$\mu$	5%	2%

**Table 5.2:** Background rejection with cuts on  $LLIK_\mu - LLIK_\pi$  for  $2 < P < 6$  GeV/c and with cuts on  $LLIK_\mu - LLIK_K$  for  $P > 2$  GeV/c, for different particle types [91].

identified over all muon tracks that have been linked to hits in the WIC, and the purity is the ratio between identified muons and all tracks passing the identification cuts.

The variables have first been studied one by one, looking for a cut that maximized  $\epsilon \times \pi$  in that particular case, then all the cuts found have been optimized again with an iterative procedure to find the best combination with a purity  $\geq 50\%$ . The algorithm has been extended from the initial angular coverage up to  $|\cos\theta| < 0.6$  to  $|\cos\theta| < 0.7$ , taking into account that this is a sort of “boundary” region at the edge of the barrel, and consequently the number of hits per track in the WIC is smaller for geometrical reasons and the CRID response too is slightly different. The optimization of the cuts has thus been performed independently in this region.

Shown in table 5.2 are the results of a MC study on the power of background rejection of the CRID likelihood functions. Cuts on  $LLIK_\mu - LLIK_\pi$  eliminate  $\sim 37\%$  of the pion background, while cuts on  $LLIK_\mu - LLIK_K$  alone can reject more than half of the kaon and proton contamination, with a loss in signal of only 5%.

## 5.4 Muon Selection

---

MC source	all tracks		$p > 2 \text{ GeV} \ \& \  \cos \theta  < 0.7$		tracks with WIC hits		tracks identified as $\mu$	
$\pi$	702141	(99.1%)	195214	(98.9%)	2704	(94.2%)	443	(80.3%)
$p$	1778	(0.3%)	1165	(0.6%)	22	(0.8%)	5	(0.9%)
$K$	2028	(0.3%)	644	(0.3 %)	5	(0.2%)	1	(0.2%)
$e$	669	(<0.1%)	159	9<0.1 %)	1	(< 0.1%)	/	/
$\mu$	1416	(0.2%)	226	(0.1 %)	139	(4.8%)	102	(18.5%)
other	126	(< 0.1%)	9	(<0.1 %)	/	/	/	/
Tot MC	708158		197417		2871		551	
Tot DT	148104		43331		701		148	

**Table 5.3:** Results of the muon identification algorithm test on a pure sample of pions selected from  $K_s^0$  decays (1996-1998 data). The composition of the MC sample as a function of different cuts is shown. Percentages are relative to the sample selected with a particular choice of cuts.

### Pion background rejection

The power of background rejection of the muon identification algorithm has been tested on two different samples of pion tracks in data and MC, selected respectively from  $K_s^0 \rightarrow \pi^+ \pi^-$  and 3-prong  $\tau$  decays.

The first sample has been obtained by reconstructing vertices formed by opposite charge tracks in the CDC satisfying these kinematic criteria:

- the angle between the track and the total vertex momentum has to be less than 0.2 mrad;
- the normalized vertex decay length has to be greater than 4;
- the normalized track distance of closest approach from the IP has to be less than 6;
- the difference between the invariant mass of the pair of tracks and the mass of the  $K_s^0$  has to be less than 20 MeV.

## 5.4 Muon Selection

---

The pion sample obtained is 99.1% pure, with a 0.2% contamination of muons. Considering only tracks with  $p > 2$  GeV/c and within  $|\cos\theta| < 0.7$  the purity goes down to 98.9% with a muon contamination around 0.1%. Shown in table 5.3 is the variation in the sample composition when different cuts are applied, requiring first that the track be successfully linked to WIC hits and then that it is identified as a muon. Only 0.28% of the pions in the muon angular acceptance and with momentum greater than 2 GeV/c survives the muon-id cuts. The difference in the misidentification rates for tracks in data and in the Monte Carlo gives an estimate on how well we are able to simulate the background level in the SLD MC. The results of this analysis are:

$$R_{bkg}(data) = (0.342 \pm 0.028)\% \quad (5.4)$$

$$R_{bkg}(MC) = (0.279 \pm 0.012)\%$$

$$Rel. Diff. = (20.14 \pm 9.88)\%$$

A similar study was conducted on a sample of pions from 3-prong  $\tau$  decays. These were selected using a filter that combines information from tracking, calorimetry and geometry of the jets in the event [93]. The results for the 1996-1998 data sample are given in table 5.4.

The initial sample is  $\sim 92\%$  pure, with a contamination of  $\sim 2\%$  from protons and 6% from electrons. The misidentification rates (ratio of tracks with  $P > 2$  GeV/c and  $|\cos\theta| < 0.7$  passing the muon-id cuts) for data and MC are:

$$R_{bkg}(data) = (0.278 \pm 0.059)\% \quad (5.5)$$

$$R_{bkg}(MC) = (0.263 \pm 0.013)\%$$

## 5.4 Muon Selection

---

MC source	all tracks		$p > 2 \text{ GeV} \ \& \  \cos \theta  < 0.7$		tracks with WIC hits		tracks identified as $\mu$	
$\pi$	192925	91.8%	146290	94.5%	1149	87.6%	317	77.9%
$p$	3860	1.8%	3124	2%	31	2.4%	8	2%
$K$	275	0.1%	22	<0.1 %	/	/	/	/
$e$	12614	6%	5139	3.3 %	25	2%	3	0.7%
$\mu$	407	0.2%	208	0.1 %	107	8%	79	19.4%
other	5	< 0.1%	/	/	/	/	/	/
Tot MC	210086		154783		1312		407	
Tot DT	10697		7909		85		22	

**Table 5.4:** Results of the muon identification algorithm test on a sample of pions from 3-prong  $\tau$  decays (1996-1998 data). The composition of the MC sample as a function of different cuts is shown.

$$Rel. \ Diff. = (5.54 \pm 22.2)\%$$

In this case there is better agreement between background rates in data and MC, although the very low statistics available severely limits the validity of the results. Furthermore this sample is not directly comparable to the one from  $K_s^0$  decays because of a substantial difference in the momentum spectrum of the pion tracks (which in this case extends up to 50 GeV/c whereas in the previous one it only reaches up to 15 GeV/c). In conclusion, we have assumed the results from the  $K_s^0$  sample as representative of this study, with the consequence that we have observed a discrepancy of about  $(20 \pm 10)\%$  in the background level between data and Monte Carlo, with the level in the simulation being systematically lower than in the data. This effect has been accounted for in the analysis, as will be described in the next chapter.

### Efficiency and Purity of the muon identification algorithm

A definition of efficiency depends on the events one is interested in in a certain analysis. Muons coming from light hadrons, for example, are part of the background in

## 5.4 Muon Selection

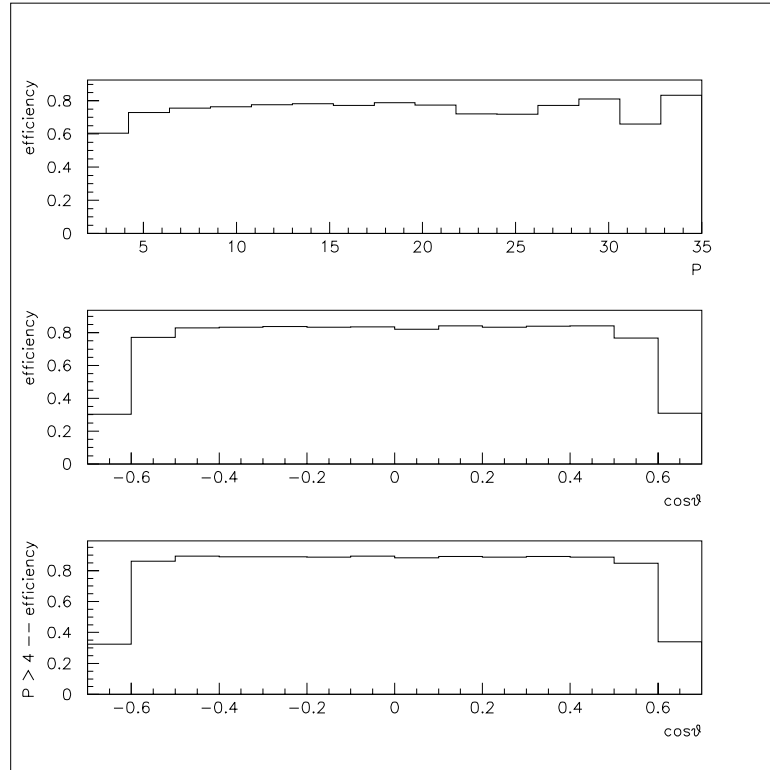


**Figure 5.12:** Efficiency of the algorithm for muon identification as a function of the track momentum (top) and of the polar angle (center and bottom) for  $p > 2$  and  $p > 4$  GeV/c respectively.

this study. Even when a muon decays from a pion inside the DC, tracking algorithms cannot often distinguish the two tracks, which will be considered in the Monte Carlo as of one or the other origin depending on the point where the decay happened (internal or external layers).

Shown in fig. 5.12 is the efficiency for identifying muons from  $B$ ,  $D$  decay with momentum greater than 2 GeV/c and within  $|\cos \theta| < 0.6$ . In the top plot is the efficiency as a function of momentum, which is roughly constant above 4 GeV/c. In the center and bottom plots are the efficiencies as a function of the polar angle, for momenta greater than 2 or 4 GeV/c respectively. One can clearly see the region of low efficiency corresponding

## 5.4 Muon Selection

---

Muons from $B, D$ decays ( $ \cos\theta  < 0.6$ )		
	$p > 2$ GeV/c	$p > 4$ GeV/c
Matching efficiency	88.7%	92.6%
Cut efficiency	89.7%	94.9%
Total efficiency	79.6%	87.9%

**Table 5.5:** Identification efficiencies for muons coming from heavy hadron decays [91].

year	data	MC
1993	2190	8922
1994-5	4901	17250
1996	2725	7039
1997-8	18474	90215
TOT	28290	123426

**Table 5.6:** Number of selected hemispheres with a muon track in  $Z^0$  hadronic events per running year.

to the 45 degree chambers. Listed in table 5.5 are the efficiencies of the identification algorithm for muons coming from  $B$  and  $D$  decays and for all MC muons for different cuts in momentum. Efficiencies and purities for tracks with and without CRID information are shown in fig. 5.13. The efficiency is here calculated with respect to CDC tracks already matched with hits in the WIC. The introduction of CRID information allows for a much higher purity especially at low momentum (where the improvement is  $\sim 25-30\%$ ).

Table 5.6 lists the number of hemispheres with an identified muon track in selected hadronic events per running year (total data sample for this analysis).

## 5.4 Muon Selection

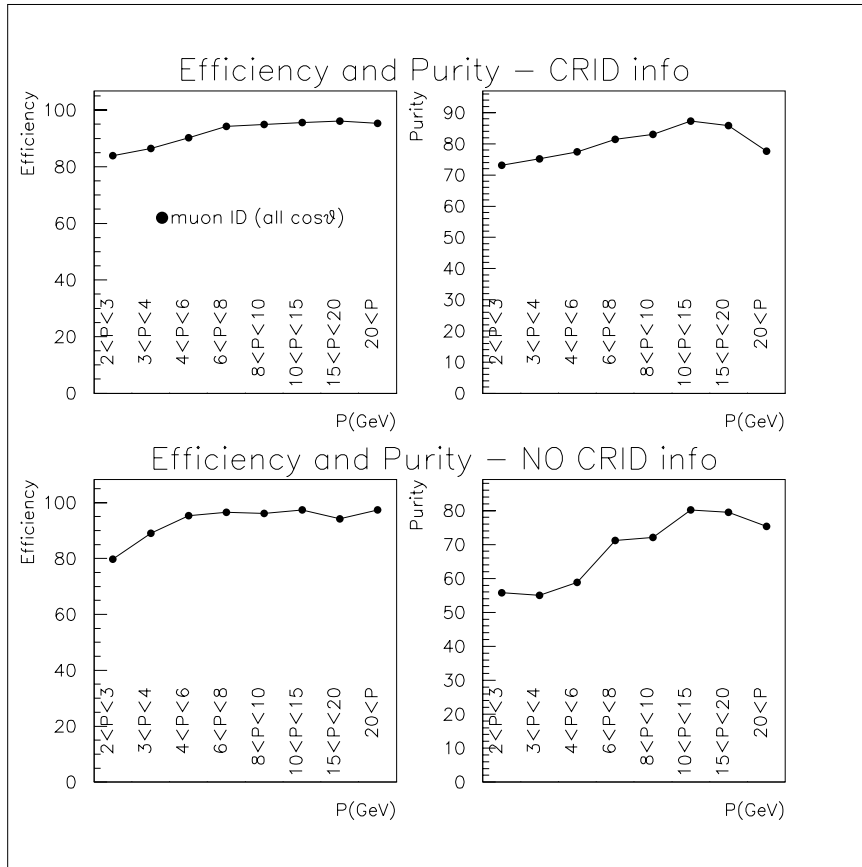


**Figure 5.13:** Comparison of efficiency and purity of the muon identification algorithm with and without CRID information.

# Chapter 6

## Measurement of $A_b$

The technique that will be described in this chapter uses identified muons from semileptonic decays of  $B$  hadrons to measure the coupling asymmetry of the underlying  $b$  quarks to the  $Z^0$  boson.

The probability of correct identification of the  $b$  quark and reconstruction of its charge and direction is called the *analyzing power*. The asymmetry signal can be diluted by the presence of muons coming from other sources in hadronic events: therefore it is of fundamental importance to be able to separate muons coming from decays of  $B$  hadrons in  $b\bar{b}$  events from those coming from direct decays of  $D$  hadrons in  $c\bar{c}$  events or from other sources.

There are two principal ways to proceed:

1. muons from a certain source can be isolated by applying cuts on characteristic tagging variables and the asymmetry can then be calculated in  $\cos\theta$  bins for this optimized

## 6.1 Signal and background

---

Source	Composition	Asymmetry
$b \rightarrow \mu^-$	31.2%	$A_b$
$b \rightarrow c \rightarrow \mu^+$	14.8%	$-A_b$
$b \rightarrow \bar{c} \rightarrow \mu^-$	2.7%	$A_b$
$c \rightarrow \mu^+$	16.9%	$A_c$
$b \rightarrow J/\psi \rightarrow \mu^\pm$	0.4%	0
$b \rightarrow \tau \rightarrow \mu^-$	1.2%	$A_b$
$\pi, K \rightarrow \mu$ and misid.	32.8%	$A_{bkg}$

**Table 6.1:** Composition of Monte Carlo identified muons from the main sources.

sample of muons.  $A_b$  is then extracted by fitting to the theoretical function and correcting for the analyzing power;

- alternatively, using the MC information of the same tagging variables, one can estimate for every muon the probabilities for all the different decay sources and then calculate the asymmetry by fitting to a likelihood function where each event contributes through a series of weights corresponding to these probabilities.

The last method is the one applied in this work, as it has proved to be solid and more statistically powerful than the first one.

## 6.1 Signal and background

In table 6.1 is shown the MC composition of identified muons from  $Z^0$  selected hadronic decays, with the main sources singled out and their respective contributions to the asymmetry. The physics sources that muons can come from are:

- direct decays of  $B$  hadrons:  $b \rightarrow \mu^-$ ;

## 6.1 Signal and background

---

2. cascade decays of  $B$  hadrons ( $b \rightarrow c \rightarrow \mu^+$ ), where the muon charge is opposite in sign to the  $b$  quark charge;
3. cascade decays of  $B$  hadrons ( $b \rightarrow \bar{c} \rightarrow \mu^-$ ), where the muon charge has the same sign as the  $b$  quark charge;
4. direct decays of  $D$  hadrons in  $c\bar{c}$  events;
5.  $\tau$  decays (following  $B$  hadron decays);
6.  $J/\psi$  decays;
7. light hadron decays ( $\pi$  and  $K$ ), *punch through* (pions and kaons that reach the WIC before decaying and can therefore be mistaken for muons), or tracks wrongly associated to WIC hits.

Their respective contributions to the asymmetry are:

- $A_b$ , for decays of the type (1) and (5) (since  $\tau$ 's have the same sign as  $b$  quarks in the chain  $b \rightarrow \tau^- \rightarrow \mu^-$ );
- $-A_b$  for decays of type (2): in this case the  $D$  hadron is produced from the  $B$  when the  $b$  quark decays into a  $W^-$  and a  $c$  quark. Since the charge of the  $c$  quark is opposite in sign to the charge of the  $b$  quark, when the  $D$  decays semileptonically it produces muons with opposite charge and therefore the asymmetry is negative;
- $A_b$  for decays of type (3): here the  $D$  hadron is produced from the  $W^-$ , for example when it decays into  $\bar{c}$  and  $s$  quarks (dominant mode). In this case the  $D$ 's then decay into muons with the same charge as the original  $b$  quark;

## 6.2 The Maximum Likelihood Method

---

- $A_c$  for decays of type (4);
- an average null asymmetry for decays of type (6), since they are always produced in  $J/\psi \rightarrow \mu^+\mu^-$  decays;
- $A_{bkg}$  (background asymmetry) for decays of type (7), which is calculated from Monte Carlo events as a function of the track total and transverse momenta.

In the determination of  $A_b$  (1) is the main source of signal and (2) and (3) only as long as it is possible to distinguish the sign of their contributions.

## 6.2 The Maximum Likelihood Method

The measurement of the  $b$  quark forward-backward asymmetry is essentially done in three steps: a) the selection of  $b\bar{b}$  events; b) the identification of the  $b/\bar{b}$  quark and the measurement of their polar angle  $\theta$ ; c) the maximum likelihood fit to the angular distribution with the theoretical function for the asymmetry.

The use of a maximum likelihood method presents some advantages over other techniques: i) all the available statistics can be used without applying any cuts; ii) there is no dependence on arbitrary parameters like bin dimensions or threshold values of the cuts.

The basic idea of this method is that the parameters we want to measure are those which maximize the probability for a certain set of events to happen. If  $p$  is the probability for a given event to occur, parametrized by unknown quantities  $a_i$  that have to be measured, a total probability  $P(a_i)$  can be defined as the product of the single probabilities for every

## 6.2 The Maximum Likelihood Method

---

event:

$$P(a_i) = \prod_{j=1}^n p_j(a_i), \quad (6.1)$$

where  $n$  represents the total number of events.  $P$  is usually called *likelihood function*. The most probable values of the parameters  $a_i$  are those which maximize this function, i.e. those which satisfy:

$$\begin{aligned} \frac{\partial P(a_i)}{\partial a_i} &= 0, \\ \frac{\partial^2 P(a_i)}{\partial a_i^2} &< 0. \end{aligned} \quad (6.2)$$

Using the logarithm of the maximum likelihood function:

$$\ln|P(a_i)| = \sum_{j=1}^n \ln|p_j(a_i)|,$$

has the advantage that shifting the parameter values by a standard deviation corresponds to reducing the maximum of  $\ln P(a_i)$  by 1/2 [94]. Solutions for the parameters are then given by:

$$\begin{aligned} \frac{\partial \ln|P(a_i)|}{\partial a_i} &= 0, \\ \frac{\partial^2 \ln|P(a_i)|}{\partial a_i^2} &< 0. \end{aligned} \quad (6.3)$$

The most appropriate function, to be used in the ideal case in which one could determine independently the primary  $b$  and  $c$  quarks directions with perfect efficiency and purity, would be, event by event:

$$p_i(A_f) = \frac{3}{8} \{ (1 - A_e P_i)(1 + \cos^2 \theta_i) + 2(A_e - P_i)A_f \cos \theta_i \},$$

which represents the normalized differential cross-section, where  $f = b$  or  $c$ ,  $P_i$  is the electron beam polarization, and  $\theta_i$  is the polar angle for the  $i^{th}$  event. Correction factors

## 6.2 The Maximum Likelihood Method

---

which account for the efficiency of the quark direction measurement as a function of  $\cos \theta$  are reduced to constants once we take the logarithm, and therefore disappear in the partial derivative.

A first complication to this picture comes from the fact that the quark direction, approximated by the direction of the jet closest to the muon track, does not correspond to the primary quark but only to the quark after gluon emission. QCD corrections must therefore be added to the probability function, which then becomes:

$$p_i(A_f) = \frac{3}{8} \{ (1 - A_e P_i)(1 + \cos^2 \theta_i) + 2(A_e - P_i)(1 + \Delta_{QCD}^b(\cos \theta_i)) A_f \cos \theta_i \},$$

where  $\Delta_{QCD}^b$  is a  $\cos \theta$  dependent factor; the  $O(\alpha_s)$  calculation for massive final state quarks by Stav and Olsen [24] was used, which is as large as 0.05(0.06) for  $b(c)$  quarks at  $\cos \theta = 0$ . Since every event in the data can only be assigned probabilities for coming from a certain source, which is in turn associated to a certain asymmetry, it is natural to combine all these possible contributions into the same function:

$$\begin{aligned} P(p, p_t, m, l/d, P_e, z; A_b, A_c) \propto & \{ (1 + z^2)(1 - A_e P_e) - 2Q(A_e - P_e) & (6.4) \\ & [(f_b(1 - 2\chi_i) - f_{bc}(1 - 2\chi_i) + f_{b\bar{c}}(1 - 2\chi_i)) \\ & (1 - \Delta_{QCD}^b(z)) A_b \\ & + f_c(1 - \Delta_{QCD}^c(z)) A_c + f_{bkg} A_{bkg}] z \} \end{aligned}$$

where  $z = \cos \theta_{jet}$ . The lepton source fractions  $f_b, f_{bc}, f_{b\bar{c}}, f_c, f_{bkg}$ , corresponding to the decays  $b \rightarrow \mu, b \rightarrow c \rightarrow \mu, b \rightarrow \bar{c} \rightarrow \mu, c \rightarrow \mu$  and background respectively, will be derived in the next section as a function of characteristic variables. A correction factor  $(1 - 2\chi_i)$  is applied to take into account  $B$  mixing effects that could dilute the signal through a

### 6.3 Estimate of the muon decay sources

---

wrong charge association. The asymmetry of the background  $A_{bkg}$  is calculated from the simulation.

### 6.3 Estimate of the muon decay sources

Kinematic and vertexing variables are used to evaluate from the simulation the probability that a muon comes from each of the various decay sources.

Because of the large mass of the  $b$  quark,  $B$  hadrons are the heaviest particles produced in  $Z^0$  decays. Therefore, muons coming from their semileptonic decays have a large momentum in the hadron rest frame, hence a large transverse momentum with respect to the  $B$  direction in the laboratory frame. Furthermore, the large fraction of the energy taken by the  $b$  quark is transferred to the  $B$  hadron providing for a large boost, and for a large total momentum of the leptons decaying from it.  $D$  hadrons produced from a  $B$  decay have a smaller energy and consequently the muons at the end of the cascade chain have a softer momentum spectrum. As for  $c\bar{c}$  events, since the  $c$  quark is still relatively heavy, muons from  $D$  direct decays tend to have a fairly large total momentum; yet, due to the lighter mass, the lepton transverse momentum distribution tends to be shifted towards lower values. All the other charged tracks in hadronic events, mainly pions and kaons, as well as muons produced in their decays, generally have small values of their momenta. Finally, tracks that are misidentified as muons usually result from a mismatch of WIC hits with CDC tracks, and therefore their momentum distributions are also quite soft.

Figs. 6.1 and 6.2 show the total and transverse momentum distributions in data and Monte Carlo (with the contributions from the major sources singled out). There is

### 6.3 Estimate of the muon decay sources

---

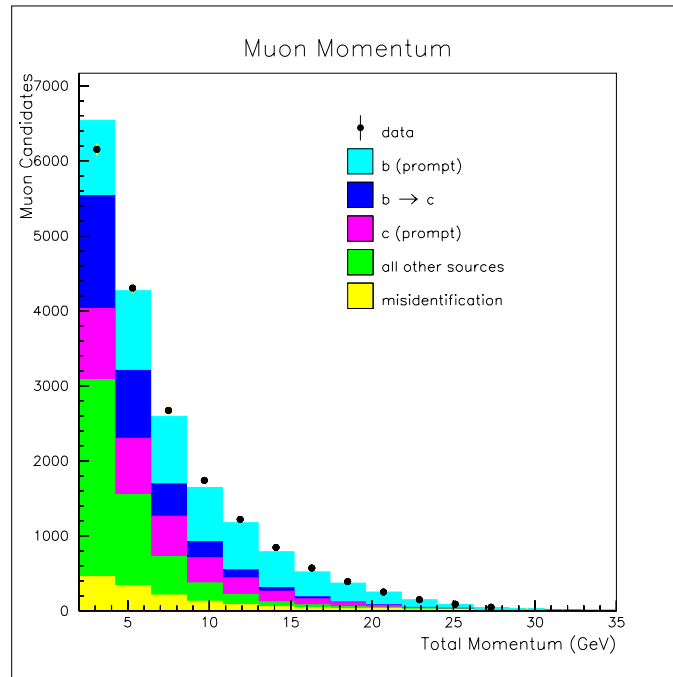


**Figure 6.1:** Total momentum distribution of identified muons in 1997-98 data (dots) and Monte Carlo (histogram).

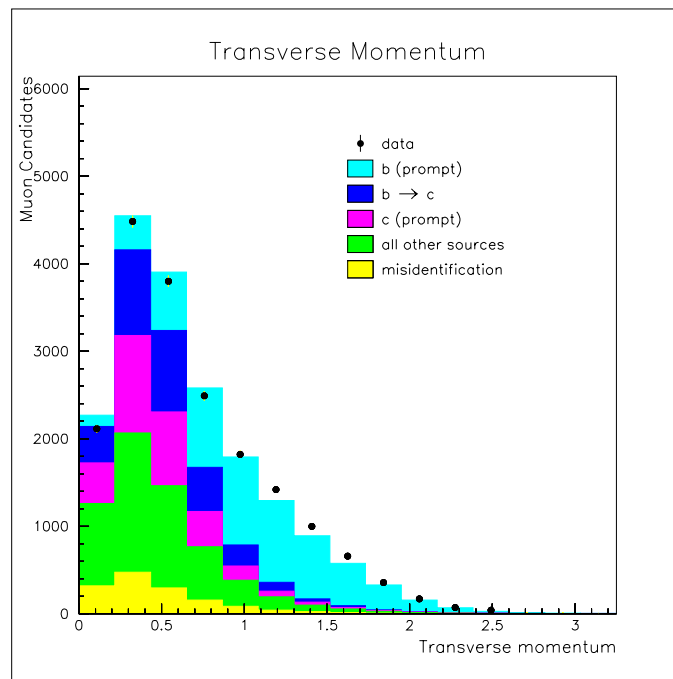


**Figure 6.2:** Transverse momentum distribution of identified muons in 1997-98 data (dots) and Monte Carlo (histogram).

### 6.3 Estimate of the muon decay sources

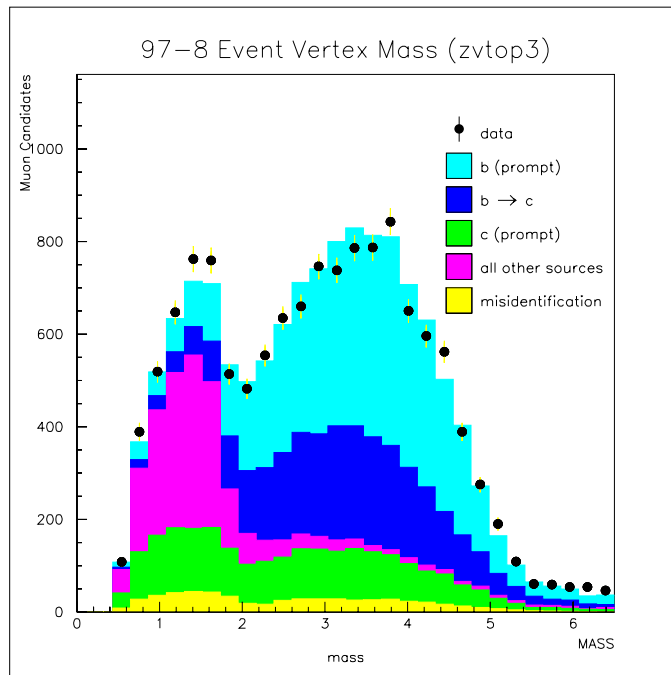


**Figure 6.3:** Event mass distribution for muons in 1997-98 data (dots) and Monte Carlo (histogram). The event mass is defined as the largest of the vertex masses found in the two hemispheres.

good agreement between them and it is possible to observe how the tails at large momenta are mostly populated by muons coming from  $b$  quark direct decays.

Vertexing information is reconstructed by dividing an event in two hemispheres and by applying the topological vertexing algorithm in each of them to find secondary decay vertices. If a vertex is reconstructed in both hemispheres, the mass of the event is defined as the largest of the masses of the two vertices; otherwise the mass of the only vertex found is taken. The efficiency for reconstructing a  $B$  vertex in the same hemisphere as the muon for  $Z^0 \rightarrow b\bar{b}$  events is  $\sim 50\%$  in 1993-95 and  $\sim 66\%$  in 1996-98; the efficiency per event (considering both hemispheres) is 74% in 1993-95 and 88% in 1996-98. Shown in fig. 6.3 is the event mass distribution in data and Monte Carlo for all the different decay

### 6.3 Estimate of the muon decay sources

---

sources. One can easily notice the sort of “natural cut” around the value of the  $D$  meson mass (1.8-2 GeV/c<sup>2</sup>), with most of the  $c\bar{c}$  contribution isolated below this threshold.

The weights in Eq. 6.4, corresponding to the decay source probabilities for any given event, are then calculated from the Monte Carlo as a function of the variables described above:  $P$ ,  $P_t$  and  $M$  (event mass). For every muon in the data, simulated events are selected with similar values of these 3 quantities, using a *nearest neighbours technique* in a 3-dimensional phase space. Three separate planes are defined, corresponding to 3 different ranges of the event mass: the charm region ( between 0.55 and 2 GeV/c<sup>2</sup>), the bottom region (above 2 GeV/c<sup>2</sup>) and finally the ensemble of all those events for which it has been impossible to reconstruct a decay vertex. The quantities  $\sqrt{P_t}$  and  $0.5 \cdot \ln P$  have been chosen as  $x$  and  $y$  coordinates of these planes: the reason for this choice relies on the fact that the distributions of events in these variables are much more uniform (see fig. 6.4) and furthermore the scales for these quantities are comparable (so that the weights for  $P$  and  $P_t$  are approximately the same). The weights are then calculated from samples of Monte Carlo events which, in the plane corresponding to the event mass, satisfy the relation:

$$\delta r_i^2 = \left[ 0.5 \cdot \ln P_i^{MC} - (0.5 \cdot \ln P_i^{DT} \pm \delta r_0) \right]^2 + \left[ \sqrt{P_{t_i}^{MC}} - (\sqrt{P_{t_i}^{DT}} \pm \delta r_0) \right]^2 < \delta r_0^2. \quad (6.5)$$

Four of these samples are selected, corresponding to the configuration shown in fig. 6.5: four circles with radius  $\delta r_0$  and centres which are shifted from the data point  $(\sqrt{P_t^{DT}}, 0.5 \ln P^{DT})$  by the quantity  $\pm \delta r_0$  along both axes. We then calculate the barycentres of these circles by weighting the positions of the events within them with their event weight in the Monte Carlo, and we associate to these points the average fractions for the various sources in the sample (fractions of events of each source). The weights at the data point are then

6.3 Estimate of the muon decay sources

---

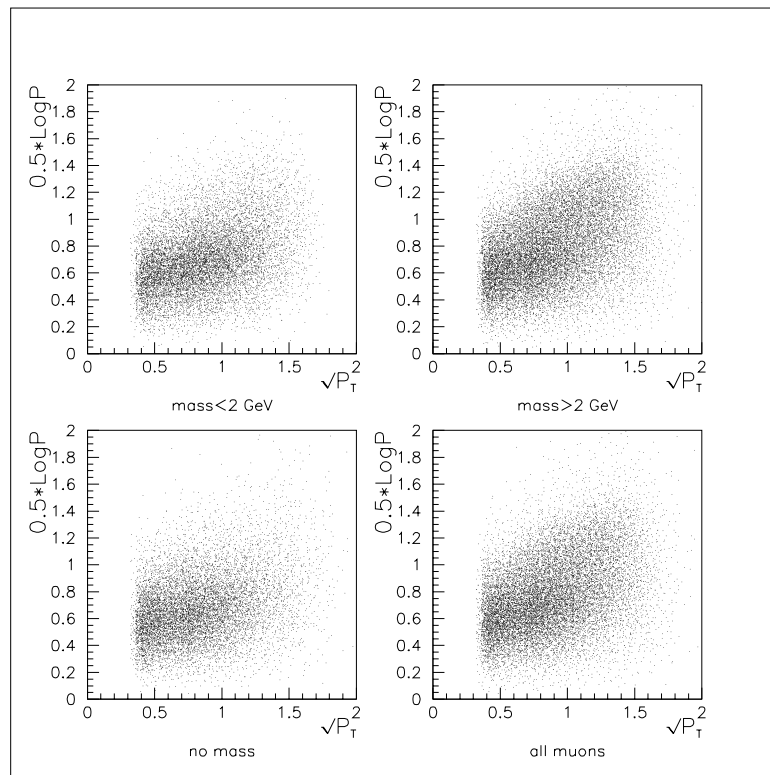


**Figure 6.4:** Distribution of  $0.5 \ln P$  and  $\sqrt{P_t}$  for muons in the 1996-98 data.

### 6.3 Estimate of the muon decay sources

---

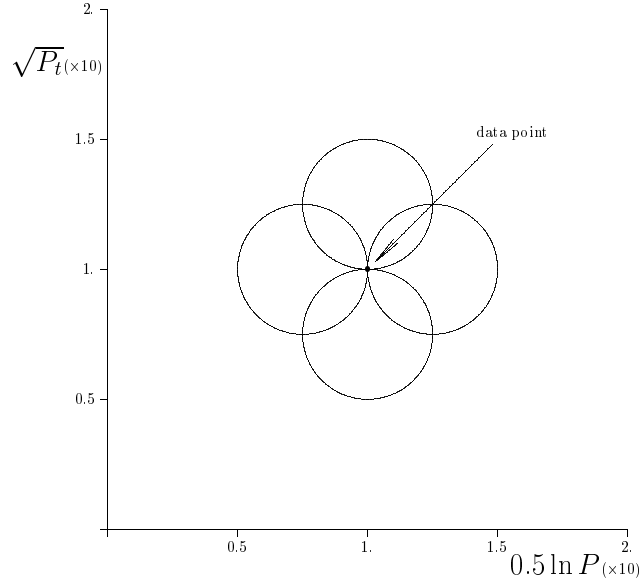


**Figure 6.5:** Illustration of the method applied in the  $\sqrt{P_t} vs 1/2 \ln P$  planes to select MC events to calculate decay source probabilities for the muon in the data.

derived via a linear interpolation between the 2+2 baryocenters (2 on the  $x$  axis, 2 on the  $y$  axis) and renormalized to unity, thus approximating the behaviour of the fractions as continuous functions in the phase space. The value of the search area  $\pi \delta r_0^2$  has been optimized with respect to the statistics available in the Monte Carlo (where, along with the general all-flavours type, we have also included additional samples of  $b\bar{b}$  and  $c\bar{c}$  events, in order to minimize systematic errors due to MC statistical fluctuations). The values used for the quantity  $\delta r_0^2$  are respectively 0.003 for 1993-95 data, 0.0075 for 1996, and 0.002 for 1997-98 data. These values have been chosen after a series of studies using Monte Carlo as data cross-checks to reproduce the Standard Model predictions and also after checking that results from the data were stable over a sufficiently large interval of values containing the preferred one (see fig. 6.6). In choosing the optimal area one has to be aware of two opposite situations: if the radius is too small then the statistics in the sample is too poor

## 6.3 Estimate of the muon decay sources

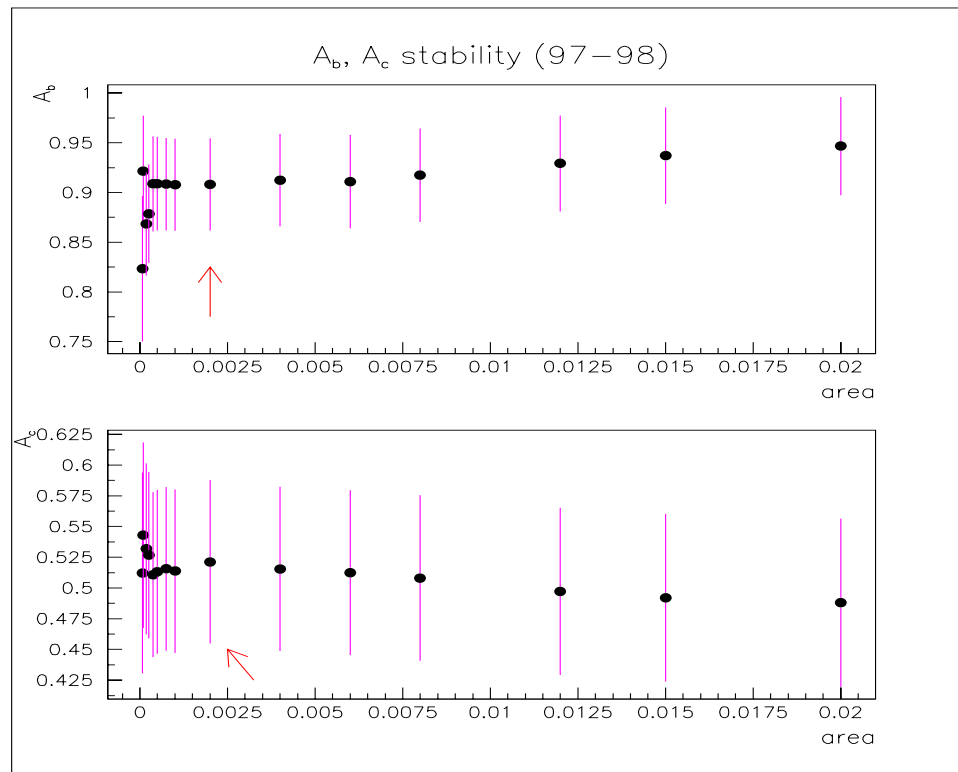


**Figure 6.6:** Stability of the  $A_b, A_c$  fit results as a function of the MC sampling area from which decay sources probabilities are derived.

### 6.3 Estimate of the muon decay sources

---

to provide any reliable information; on the other hand, if the area is too large then the events selected (especially those on the periphery) are not particularly representative of the data point. In both cases the signal for the asymmetry would be washed out.

#### 6.3.1 L/D information

In a second step, and for those events only with a reconstructed secondary vertex in the muon hemisphere ( $\sim 57\%$  of the total), the source probabilities obtained with the nearest neighbours technique just described in a 3-D phase space are re-weighted with a set of fractions derived from a fourth variable.

In this analysis in fact, it is not only important to be able to separate bottom from charm events (for which the information provided by the secondary vertex mass is crucial), but also to distinguish the various sources of  $b$  decays. The weight of bottom events is in fact approximately given by the difference between the probabilities of a direct and a cascade (wrong sign) decay. Since these have opposite signs and are comparable in magnitude, if they are not accurately separated, the resulting weight will be particularly low, thus diluting the signal for  $A_b$ .

The L/D variable, as defined in fig. 5.3, proves to be particularly useful for this purpose. This quantity can in fact be used to somehow “position” the muon track along the decay chain: in cases in which only one secondary vertex is reconstructed, values of  $L/D < 1$  (muon upstream with respect to the secondary vertex) are more likely to characterize direct decays of the  $B$  into the lepton, whereas values  $> 1$  (muon downstream with respect to the vertex) are more likely to be a signature of cascade decays. As is evident in fig. 6.7,

### 6.3 Estimate of the muon decay sources

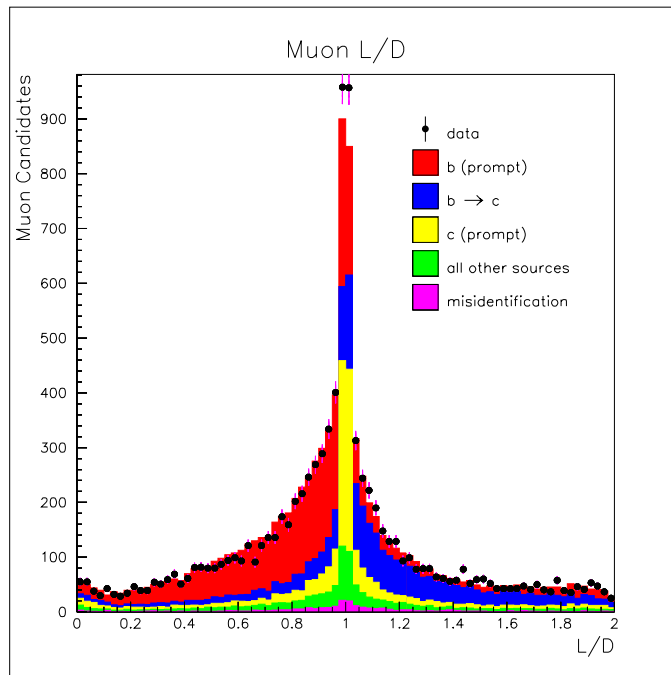
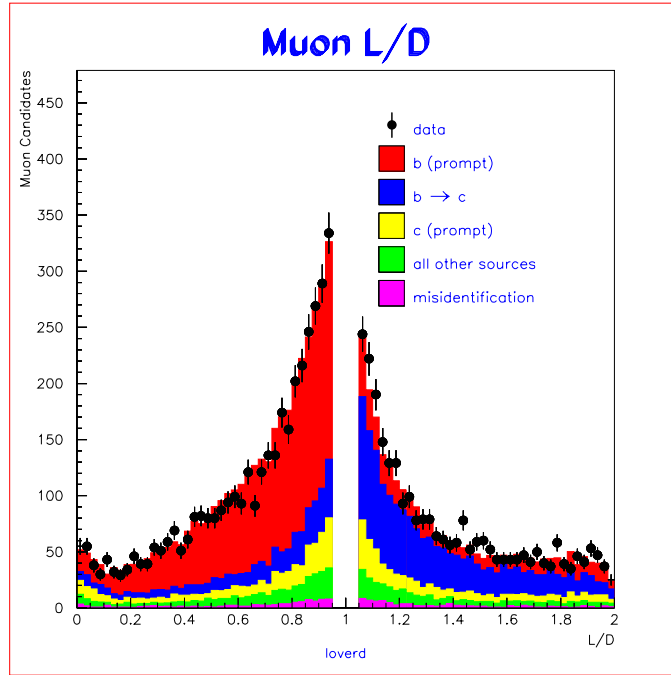


Figure 6.7: L/D distribution for muons in 1997-98 data (dots) and Monte Carlo (histogram).

all the discriminant information is contained in the tails of the distribution, whereas little analyzing power is present in the central peak. Shown in fig. 6.8 is the same distribution with a cut applied requiring:  $|(L/D - 1)| > 0.05$ .

For 1993 to 1996 data, L/D is defined for all those events with at least one reconstructed vertex and with the muon track belonging or attachable to it: a new vertex is fitted after excluding the muon track, and L/D is calculated with respect to this re-fitted vertex. The efficiency for reconstructing L/D in  $Z^0 \rightarrow b\bar{b}$  events is approximately 23% and 31% for VXD2 and VXD3 respectively (tails only). For 1997-98 data, thanks to the new vertexing algorithm (“*ghost algorithm*”), which allows the possibility of reconstructing multiple decay vertices, we adopt two separate definitions: i) if only one secondary vertex is found, then

### 6.3 Estimate of the muon decay sources



**Figure 6.8:** Tails of the L/D distribution for 1997-98 data (dots) and Monte Carlo (histogram).

we follow the usual procedure, otherwise ii) L/D is redefined as:

$$L/(D_2 + D_3),$$

where  $D_2$ ,  $D_3$  are the flight distances from the IP of the secondary and tertiary vertices respectively. Without this redefinition for the “ghost” track algorithm, the muon L/D distribution would be just peaked at 1 for all events where more than one secondary vertex is reconstructed, and consequently it would not provide any useful information. The efficiency for reconstructing L/D in this case is 61% (in the tails for  $Z^0 \rightarrow b\bar{b}$  events). The sets of fractions that are used to re-weight the muon source probabilities derived in the  $(P, P_t, mass)$  space are extracted from the L/D distribution after dividing it into several intervals. In each of these intervals we calculate the probability for an event of any given

## 6.4 Maximum likelihood fit

---

source to have a value of  $L/D$  included in that interval. These probabilities, renormalized to unity, are then used to rescale the fractions obtained in the 3-D phase space. In order to take into account correlations between  $L/D$  and all the other variables, different matrices of  $L/D$  efficiencies are calculated in different  $(P, P_t, M)$  regions. There are two main reasons to explain why this particular solution was adopted instead of just using  $L/D$  as an additional coordinate in a 4-dimensional phase space: 1) because useful information to separate the decay channels is only provided in the tails of the distribution and 2) because adding another dimension would have dispersed too much the MC population in a 4-D phase space (the statistics available was insufficient).

## 6.4 Maximum likelihood fit

Once the weights corresponding to the muon decay source probabilities have been calculated, there are still a few effects that need to be taken into account before proceeding with the maximum likelihood fit to extract  $A_b$  (and  $A_c$ ).

### 6.4.1 $B$ mixing

$B$  mixing is the tendency of neutral  $B$  mesons to transform into their own anti-particles: this can have the effect of changing a  $b$  quark into a  $\bar{b}$  (or vice-versa) before it decays (for example semileptonically), with the consequence that the charge attributed to the primary quark (as deduced by the charge of the decay products, in this case muons) can therefore be wrong. The asymmetry signal would then be diluted by these events for wrong charge association.

#### 6.4 Maximum likelihood fit

---

Let  $\chi$  be the mixing probability for a  $B$  hadron to decay after having transformed into its own antiparticle. If the mixing probability is large (as in the case of a  $B_s$ ), the meson will transform more than once into its antiparticle before decaying, and therefore  $\chi = 1/2$ . If on the other hand the mixing probability is small (as for a  $B_d$ ), that means that the meson often decays before mixing, and therefore  $\chi$  is small.

If  $\bar{\chi}$  is the average value of  $\chi$  for all  $B$  hadrons, including those that have not mixed, the  $b$  quark asymmetry has to be corrected according to:

$$\tilde{A}_{FB}^b = \frac{\tilde{A}_{FB}^b(\text{observed})}{(1 - 2\bar{\chi})}, \quad (6.6)$$

where the factor of 2 is due to the fact that if the sign of the charge of the  $b$  quark is wrong, then the contribution to the asymmetry has opposite sign. The current world measurement for  $\bar{\chi}$  is given by the average over all LEP experiments for  $b$  direct decays [15]:

$$\bar{\chi} = 0.1186 \pm 0.0043.$$

This correction, however, is only an approximate way to account for mixing effects. There is in fact a dependence of the mixing probability on the decay type, so that, for example, mixing effects are expected to differ for primary or secondary lepton components [95]. Assuming the charged and neutral  $B$  meson lifetimes and production rates to be approximately identical, primary leptons satisfy:

$$BR(B^- \rightarrow l^- X) = BR(\bar{B}_d \rightarrow l^- X),$$

whereas for secondary leptons, since they mainly originate via the decay chain  $\bar{B} \rightarrow D \rightarrow l^+$ , we expect that:

$$c \equiv \frac{BR(\bar{B}_d \rightarrow l^+ X)}{BR(B^- \rightarrow l^+ X)} > 1, \quad (6.7)$$

## 6.4 Maximum likelihood fit

---

because

$$BR(D^+ \rightarrow l^+ X)/BR(D^0 \rightarrow l^+ X) \approx \tau(D^+)/\tau(D^0) = 2.55.$$

In this analysis, instead of using 3 different average values of  $\bar{\chi}$  for the three types of  $B$  decay ( $b \rightarrow \mu$ ,  $b \rightarrow c \rightarrow \mu$  and  $b \rightarrow \bar{c} \rightarrow \mu$ ), we use a mixing probability  $\chi_i$  that is calculated event by event based on its kinematic and lifetime information. The  $b\bar{b}$  events selected in the four samples of the 3-D MC phase space used to derive the event decay source probabilities (those that best approximate the event behaviour in  $P$ ,  $P_t$  and  $M$ ) are divided into 3 subsamples corresponding to 3 different L/D ranges (L/D<1, L/D>1 and events with no L/D reconstructed).  $\chi_i$  is then obtained by averaging over the true mixing information of the Monte Carlo  $b\bar{b}$  events that fall in the L/D bin corresponding to the data point. With this procedure there is no more need to apply rescalings to the average  $\bar{\chi}$  (calculated for  $b$  direct decays) to account for different mixing behaviours of the cascade components, and the dependence on the decay source is automatically accounted for (see fig. 6.9).

### 6.4.2 $O(\alpha_s)$ QCD corrections

The factor  $\Delta_{QCD}^f$  ( $f = b, c$ ), which appears in the likelihood function 6.4, takes into account first order QCD corrections as a function of the polar angle as calculated by Stav and Olsen in the polarized massive case [24]. Shown in fig. 6.10 are the absolute and relative contributions of the  $O(\alpha_s)$  QCD corrections to the polarized forward-backward asymmetry of the  $b$  quark as a function of the polar angle  $\theta$  for different values of the quark mass.

## 6.4 Maximum likelihood fit

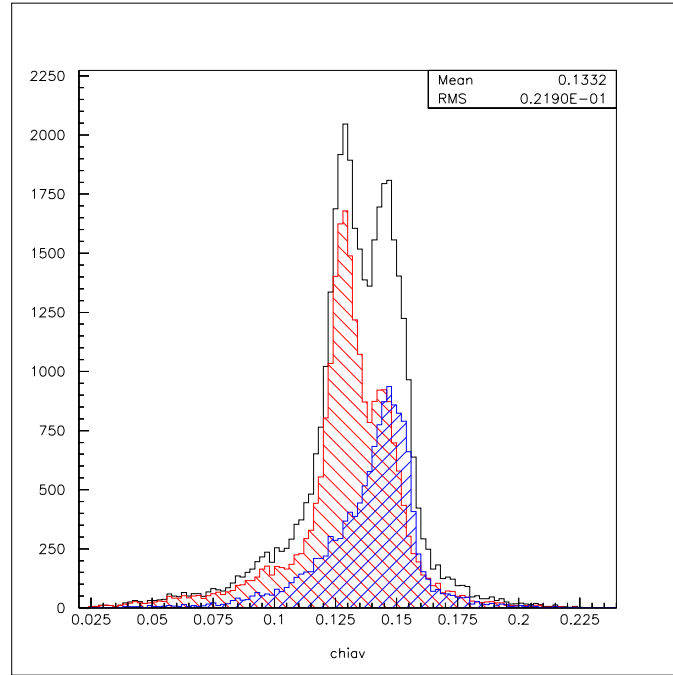


**Figure 6.9:** Distribution of the mixing probability  $\chi_i$  for  $b\bar{b}$  events: highlighted in red is the spectrum of  $b$  direct decays and in blue that for  $b$  cascade decays.

Yet even with these corrections, the fit does not yield the pure electroweak value of  $A_b$ . Firstly, there are contributions from higher orders in gluon radiation. Secondly, there are analysis procedures that reduce the effect of QCD radiation by suppressing events with hard gluon radiation, and therefore the QCD corrections must themselves be corrected to account for these mitigating effects. Biases can be both of physical nature and related to the detector efficiency and the analysis procedure. The event selection, for example, tends to favour  $q\bar{q}$  events over  $q\bar{q}g$  ones, since muons with high momentum are more likely to be produced in  $q\bar{q}$  events, where the quark energy is not diluted by gluon emission; furthermore the identified muons tend to select the highest energy quark, whose direction is less affected by the gluon emission in  $q\bar{q}g$  events. For the same reason, biases can also be introduced by the likelihood weights, which are momentum dependent and tend to

## 6.4 Maximum likelihood fit

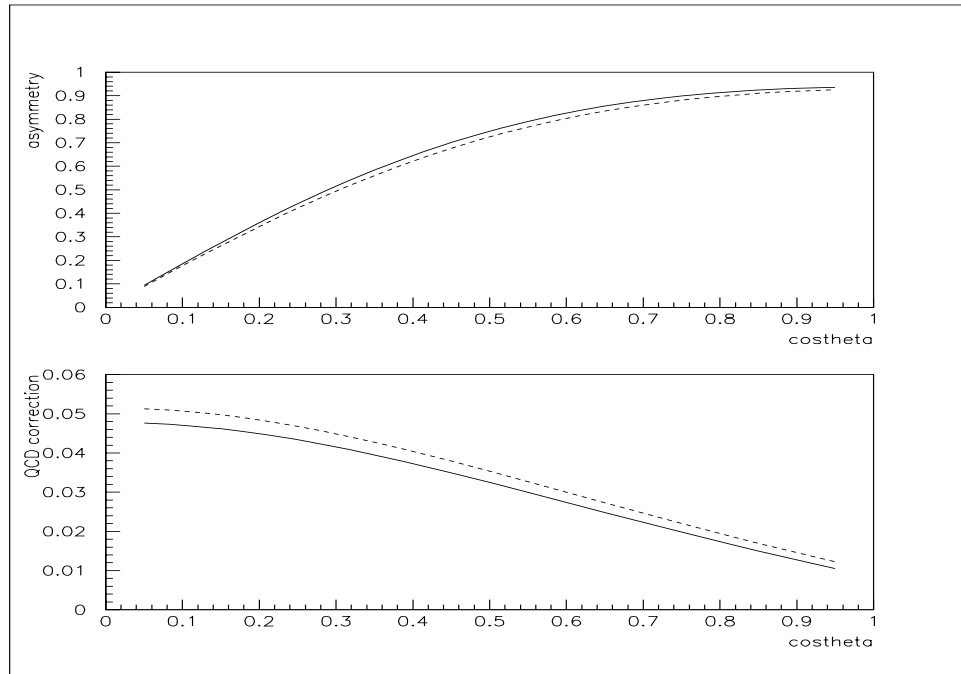


**Figure 6.10:** Contributions of the first order QCD corrections to the polarized forward-backward asymmetry of the  $b$  quark as a function of the cosine of the polar angle  $\theta$ . In the figure at the top is shown the asymmetry with (dashed line) and without (solid line) QCD corrections. In the figure at the bottom is shown the relative QCD correction  $\Delta_{QCD}^b$  for  $m_b=4.5 \text{ GeV}/c^2$  (solid line) and  $m_b=0$  (dashed line).

## 6.4 Maximum likelihood fit

---

Conditions of fit	$A_b$ from fit	Change from previous fit
$O(\alpha_s)$ ; no cuts or reweighting	$0.8947 \pm 0.0010$	
$P > 2$ GeV	$0.9003 \pm 0.0011$	+0.0056
Likelihood weights	$0.9014 \pm 0.0015$	+0.0011
Muon ID eff.	$0.9024 \pm 0.0018$	+0.0010
Quark selection	$0.9057 \pm 0.0018$	+0.0033
Hadronization	$0.9049 \pm 0.0018$	-0.0008
Decay and jet modeling	$0.9083 \pm 0.0018$	+0.0034
Input electroweak $A_b$	0.9350	

**Table 6.2:**  $A_b$  study on the analysis corrections to the first order QCD corrections.

favour events at high momenta. Other effects which are considered are those related to hadronization and  $B$  and  $D$  models, to the extent that they influence the reconstruction of the quark direction.

To estimate the impact of these effects on the QCD correction, a sample of  $\sim 2$  million generator level  $Z \rightarrow b\bar{b}(c\bar{c})$  events have been produced using JETSET 7.4 [66] and including effects of QCD radiation via the use of a first-order matrix element [96]. The polarized forward-backward asymmetry of these events, after various levels of simulation of the event generation process and analysis procedures, was fitted to the form  $2A_{b(c)} \cos \theta / (1 + \cos^2 \theta)$  in the region  $|\cos \theta| < 0.7$ . Table 6.2 presents the results of one of these studies for the  $A_b$  analysis, showing the cumulative diluting effects as the various analysis steps are switched on. Only events with muons from  $b$  decay are included in the asymmetry fit. In the first four lines we consider the direction of the quark before hadronization. For line 1, the fit is to all events. In line 2 we consider only those events containing a muon with momentum greater than 2 GeV/c. In line 3 events are further weighted according to their approximate weight in the maximum likelihood analysis. In line 4 the events are additionally weighted

#### 6.4 Maximum likelihood fit

---

with the muon identification efficiency (as a function of the momenta), as determined by the full simulation Monte Carlo. At line 5, still maintaining all the previous steps, the asymmetry is now calculated with respect to the final state quark. In line 6 we introduce the effects of hadronization by considering the  $B$  meson direction and finally at line 7 we include effects of the semileptonic decay process and the association of the muon to the nearest jet by considering the jet axis direction. The global effect of all these corrections is given by the formula:

$$\Delta_{QCD}(z) = \left( \frac{A^0(z) - A_{MC}^{1,anal}(z)}{A^0(z) - A_{MC}^1(z)} \right) \left( \frac{A^0(z) - A_{SO}^1(z)}{A^0(z)} \right) \equiv f_{QCD}(z) \cdot \Delta_{QCD,SO}(z), \quad (6.8)$$

where  $z = \cos \theta$ , and  $A^0$ ,  $A^1$  refer to the pure electroweak and first-order corrected asymmetries. The subscripts “SO” and “MC” refer to the Stav-Olsen calculation and Monte Carlo generator-level asymmetries respectively. The superscript “anal” refers to the MC asymmetry after all steps of the analysis simulation have been applied.  $f_{QCD}(\cos \theta)$  is the amount of correction to the Stav-Olsen calculation as derived from this study. A similar procedure has been applied to derive the correction in the case of  $c$  quarks.

Since we have made use of functions generating random numbers in the simulation of the analysis steps, the calculation of  $f_{QCD}^b(f_{QCD}^c)$  has been repeated several times and the results have been averaged. Mean values of  $f_{QCD}^b = 0.75 \pm 0.10$  and  $f_{QCD}^c = 0.70 \pm 0.20$  were found over the region  $|\cos \theta| < 0.7$ , corresponding to an increase of  $\sim 1.5\%$  (1.4%) in  $A_b$  ( $A_c$ ), or in other words a reduction of the size of the first order correction as given by the Stav and Olsen calculation. In practice,  $|\cos \theta|$ -dependent values for  $f_{QCD}$  have been used in the likelihood fit.

## 6.4 Maximum likelihood fit

---

### 6.4.3 Background asymmetry

In the measurement of the polarized forward-backward asymmetry it is of fundamental importance to correctly identify the backgrounds and estimate their effects on the measurement. The most important of these effects is the forward-backward asymmetry of the background events, which is quite complicated to estimate for light hadron events especially, given the different sources muons can derive from, and can be expected to depend on the muon total and transverse momenta.

One could in principle try to approximate the behaviour of muons from light hadron decays or misidentified muons with that of all charged non-leptonic tracks in the data with momentum greater than 2 GeV/c. This assumption is however not so accurate, and there is a significant difference in the angular distribution in  $|\cos\theta|$  of these event samples (see fig. 6.11). Given the difficulty of distinguishing the various sources of background in the data, their contribution to the asymmetry has been estimated in this analysis using true background events in the simulation, separated into two different categories: 1) misidentified muons and 2) muons from light hadron decays or misassociated tracks. For each of these samples, the asymmetry has been calculated as a function of the polar angle  $\cos\theta$ , using a fit to:

$$\tilde{A}_{FB}(\cos\theta) = 2P_e A_{bkg} \frac{|\cos\theta|}{1+\cos^2\theta},$$

in different regions of transverse momentum and logarithm of total momentum. The fit results for each of these sectors are shown in fig. 6.12. A polynomial fit is applied in every transverse momentum bin to extract the asymmetry as a function of the logarithm

## 6.4 Maximum likelihood fit

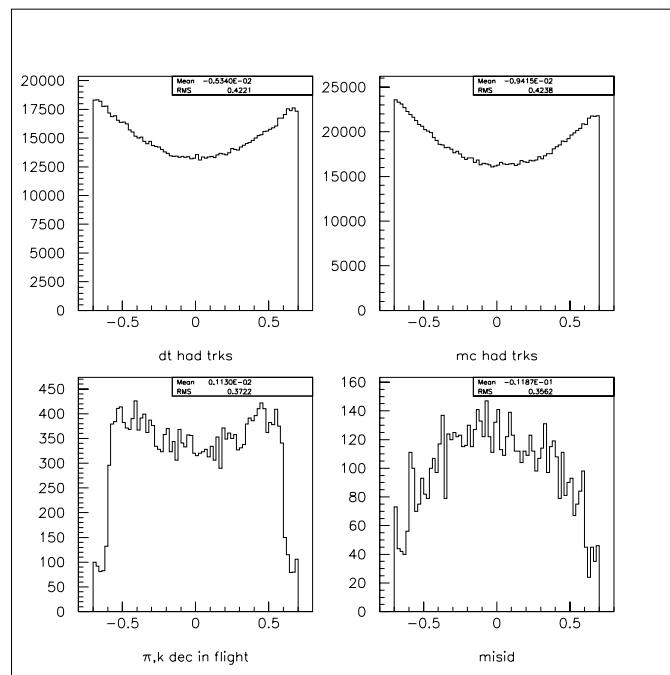


**Figure 6.11:** Angular distribution of: non-leptonic charged tracks in the data (top left) and Monte Carlo (top right), Monte Carlo muons from light hadron decays (bottom left) and misidentified muons (bottom right).

## 6.4 Maximum likelihood fit

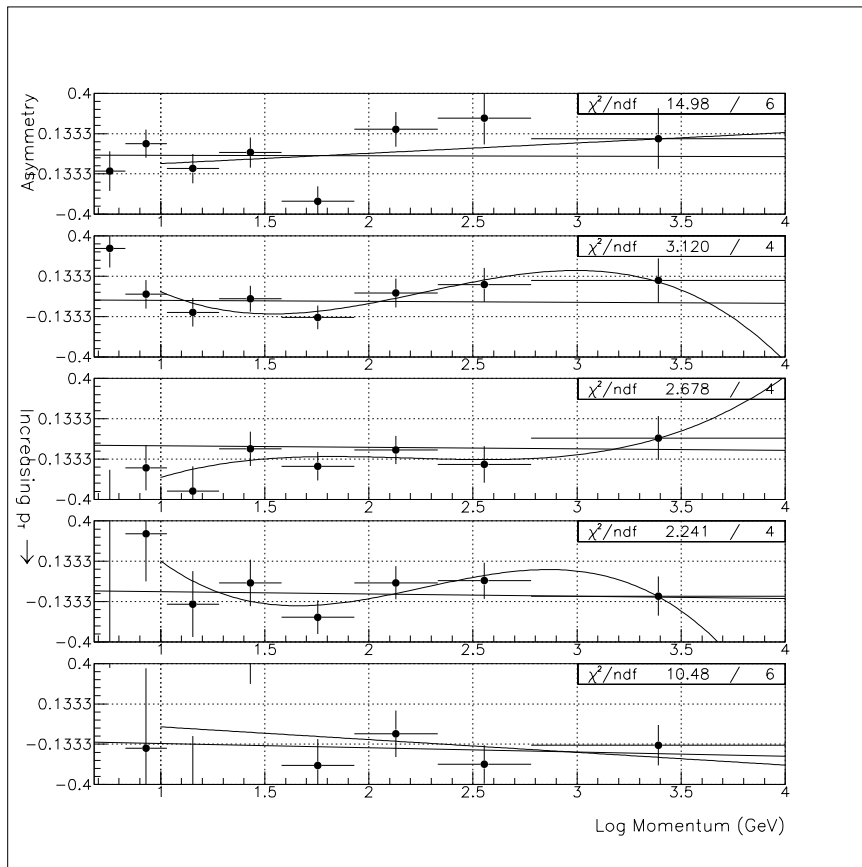


**Figure 6.12:** Results of the asymmetry fit for MC muons from light hadron decays in every transverse momentum bin as a function of the logarithm of the total momentum.

## 6.5 Crosscheck: MC as data study

---

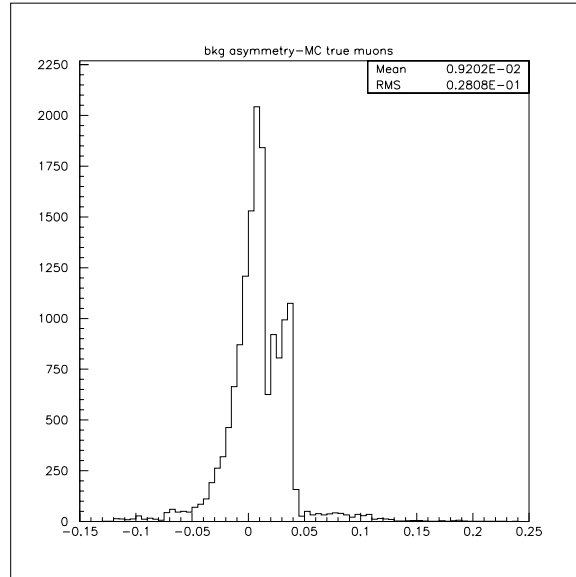


**Figure 6.13:** Distribution of the fitted values of the asymmetry for 1997-98 Monte Carlo background events.

of the total momentum. A distribution of the asymmetry for 1997-98 Monte Carlo events identified as background is shown in fig. 6.13. Different fits have been used for the 1993-5, 1996 and 1997-98 datasets.

Finally, to account for the uncertainty on how well the background distributions in the simulation reproduce the data, the light hadron asymmetry, as extracted from the fit to the Monte Carlo events, has been rescaled by the data to Monte Carlo ratio of the asymmetry in a sample of charged non-leptonic tracks passing a momentum cut at 2 GeV/c.

## 6.5 Crosscheck: MC as data study

A crosscheck has been done using events in the simulation as data, and considering the Monte Carlo true origin of the event instead of the set of weights calculated with the nearest neighbours technique in the 3-D phase space. This gives:

## 6.5 Crosscheck: MC as data study

---

$$A_b = 0.926 \pm 0.018_{stat} \pm 0.006_{syst}$$

$$A_c = 0.647 \pm 0.023_{stat} \pm 0.006_{syst}$$

for 1993-1995,

$$A_b = 0.956 \pm 0.023_{stat} \pm 0.006_{syst}$$

$$A_c = 0.687 \pm 0.031_{stat} \pm 0.006_{syst}$$

for 1996, and

$$A_b = 0.939 \pm 0.009_{stat} \pm 0.006_{syst}$$

$$A_c = 0.648 \pm 0.013_{stat} \pm 0.006_{syst}$$

for 1997-1998 <sup>1</sup>. Input values in the fit were the Standard Model predictions for  $A_b$  and  $A_c$  (0.935 and 0.667 respectively) and the SLD measurement of  $A_e$  (0.1514). Only the uncertainties from  $O(\alpha_s^2)$  QCD corrections contribute to the systematic error.

Combining these results together, one obtains for the whole 1993-1998 data sample:

$$A_b = 0.939 \pm 0.008_{stat} \pm 0.006_{syst}$$

$$A_c = 0.653 \pm 0.011_{stat} \pm 0.006_{syst} .$$

As a further check, we have repeated the Monte Carlo as data analysis, but this time considering for each muon the set of decay source probabilities calculated as a function of  $P, P_t$ , mass and L/D. The results obtained in this case are:

$$A_b = 0.920 \pm 0.034_{stat} \pm 0.010_{syst}$$

$$A_c = 0.623 \pm 0.046_{stat} \pm 0.040_{syst}$$

---

<sup>1</sup>Data from different running periods have been analyzed separately given the differences in the apparatus (especially the upgrade in the vertex detector in 1996) and in some reconstruction algorithms, which affect the event selection efficiency and the analyzing power.

## 6.6 Flavour tag calibration

---

for 1993-1995,

$$A_b = 1.001 \pm 0.042_{stat} \pm 0.026_{syst}$$

$$A_c = 0.649 \pm 0.063_{stat} \pm 0.037_{syst}$$

for 1996, and

$$A_b = 0.953 \pm 0.016_{stat} \pm 0.011_{syst}$$

$$A_c = 0.635 \pm 0.024_{stat} \pm 0.030_{syst}$$

for 1997-1998.

The combined 1993-1998 result is:

$$A_b = 0.951 \pm 0.014_{stat} \pm 0.008_{syst}$$

$$A_c = 0.634 \pm 0.021_{stat} \pm 0.021_{syst}.$$

## 6.6 Flavour tag calibration

The Monte Carlo flavour composition has been corrected according to the data after a study of tagging efficiencies in three separate regions: one for events with  $M > 2$  GeV/c<sup>2</sup> (bottom), one for events with  $M$  between 0.55 and 2 GeV/c<sup>2</sup> (charm), and one for all events with  $M < 0.55$  GeV/c<sup>2</sup> or no mass reconstructed. The efficiency for a correct  $b$  tag in the high mass region is given by:

$$\epsilon_b = \epsilon_b^0 + \epsilon_b^\mu - \epsilon_b^d, \tag{6.9}$$

where  $\epsilon_b^0$  is the efficiency for a generic hadronic event (in the hemisphere not containing the muon track) as derived from the SLD  $R_b$  analysis,  $\epsilon_b^\mu$  is the efficiency for a double tag

## 6.6 Flavour tag calibration

---

(from Monte Carlo), and  $\epsilon_b^\mu$  is the efficiency calculated in the muon hemisphere.  $\epsilon_b^\mu$  can be obtained from data or Monte Carlo using the following relation:

$$\epsilon^\mu = \epsilon_b^\mu P_b^0 + \epsilon_c^\mu P_c^0 + \epsilon_{uds}^\mu P_{uds}^0, \quad (6.10)$$

where  $\epsilon^\mu$  is the efficiency for a  $B$  tag in the muon hemisphere once there has been a tag in the opposite hemisphere;  $P_x^0$  ( $x = b, c, u, d, s$ ) are the purities of  $x\bar{x}$  events in the high mass region (from Monte Carlo);  $\epsilon_c^\mu$  ( $\epsilon_{uds}^\mu$ ) are the efficiencies for a  $c\bar{c}$  ( $u\bar{u}$ ,  $d\bar{d}$ ,  $s\bar{s}$ ) event to be tagged as a  $b\bar{b}$  event in the muon hemisphere (from Monte Carlo). The values of  $\epsilon_b^\mu$  obtained from data and Monte Carlo are then substituted into Eq. 6.10 to give the respective values for  $\epsilon_b$ . The ratio between them, calculated in different bins of the jet axis  $|\cos\theta|$  is then used to correct the MC flavour composition according to the data ( $\sim 5\%$  correction on average). Formulae similar to Eq. 6.9 are valid for  $c\bar{c}$  and  $uds$  events in the high mass region:

$$\epsilon_c = \epsilon_c^0 + \epsilon_c^\mu - \epsilon_c^d \quad (6.11)$$

$$\epsilon_{uds} = \epsilon_{uds}^0 + \epsilon_{uds}^\mu - \epsilon_{uds}^d,$$

where all components are taken from Monte Carlo, except for  $\epsilon_b^0$  taken from the SLD  $R_b$  measurement. Two assumptions have been implicitly made so far: 1) we expect the  $B$  tag efficiency to be the same in a generic  $B$  decay for events with a muon in the opposite hemisphere and events without a muon; 2) the same acceptance is assumed for this and the  $R_b$  analysis. The formulae presented here are mathematically correct only if there is no correlation between the two hemispheres. Introducing a correlation factor  $\lambda_b^\mu$  defined

## 6.6 Flavour tag calibration

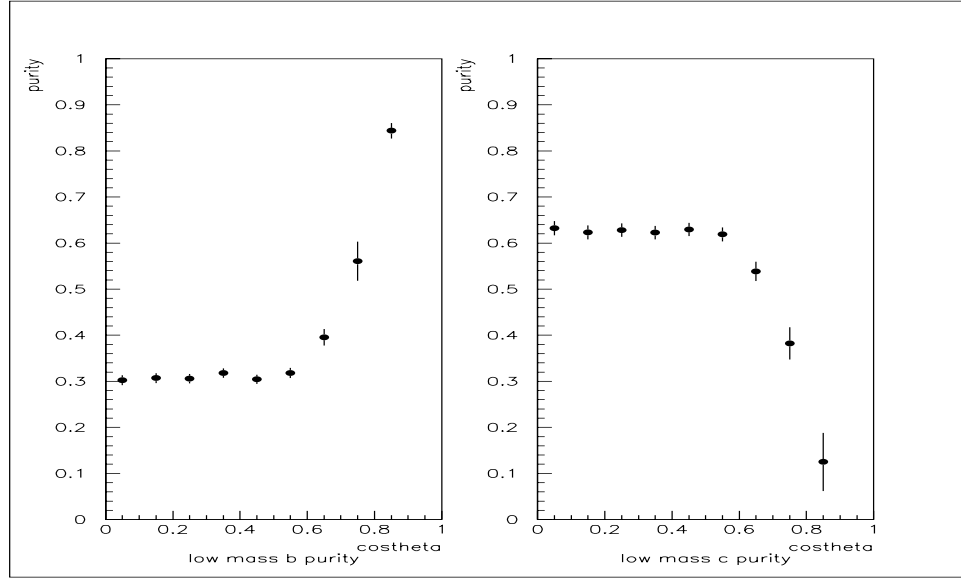


**Figure 6.14:** Dependence of the  $B$  tag (left) and  $ct$  tag (right) purities on the  $\cos\theta$  of the jet axis in the low mass region.

as:

$$\lambda_b^\mu \equiv \frac{\epsilon_b^d - \epsilon_b^{\mu MC} \epsilon_b^0}{\epsilon_b^{\mu MC} - \epsilon_b^{\mu MC} \epsilon_b^0}, \quad (6.12)$$

the efficiency for a correct  $B$  tag in the high mass region will then become:

$$\epsilon_b = \epsilon_b^0 + \frac{\epsilon_b^\mu \epsilon_b^0}{\epsilon_b^0 + \lambda_b^\mu (1 - \epsilon_b^0)} - \epsilon_b^d. \quad (6.13)$$

In the low mass region similar formulae hold, but more complicated, because of the veto on a high vertex mass in either hemisphere. We have:

$$\epsilon_x = \epsilon_x^0 + \epsilon_x^\mu(\lambda) - \epsilon_x^d - \epsilon_x^{veto}, \quad (6.14)$$

where  $x = b, c, uds$  and  $\epsilon_x^{veto}$  is the mixed tag efficiency calculated from Monte Carlo. Two correlation coefficients  $\lambda_b^\mu$  and  $\lambda_c^\mu$  need to be accounted for in this case.

An effect that has been observed during some checks on the performance of the flavour tags is a dependence of the tag purities on the jet direction at high  $|\cos\theta_{jet}|$  especially

## 6.7 Fit Results

---

Parameter	Adopted value
$A_e$	0.1520
$M_b$	4.5 GeV/c <sup>2</sup>
$M_c$	1.5 GeV/c <sup>2</sup>
$\sin^2 \theta_W$	0.23055
$\alpha_s$	0.119
$M_Z$	91.1863 GeV/c <sup>2</sup>

**Table 6.3:** Values adopted for some physical quantities in the fit.

in the low mass region (see fig. 6.14). In particular, for  $|\cos \theta_{jet}| > 0.7$  the charm tag purity drops steadily down from a constant value of  $\sim 60\%$  in the barrel region whereas the  $b$  tag purity has a correspondent gradual increase. In order to account for this effect, MC  $b\bar{b}$ ,  $c\bar{c}$  and  $uds$  events in the three  $\sqrt{p_t}$  vs  $0.5 \cdot \ln p$  planes have been given a weight proportional to the fractional increase (or decrease) of the corresponding flavour tag purity at  $|\cos \theta| > 0.7$ .

Furthermore, even if such a large effect was not observed for the tag efficiencies, we decided to include a  $|\cos \theta|$  dependence in all the variables used for the tag calibration as illustrated above (equations 6.8 through 6.12), substituting for scalar quantities  $n$ -dimensional vectors with the values assumed by the same variables in  $n$  different bins of  $|\cos \theta|$ .

## 6.7 Fit Results

Taking into account the corrections described so far, the maximum likelihood method, described in section 6.2 has been applied to the probability function (Eq. 6.4), assuming a set of values for some physical quantities used in the fit as listed in table 6.3. Almost all of these quantities are only used in the calculation of QCD corrections, and

## 6.7 Fit Results

---

therefore uncertainties in their values lead to negligible variations on the fit results.  $A_e$  is fixed in the fit to  $0.1514 \pm 0.0022$  (in agreement with the result of the  $A_{LR}$  analysis [18]), but it could also be left as a free parameter and fitted together with the heavy quarks asymmetries: its value in that case would be  $0.1418 \pm 0.0092$  (1996-1998), with a small effect on  $A_b$  and  $A_c$  ( $< 0.1\%$  relative difference).

Since both parameters are present in the probability function that is maximized in the likelihood fit, it is possible to obtain measurements of both  $A_b$  and  $A_c$  at the same time. However, this analysis is mostly optimized to measure  $A_b$  and the analyzing power for an  $A_c$  measurement is not very high, due to the difficulty of separating charm and background with the tagging variables used. Therefore the importance of the  $A_c$  measurement should be considered as secondary with respect to  $A_b$ , and the results which are presented here only preliminary (further checks on their consistency would be needed before proceeding to an official release).

The results from a simultaneous fit to  $A_b$  and  $A_c$  are:

$$A_b = 0.947 \pm 0.084(stat) \tag{6.15}$$

$$A_c = 0.542 \pm 0.110(stat)$$

for 1993-1995 data,

$$A_b = 1.000 \pm 0.118(stat) \tag{6.16}$$

$$A_c = 0.637 \pm 0.170(stat)$$

for 1996 and

$$A_b = 0.916 \pm 0.047(stat) \tag{6.17}$$

## 6.7 Fit Results

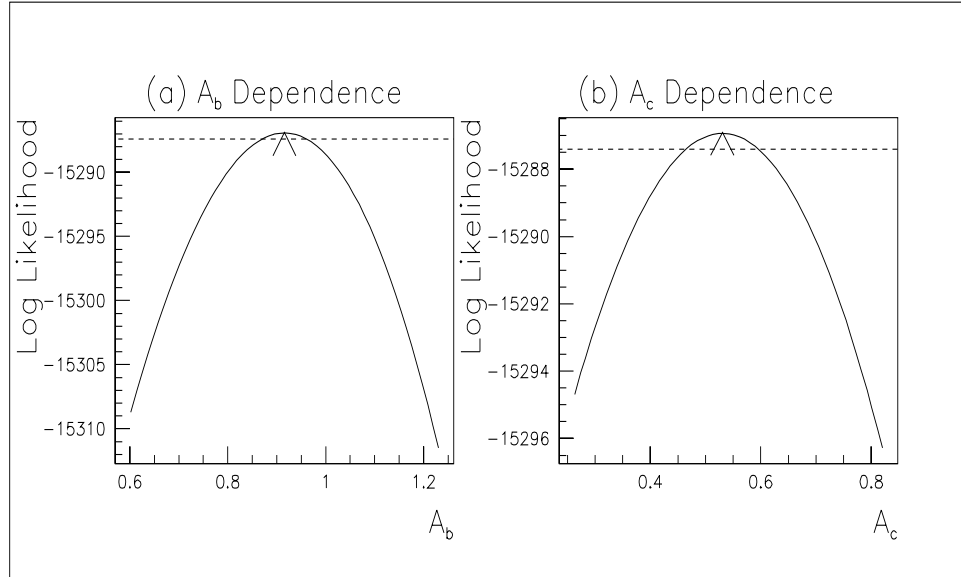


**Figure 6.15:** Variation of the logarithm of the maximum likelihood function as a function of  $A_b$  and  $A_c$  around the maxima for 1997-1998 data. (a) Variation as a function of  $A_b$  (with  $A_c$  fixed to the fit result value). (b) Variation as a function of  $A_c$  (with  $A_b$  fixed).

$$A_c = 0.530 \pm 0.068(stat)$$

for 1997-1998 data, where the errors are just from data statistics.

Fig. 6.15 shows the logarithms of the maximum likelihood function for  $A_b$  and  $A_c$  (1997-1998 data fit). The correlation coefficients between  $A_b$  and  $A_c$  are +0.138 for 1993-95 data, +0.114 for 1996 and +0.108 for 1997-98 (see fig. 6.16).

Further corrections have to be added to the central values derived from the fit, as a result of second order QCD effects which will be described later and of Initial-State-Radiation and  $\gamma/Z$  interference effects (the 2 latter ones have been estimated to produce a  $\sim -0.2\%$  ( $\sim +0.12\%$ ) correction [97] on  $A_b$  ( $A_c$ ) using ZFITTER 6.23 [98]). The absolute variations are  $\Delta A_b = 1.1 - 1.6\%$  and  $\Delta A_c \sim 1.5 - 2\%$ .

The above results take into account corrections related to the fact that some of the branch-

6.7 Fit Results

---

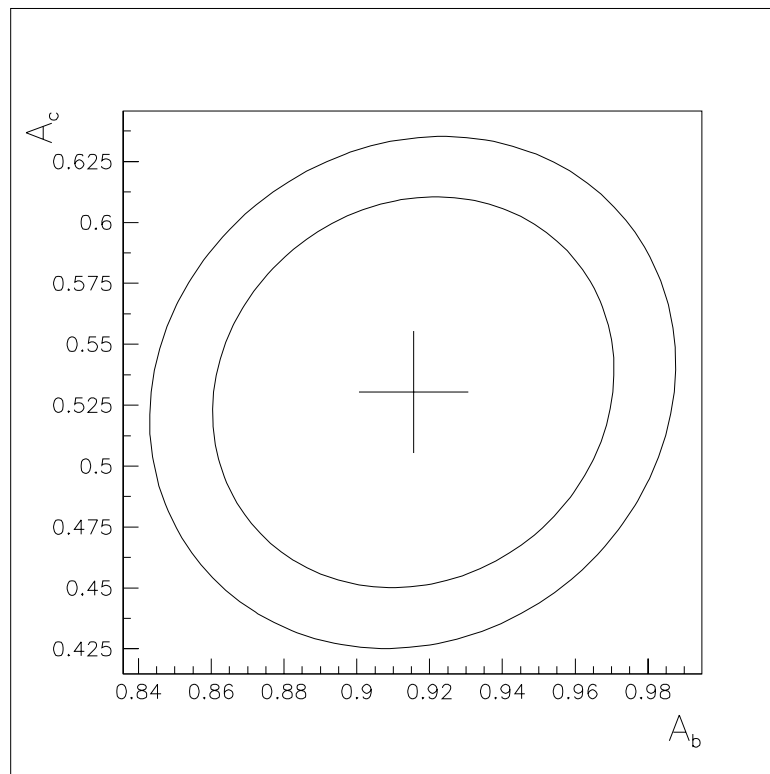


**Figure 6.16:** Contours relative to one and two standard deviations of the logarithm of the maximum likelihood function for 1997-1998 data.

## 6.8 Comparison with a different technique (1)

---

Decay channel	SLD MC 1993-1995	SLD MC 1996-98	World Average
$b \rightarrow \mu^-$	10.75%	10.96%	$10.62 \pm 0.17\%$
$b \rightarrow c \rightarrow \mu^+$	9.34%	8.61 %	$8.07 \pm 0.25\%$
$b \rightarrow \bar{c} \rightarrow \mu^-$	0.90%	1.70%	$1.62 \pm 0.40\%$
$c \rightarrow \mu^+$	10.30 %	9.10%	$9.85 \pm .32\%$
$b \rightarrow \tau \rightarrow \mu^-$	0.42%	0.50%	$0.45 \pm 0.07\%$
$b \rightarrow J/\psi \rightarrow \mu^+ \mu^-$	0.09%	0.07%	$0.07 \pm 0.02\%$

**Table 6.4:** Branching ratios in the SLD Monte Carlo, compared with the world averages [15].

ing ratios in the SLD Monte Carlo are different from the world average values listed in table 6.4. The final results are then:

$$A_b = 0.9630 \pm 0.0842(stat) \quad (6.18)$$

$$A_c = 0.5573 \pm 0.1103(stat)$$

for 1993-1995 data,

$$A_b = 1.0158 \pm 0.1178(stat) \quad (6.19)$$

$$A_c = 0.6664 \pm 0.1705(stat)$$

for 1996 data, and

$$A_b = 0.9266 \pm 0.0467(stat) \quad (6.20)$$

$$A_c = 0.5441 \pm 0.0679(stat)$$

for 1997-1998 data (errors are just from data statistics).

## 6.8 Comparison with a different technique (1)

As a first crosscheck of these numbers, we have repeated the  $A_b$  measurement using an approach that is more intuitive and direct than the maximum likelihood method.

## 6.8 Comparison with a different technique (1)

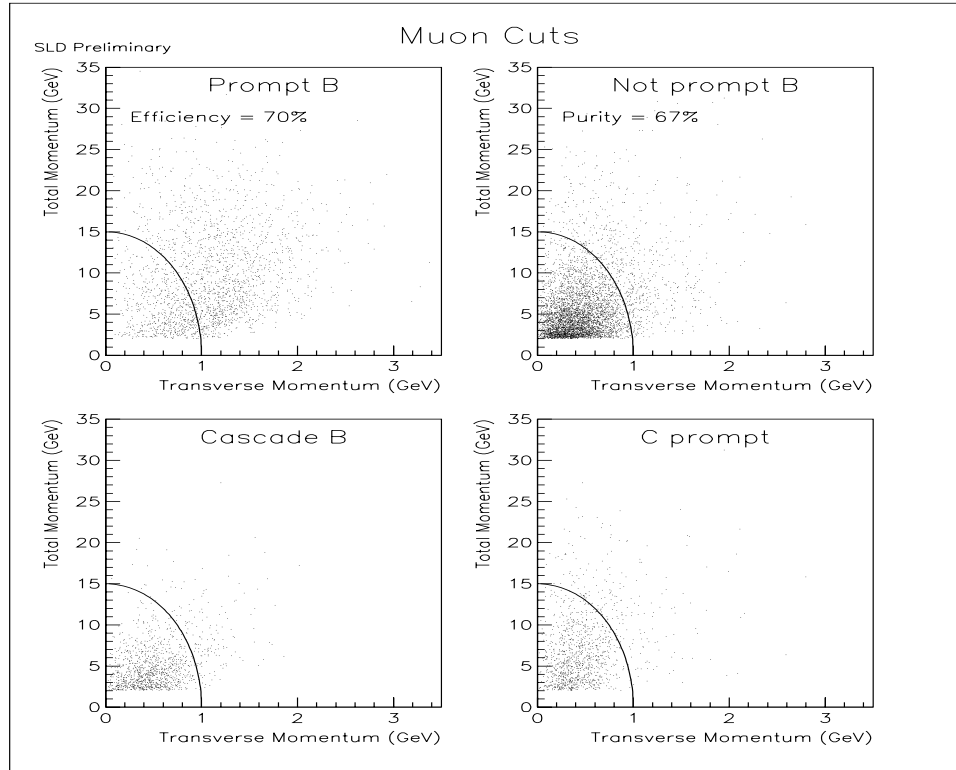


**Figure 6.17:** Elliptic cut on the total and transverse momenta for muons coming from  $b$  direct decays (top left), from all other sources (top right), from  $b$  cascade decays (bottom left) and from  $c$  decays (bottom right).

We have selected a sample of events enriched in  $B$  hadrons direct decays by applying an elliptic cut on the total and transverse momenta of the muon tracks. The cut chosen in this case is:

$$\sqrt{\left(\frac{p}{15.0}\right)^2 + \left(\frac{p_t}{1.0}\right)^2} > 1.0 \quad (6.21)$$

which is shown in fig. 6.17 for muons coming from different sources. The cut has an efficiency of  $\sim 70\%$  and a purity of  $67\%$ , from the simulation. Moreover, to further enrich our sample we have required that the mass  $M$  of the event (defined again as the highest of the two vertex masses reconstructed in the two hemispheres of the event) satisfy:  $M > 0.55$   $\text{GeV}/c^2$  and, if  $M < 2$   $\text{GeV}/c^2$ ,  $15 \cdot M - p_{vtx} > 10$ , where  $p_{vtx}$  is the correspondent vertex

## 6.8 Comparison with a different technique (1)

---

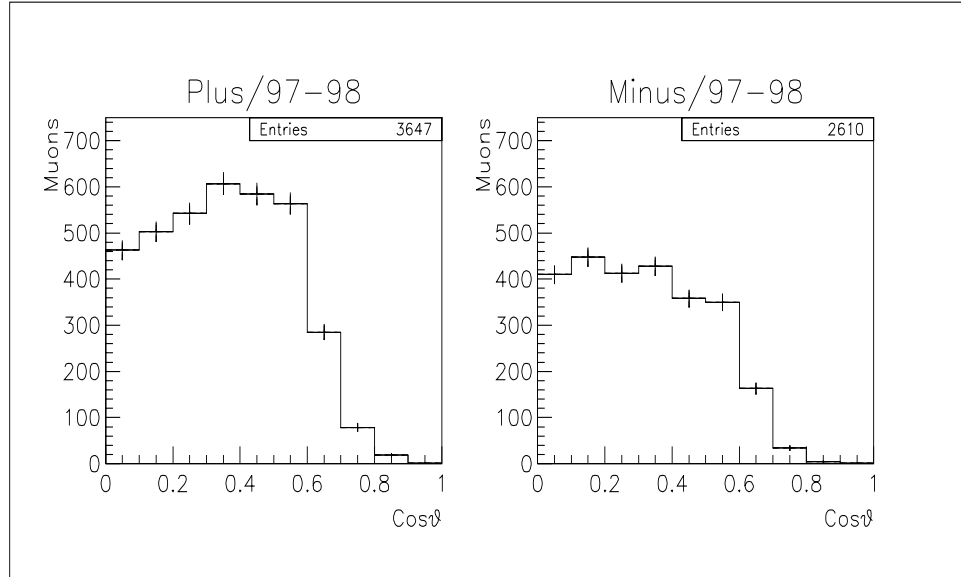


**Figure 6.18:** Histograms used to calculate the polarized forward-backward asymmetry in  $|\cos\theta|$  intervals.

momentum. The sample selected (using 1997-1998 data only) consists of 6257 muons from all the different sources. In order to estimate the asymmetry of the background, we have used the same functional form dependent on the total and transverse momenta of the muon track that has been derived previously for the maximum likelihood analysis (see section 6.4.3). The average value of the distribution (0.0366) is used in this study.

The selected muons have been divided in two histograms according to the sign of the quantity:

$$M = Q \times P_e \times \cos \theta,$$

where  $Q$  is the muon charge,  $P_e$  is the polarization and  $\cos \theta$  is the angle of the jet associated with the muon. The two histograms are shown in fig. 6.18. More interesting from a physical point of view are the distributions of the quantity  $-Q \cdot \cos \theta$ , which represents the  $b$  quark direction, illustrated in fig. 6.19. For every  $|\cos \theta|$  interval of the histograms in fig. 6.18

## 6.8 Comparison with a different technique (1)

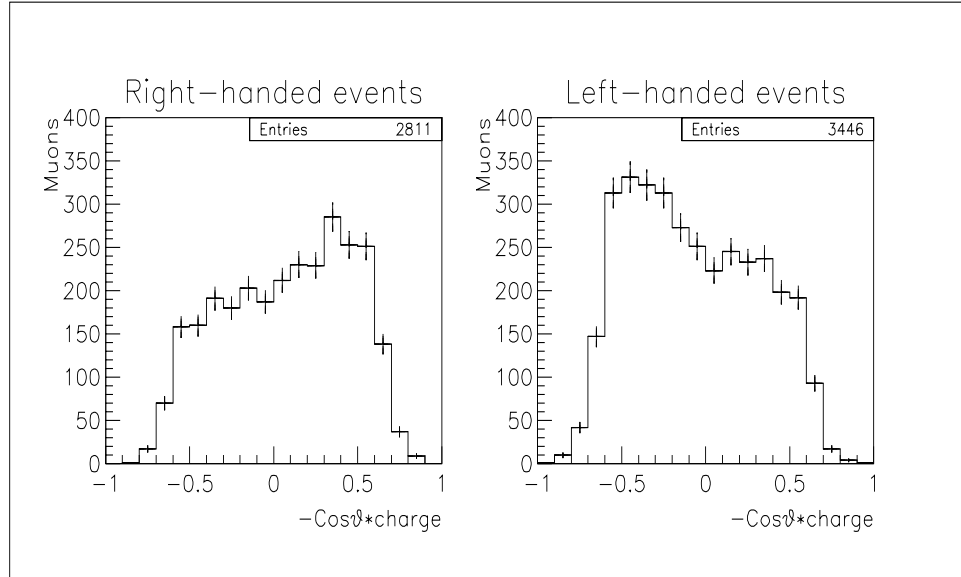


**Figure 6.19:** Distributions of the quantity  $-Q \cos \theta$ , which gives the  $b$  quark direction, for events with positive and negative polarization respectively.

we form an asymmetry:

$$A_i = \frac{N_i^+ - N_i^-}{N_i^+ + N_i^-}, \quad (6.22)$$

where  $N_i^+$  and  $N_i^-$  are the number of muons in the  $i$ -th  $|\cos \theta|$  interval of the *Plus* and *Minus* histograms respectively. The statistical error on the asymmetry is given by:

$$\Delta A_i = \sqrt{\frac{4N_i^+ N_i^-}{(N_i^+ + N_i^-)^3}}. \quad (6.23)$$

The polarized forward-backward asymmetry is shown in fig. 6.20, along with the fit performed with Eq.1.15, which takes into account  $b$  quark mass effects and first order QCD corrections. The mitigation factor on the QCD corrections (as calculated in the maximum likelihood analysis) has been applied too. The result of the fit is:

$$\tilde{A}_{FB}^{fit} = 0.2992 \pm 0.0211(stat)$$

with  $\chi^2 = 2.2$  for 6 degrees of freedom. This value has to be corrected for non- $b$  events

## 6.8 Comparison with a different technique (1)

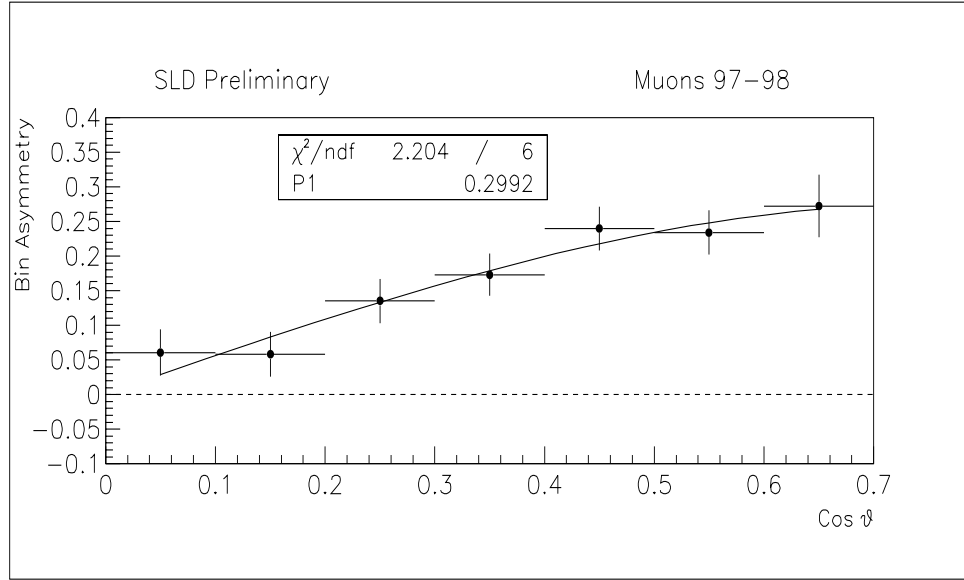


**Figure 6.20:** Asymmetry fit as a function of  $\cos \theta$ .

that pass the elliptic+mass cut. Summing up their contribution to the asymmetry, and assuming  $A_c$  equal to the Standard Model value, the observed asymmetry results:

$$A^{fit} = A_b(0.3599 \pm 0.0029) + (-0.0387 \pm 0.0009),$$

where the signal and background contributions to  $A_b$  have been isolated. Combining the two previous results we get:

$$A_b = 0.939 \pm 0.059,$$

which is consistent with the result found with the maximum likelihood method (6.17). The statistical error is in this case higher due to the cuts applied on the available statistical sample of events.

## 6.9 Comparison with a different technique (2)

---

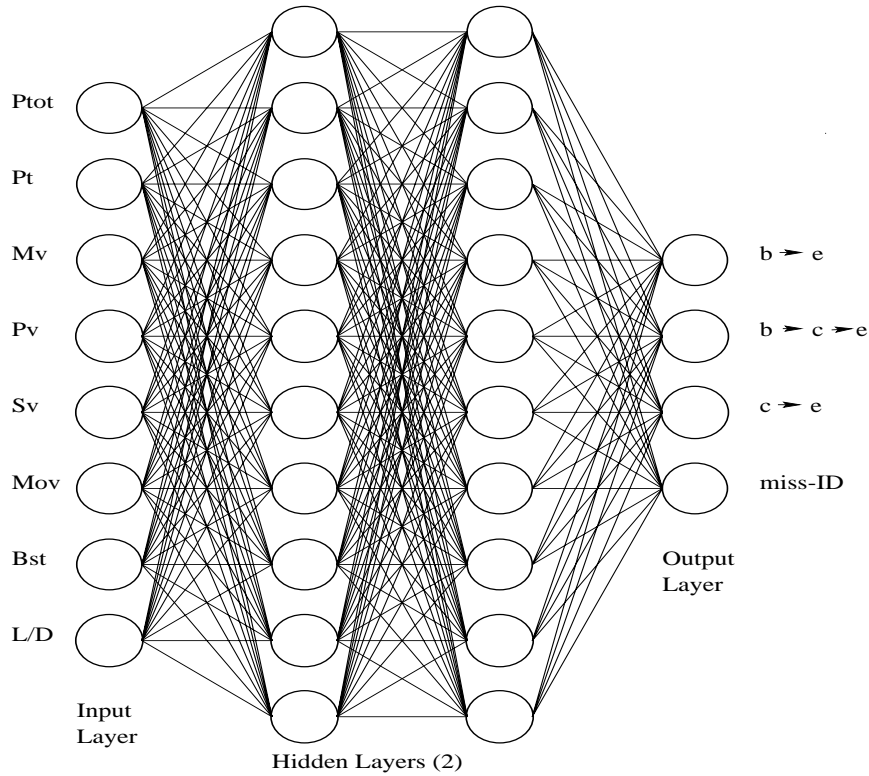


**Figure 6.21:** The architecture used for the source classification neural net (8-10-10-4). It is a full connection, feed forward with back-propagation neural network.

## 6.9 Comparison with a different technique (2)

In a second crosscheck, we have adopted again a maximum likelihood technique, but this time using a neural net to calculate the decay source probabilities of muons. The procedure followed reproduces with small changes the one adopted for the parallel analysis with electrons [99], to which we refer for further details and for a description of the main principles of artificial intelligence.

The package used is the Stuttgart Neural Network Simulator (SNNS) [100]. We have built a feed-forward, back-propagation network with an architecture of 8 input nodes, 10 hidden nodes in each of the 2 hidden layers and 4 output nodes (see fig. 6.21). The architecture

## 6.9 Comparison with a different technique (2)

---

has been optimized for this analysis by pruning input and hidden nodes to keep only the most contributing ones. The eight kinematic and topological variables used as inputs are:

- the muon momentum,
- the transverse momentum with respect to the nearest jet axis,
- the same-hemisphere vertex mass, vertex momentum and vertex significance (defined as the decay length divided by the vertex error width),
- the opposite-hemisphere mass,
- the boost  $\beta\gamma$  of the underlying  $B$  meson,
- L/D.

The training parameters were optimized by minimizing the training set error and by trying to achieve a good separation between signal and background. The best values found were:  $\eta = 0.15$  (*learning rate*),  $T = 1.0$  (*temperature*, a parameter in the node activation function) and  $N = 20,000$  (*number of training cycles*).

The neural network was trained on a sub-sample of the 1997 Monte Carlo. Since the training behaviour is improved if the different source signals are in roughly equal proportions, the all-flavours MC was enhanced by the use of extra  $Z^0 \rightarrow c\bar{c}$  MC.

The performance of the net is monitored with a test set which is independent of the training set (a different sub-sample of the 1997 Monte Carlo). The training process is interrupted every few cycles and the network is run on the test set to compare errors between output node values and MC truth values. If the test set error diverges, it is a sign that the network

## 6.9 Comparison with a different technique (2)

---

is *overtraining*, i.e. that it is unable to analyze new data.

The 4 outputs of the net range from 0 to 1 and correspond to the sources:  $b \rightarrow \mu$ ,  $b \rightarrow c \rightarrow \mu$ ,  $c \rightarrow \mu$  and background. For the analysis, these outputs have been projected into a two-dimensional space parametrized by  $x = OUT_b + OUT_{bc}$  and  $y = OUT_b + OUT_c$ , where  $OUT_b$ ,  $OUT_{bc}$ ,  $OUT_c$  are the values of the  $b$  direct,  $b$  cascade, and  $c$  direct output nodes respectively. If a muon comes from a  $b$  direct decay, it will be projected around the (1,1) point of this space; if it comes from a  $b$  cascade decay, it will be found around the (1,0) point; if it comes from a  $c$  direct decay it will be around the (0,1) point and finally if it is a background muon then it will populate the area around the origin. Fig. 6.22 shows this representation for the 1997-1998 Monte Carlo (after excluding the events used for the network training): it is evident how we can achieve a fairly good separation of the  $b$  channels from each other and from the background, whereas it is more difficult to distinguish the charm contribution from the background. Therefore, only a measurement of  $A_b$  has been obtained with this method.

$A_b$  is measured by fitting to the maximum likelihood function (Eq. 6.4) after calculating the source probabilities from the 2-D Dalitz representation of the neural net outputs. First all the available (1997-1998) Monte Carlo is passed through the neural net and projected in the 2-D space. This is then binned into a  $50 \times 50$  grid. Data events are then passed through the neural net, and projected in the Dalitz space. The source probabilities of each event are then derived from the fractions of MC events of each source in the corresponding bin of the 2-D Dalitz space. If the statistics in the bin is too low, the window for calculating the weights is enlarged from  $1 \times 1$  to a  $3 \times 3$  (in bin units).  $B$  mixing, background

## 6.9 Comparison with a different technique (2)

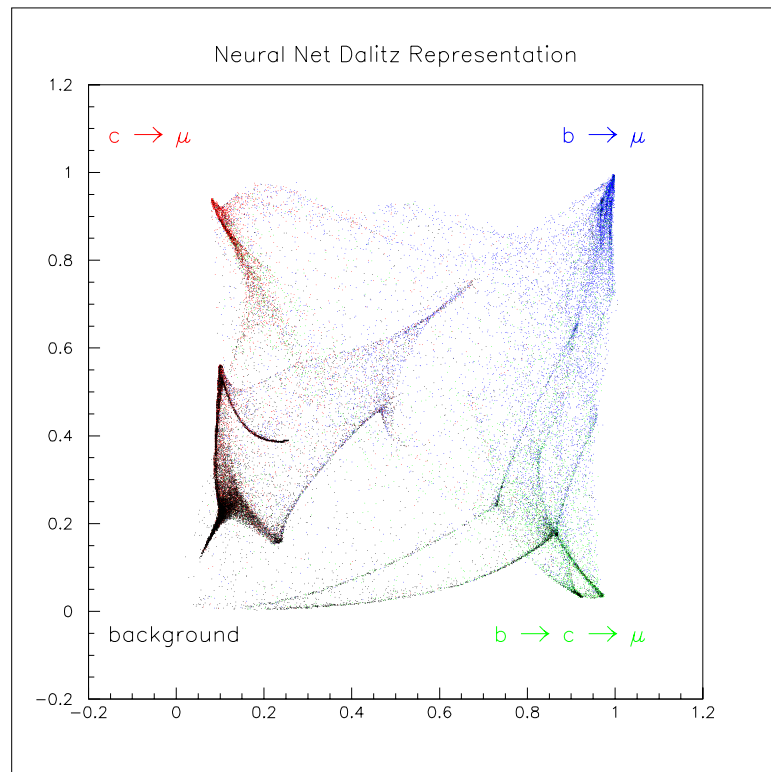


**Figure 6.22:** Two-dimensional representation of the output nodes, with axes defined by  $x = OUT_b + OUT_{bc}$  and  $y = OUT_b + OUT_c$ .

## 6.10 Systematic Errors

---

asymmetry and QCD corrections are treated as in the multi-variate maximum likelihood approach.

The result of the fit ( $A_b$  only) is:

$$A_b = 0.930 \pm 0.052,$$

again consistent with our multi-variate measurement.

## 6.10 Systematic Errors

Given the strong reliance on the Monte Carlo simulation, there are many sources of systematic errors in this analysis, including: the simulation of  $B$  and  $D$  hadron decays, the detector resolution, the background simulation and the input values of physical quantities used in the analysis. All of these are considered in detail as follows.

### 6.10.1 Monte Carlo statistics

The error due to the limited statistics in the simulation is estimated by dividing the Monte Carlo population into 4 sub-samples with one quarter of the total statistics each, and by refitting for  $A_b$  and  $A_c$  using only weights derived from each of these subsamples (after rescaling the size of the search area for the nearest neighbours technique in the 3-D phase space). The average of the four fits is calculated along with the standard deviation, whose value divided by two (to relate to the total statistics, instead of only one fourth) is taken as systematic error due to the MC statistics. This gives:  $\Delta A_b = 0.0038$ ,  $\Delta A_c = 0.0194$  (1993-98 combined).

## 6.10 Systematic Errors

---

### 6.10.2 Jet axis simulation

Uncertainties in the jet axis simulation can affect the asymmetry measurement by distorting the lepton  $p_t$  spectrum and, to a lesser extent, the jet direction. This effect has been studied by comparing the back-to-back direction of jets for data and MC in two-jet events. The jet axis resolution has been found to be slightly worse in MC than in the data, which could be a consequence of an imperfect simulation of electromagnetic showers in the calorimeter or of the choice of the parameter related to the width of the transverse momentum distribution in JETSET. An improvement is obtained by “smearing” the jet angle in the data randomly according to a Gaussian distribution with a 10 mrad width (15 mrad for 1997-98 data). This effect is obtained in the analysis by varying the transverse momentum of the muon track by:

$$p'_t = p \sqrt{(p_t/p + r_1 \Delta\phi)^2 + (r_2 \Delta\phi)^2}, \quad (6.24)$$

where  $p$  is the total momentum,  $r_1, r_2$  are randomly chosen according to a Gaussian distribution and  $\Delta\phi=0.010(0.015)$ (see fig. 6.23). A conservative way to estimate the systematic error is to apply the equation 6.24 to Monte Carlo muons, thus worsening their resolution and to recalculate  $A_b$  and  $A_c$ . This is justified by the assumption that, the problem relying on data simulation, the systematic uncertainty will be the same worsening or improving the Monte Carlo resolution. The error has been calculated as the mean variance on a sample of 20 different fits obtained using different *seeds* for the random number generator:  $\Delta A_b = 0.0020$ ,  $\Delta A_c = 0.0017$ .

## 6.10 Systematic Errors

---

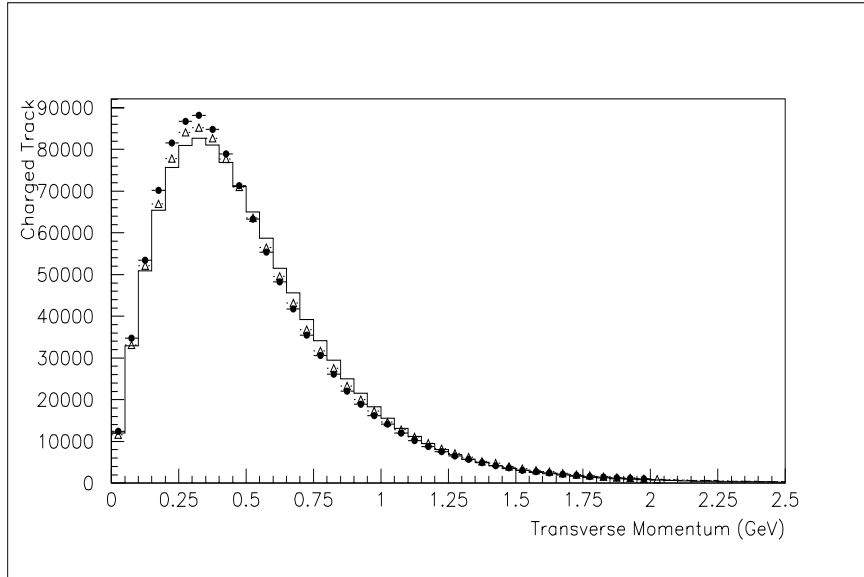


**Figure 6.23:** Transverse momentum distribution of all charged tracks in 1997-98 Monte Carlo (histogram) and in the data before (dots) and after (open triangles) applying the smearing.

### 6.10.3 Tracking Efficiency

This analysis is independent of tracking efficiency unless such efficiency depends on  $p$ ,  $p_t$  or is not symmetric in  $\cos \theta$ . The extent of this dependence has been calculated by reweighing MC tracks by the data to MC ratio of the number of tracks as a function of  $p$  and  $p_t$ . In fig. 6.24 are shown data and MC distributions of the logarithm of the total momentum of charged tracks with  $p > 2 \text{ GeV}/c$ ,  $|\cos \theta| < 0.7$  and impact parameter less than 1.5 cm in the  $z$  coordinate. At low momenta there are more tracks in the Monte Carlo than in the data, and vice-versa for high momenta: the ratio can be approximated with a linear fit and the result is used to reweigh the muons in the simulation and redo the maximum likelihood fit for  $A_b$  and  $A_c$ .

We have similarly obtained the transverse momentum distribution (fig. 6.25), after apply-

## 6.10 Systematic Errors

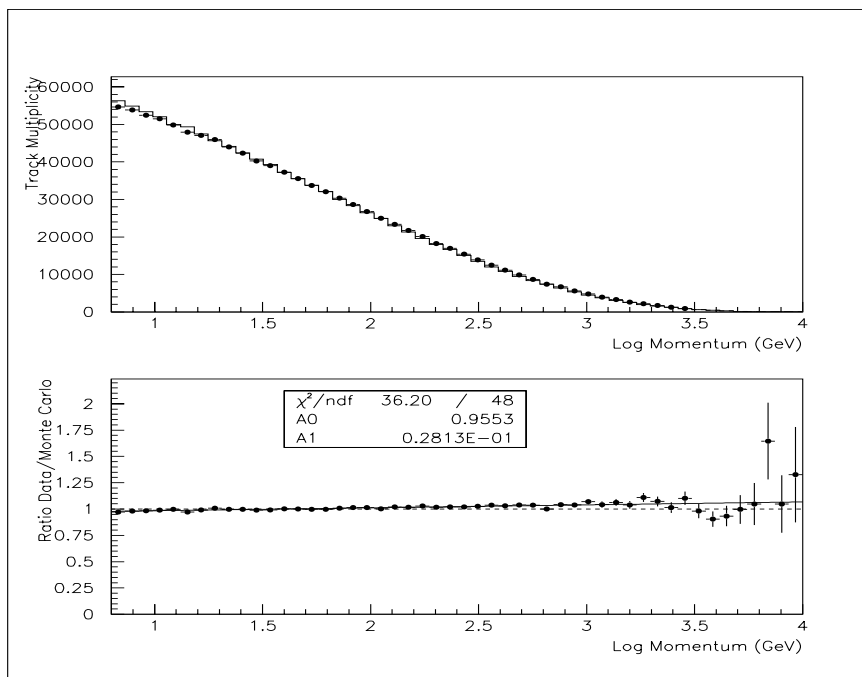


**Figure 6.24:** At the top: comparison between data (dots) and Monte Carlo (histogram) distributions of the logarithm of the total momentum for 1997-98 charged tracks. At the bottom: ratio of the two distributions.

## 6.10 Systematic Errors

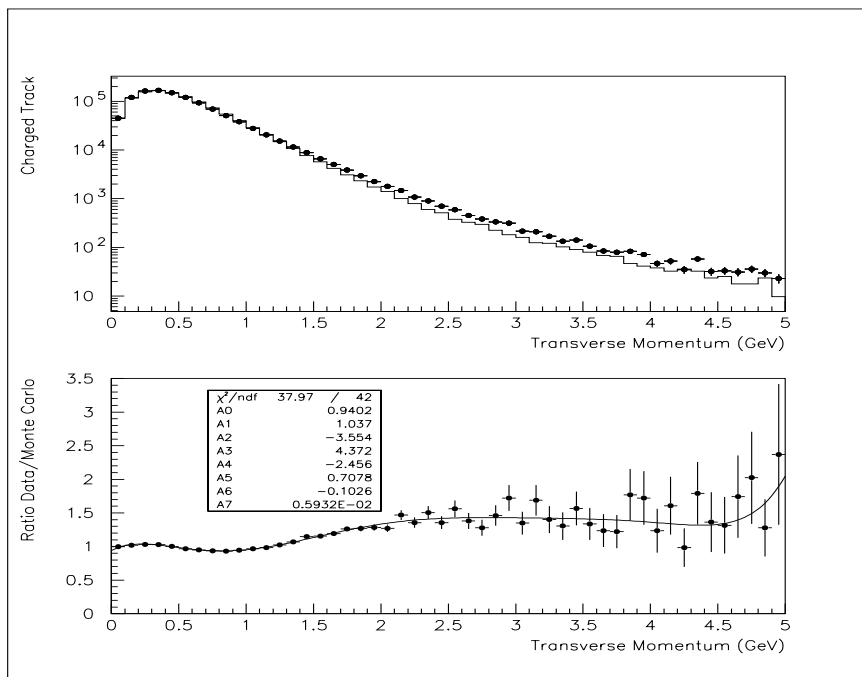


**Figure 6.25:** At the top: comparison between data (dots) and Monte Carlo (histogram) distributions of the transverse momentum for 1997-98 charged tracks after applying a 15 mrad smearing. At the bottom: ratio of the two distributions.

## 6.10 Systematic Errors

---

ing a smearing according to eq. 6.24. In this case there is clearly an excess of data over Monte Carlo at high  $p_t$ . The ratio of the two distributions is more complicated and it has been fitted to a seventh order polynomial. Muons with transverse momentum less than 4 GeV/c have been reweighted according to this polynomial and the variations obtained on  $A_b$  and  $A_c$  have been summed in quadrature to the previous ones to obtain the global systematic error related to tracking efficiency:  $\Delta A_b = 0.0074$  and  $\Delta A_c = 0.0031$ .

### 6.10.4 Background Level in muon identification

From the study with a pure sample of pions from  $K_s^0$  meson decays that has been described in detail in the previous chapter, we have observed a discrepancy of about  $(20 \pm 10)\%$  (Eq. 5.4) in the background level between data and Monte Carlo, with the level in the simulation being lower than in the data. This effect has been accounted for in the analysis by increasing the background source probabilities for every event in the maximum likelihood by +20%. To estimate the related systematic error, the (uncorrected) background level has been increased by 10% and 30% of itself ( $\pm 10\%$  variation, from Eq. 5.4),  $\Delta A_b = 0.0041$  and  $\Delta A_c = 0.0130$ .

Another study related to the background was done on the hadronic production fractions by comparing JETSET  $\pi^\pm$  and  $K^\pm$  rates from a sample of MC charged hadronic tracks with the results of the SLD particle production analyses using 1993-1995 data [101]. The comparison as a function of the total momentum  $p$  is illustrated in fig. 6.26, where dots and triangles indicate pions and kaons in the data respectively, and the lines give

## 6.10 Systematic Errors

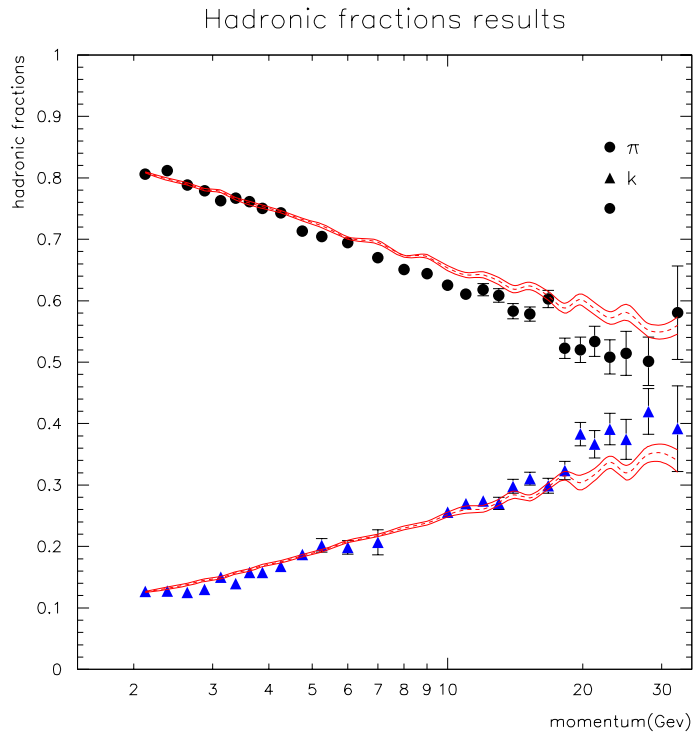


**Figure 6.26:** Comparison between measured charged hadron production fractions and JETSET rates. The dots represent the  $\pi^\pm$  fraction in the data, the triangles the  $K^\pm$  fraction in the data, and the lines represent the one-sigma Monte Carlo bands.

the one sigma bands for the MC rates. The background source fractions in the maximum likelihood function have been rescaled by the data to Monte Carlo fitted ratio (as a function of momentum), with an overall shift on the central values of  $A_b$  and  $A_c$  of approximately  $-0.1\%$  and  $-0.6\%$  respectively.

### 6.10.5 Background Asymmetry

As seen in a previous paragraph, the background asymmetry has been calculated as a function of  $p$  and  $p_t$  from true background muons in the simulation divided into the categories of: i) misidentified muons and ii) muons from light hadron decays. The value of

## 6.10 Systematic Errors

---

the asymmetry has then been rescaled by the data to Monte Carlo ratio of the asymmetry in a sample of charged non-leptonic tracks with a momentum cut at 2 GeV/c, in order to account for possible discrepancies between data and Monte Carlo distributions for the background.

To estimate the systematic error we have just considered the variation in the fitted values of  $A_b$  and  $A_c$  with or without application of this final rescaling, obtaining:  $\Delta A_b = 0.0021$  and  $\Delta A_c = 0.0090$ .

### 6.10.6 $\Gamma(Z^0 \rightarrow b\bar{b}), \Gamma(Z^0 \rightarrow c\bar{c})$ and other branching ratios

Using the most recent measurements for  $R_b$  ( $0.2164 \pm 0.0007$ ) and  $R_c$  ( $0.1674 \pm 0.0038$ ) [15], the uncertainties on these quantities have been taken into account by varying the weights of muons from  $b\bar{b}$  ( $c\bar{c}$ ) events in the maximum likelihood function by  $\pm 0.34\%$  ( $\pm 2.3\%$ ). This gives the variations:  $\Delta A_b = 0.0004$ ,  $\Delta A_c = 0.0006$  ( $R_b$ ) and  $\Delta A_b = 0.0008$ ,  $\Delta A_c = 0.0085$  ( $R_c$ ).

Uncertainties on specific branching ratios have been accounted for in a similar way by varying the correspondent event source probability by a percentage equal to the relative statistical error on the world average measurement for that rate (as listed in table 6.4).

Variations for all cases are shown in tables 6.5 and 6.6.

### 6.10.7 $B^\pm, B^0$ and $B_s$ meson decay lepton spectrum

The SLD Monte Carlo modelling of the momentum spectrum of muons from semileptonic decays of  $B^\pm$  and  $B^0$  mesons reproduces measurements performed at CLEO [102].

## 6.10 Systematic Errors

---

The main uncertainty is related to how the spectrum divides between  $B$  direct and cascade decays, and it is connected in particular to the knowledge of the branching ratio  $b \rightarrow D^{**} + \mu + \nu_\mu$ . To estimate the relative systematic error, the fraction of muons produced in this decay ( $\sim 23\%$  of muons from  $b$  decays) has been varied by  $\pm 10\%$ , consequently varying the other fractions to keep  $R_b$  constant.

For  $B_s$  mesons a variation of  $\pm 20\%$  has been applied to 1993-1995 data and of  $\pm 10\%$  to 1996-1998 data (due to different fractions in the Monte Carlo). Summing up in quadrature the two variations, the total systematic error related to the  $B \rightarrow D^{**}\mu\nu$  fraction is:  $\Delta A_b = 0.0033$ ,  $\Delta A_c = 0.0025$ .

### 6.10.8 $D$ meson decay lepton spectrum

The model adopted in the SLD MC for  $D$  meson semileptonic decay reproduces  $D \rightarrow l$  data recorded by DELCO [103] and MARK III. These measurements however are affected by large errors. The systematic error due to these uncertainties has been estimated by constraining the ACCMM model [104] to these data. This model has two parameters that can be fixed: the Fermi momentum  $p_f$  and the mass  $m_q$  of the quark produced in the heavy quark decay. The data from DELCO and MARK III have been fitted to this model [105] using  $m_q = 0.001 \pm 0.152 \text{ GeV}/c^2$  and  $p_f = 0.467_{-0.114}^{+0.205} \text{ GeV}/c$ . The distributions used to estimate the systematic error are: ACCMM1 ( $m_q = 0.001 \text{ GeV}/c^2$  and  $p_f = 0.467 \text{ GeV}/c$ ), ACCMM2 ( $m_q = 0.001 \text{ GeV}/c^2$  and  $p_f = 0.353 \text{ GeV}/c$ ) and ACCMM3 ( $m_q = 0.153 \text{ GeV}/c^2$  and  $p_f = 0.467 \text{ GeV}/c$ ). The momentum spectrum of Monte Carlo muons from  $D$  meson decay has been varied according to the ratios

## 6.10 Systematic Errors

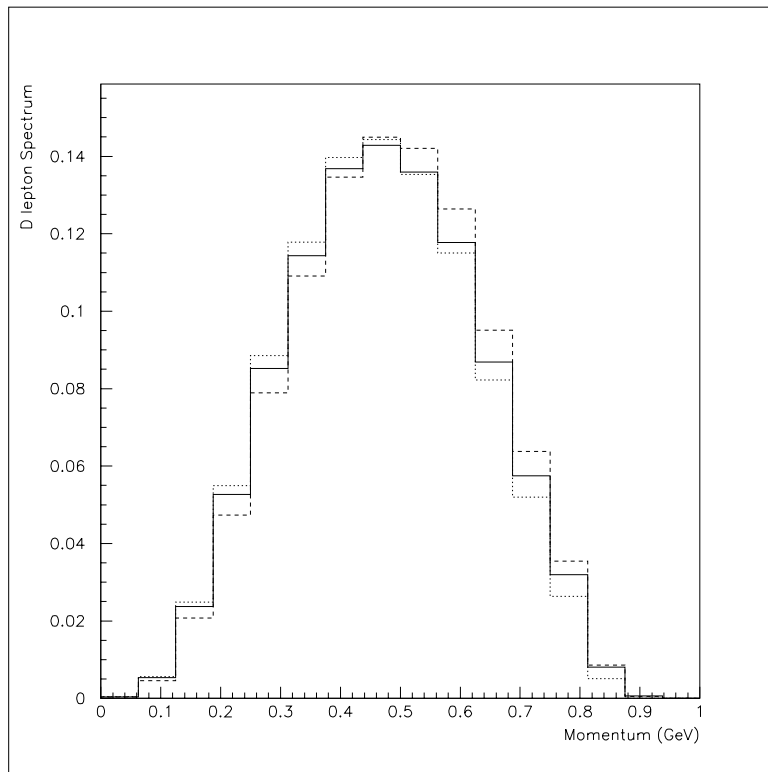


**Figure 6.27:** Variations (dashed lines) in the momentum spectrum of muons from  $D$  hadron decays adopted to estimate the systematic error, as compared to the SLD MC (solid line).

ACCMM2/ACCMM1 and ACCMM3/ACCMM1 (see fig. 6.27), obtaining the variations:

$$\Delta A_b = 0.0042, \quad \Delta A_c = 0.0016.$$

### 6.10.9 $B_s$ and $\Lambda_b$ fractions

Another uncertainty to be taken into account is the fraction of leptons produced in  $B_s$  and  $\Lambda_b$  decays.

LEP measurements on  $B_s$  production in  $b\bar{b}$  events give an estimate of the product  $BR(\bar{b} \rightarrow B_s^0) \cdot BR(B_s^0 \rightarrow D_s^- l^+ \nu X)$  [106]. Using the Particle Data Group [7] value for the second branching ratio, we can assume an uncertainty of  $\sim 4\%$  on our knowledge of the  $B_s$

## 6.10 Systematic Errors

---

production fraction. Since the input fraction in our Monte Carlo is around 11.5%, muons in the simulation have been weighted so as to vary this fraction symmetrically between 7.5 and 15.5%, obtaining the variations:  $\Delta A_b = 0.0013$  and  $\Delta A_c = 0.0014$ .

Similar arguments hold when we consider the  $\Lambda_b$  production fraction. In this case LEP measurements give the product  $BR(b \rightarrow \Lambda_b) \cdot BR(\Lambda_b \rightarrow \Lambda_c^+ l^- \bar{\nu} X)$  [107], and with the knowledge of the  $\Lambda_b$  decay branching ratio, we can assume an error of  $\sim 3\%$  on our knowledge of the  $\Lambda_b$  production fraction. Muon weights have been therefore re-weighted as to vary the input value of this fraction in our MC (7.2%) between 4.2 and 10.2%. The variations obtained are:  $\Delta A_b = 0.0018$  and  $\Delta A_c = 0.0011$ .

### 6.10.10 $b$ and $c$ quark fragmentation

The JETSET Monte Carlo generator has been used to simulate hadronization and quark momentum distributions in hadronic events: these influence the momentum spectra of  $B$  and  $D$  hadrons and therefore of their decay products, including muons. Uncertainties on the simulation accuracy are further sources of systematic errors.

The momentum distribution of heavy quarks in the SLD MC is simulated by the Peterson function [69](Eq. 4.3), parametrized by a quantity  $\epsilon_q$  whose value is set at 0.006 for the  $b$  quark and at 0.06 for the  $c$  quark. Early heavy quark fragmentation data [108] [109] were found to be consistent with this model, which was therefore used as the standard in Monte Carlo simulations by many experiments. Uncertainties on the values of  $x_E(b)$  and  $x_E(c)$  (the average beam energy fraction carried by the quark) correspond to variations in the  $\epsilon_q$  parameters. For this analysis we have assumed:  $\epsilon_b = 0.006 \pm 0.0015$  and  $\epsilon_c = 0.06 \pm 0.015$ .

## 6.10 Systematic Errors

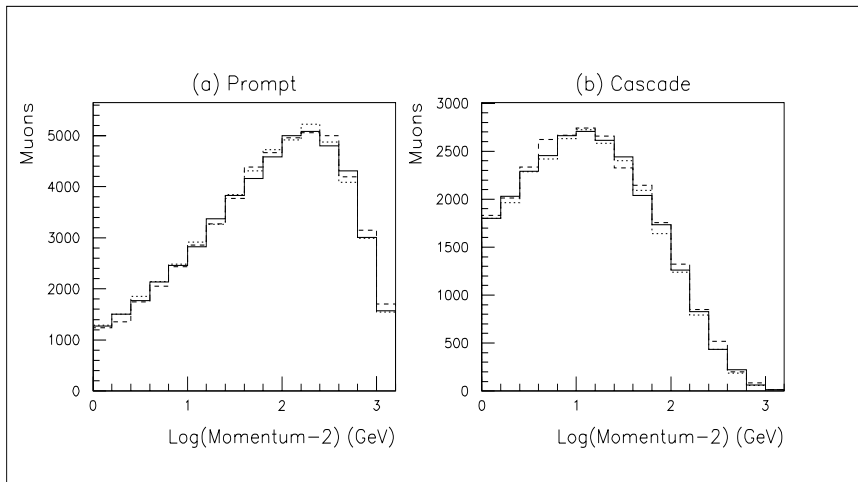


**Figure 6.28:** Momentum distributions for muons from  $B$  hadron direct (left) and cascade (right) decays, for central (solid line) and boundary (dashed lines) values of  $\epsilon_b$ .

Fig. 6.28 shows the momentum distribution of generator level MC muons from  $B$  hadron direct and cascade decays for the central and boundary values of  $\epsilon_b$ . Fig. 6.29 shows the ratio of these distributions, and the fit which is used to weigh events in the simulation. Fig. 6.30 shows the same distributions in the case of  $\epsilon_c$ . Summing up in quadrature the variations for  $\epsilon_b$  (set equal to 0.0045 and 0.0075) and  $\epsilon_c$  (assumed equal to 0.045 or 0.07) yields:  $\Delta A_b = 0.0029$  and  $\Delta A_c = 0.0122$ .

Recent SLD measurements of the  $b$  fragmentation function [110] have shown that the shape of the Peterson functional form is too wide to accurately represent the data and other models might be preferable. Therefore another systematic error has been included, which consists in the uncertainty observed when constraining to our data a phenomenological function derived by ALEPH from measurements of the shape of the  $B$  energy distribution [111]. We have compared the momentum distributions of generator level muons from  $B$  hadron direct and cascade decays when adopting the standard Peterson fragmentation

## 6.10 Systematic Errors

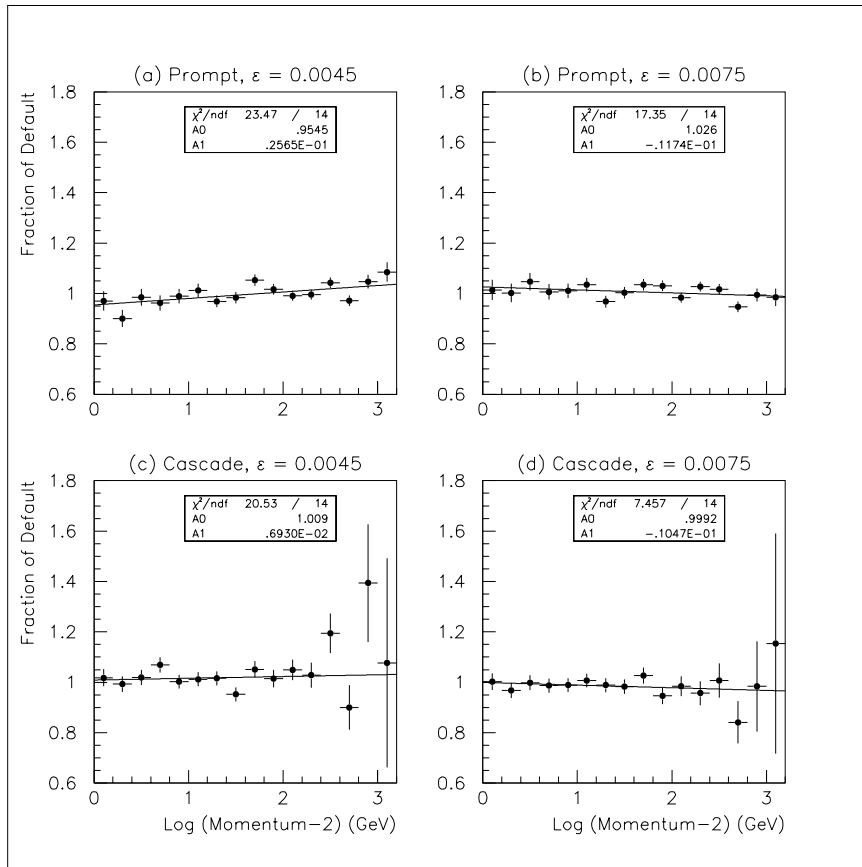


**Figure 6.29:** Ratio of the momentum distributions of muons from simulations with different values of  $\epsilon_b$  and the fit used to weigh events in the Monte Carlo to calculate systematic errors.

## 6.10 Systematic Errors

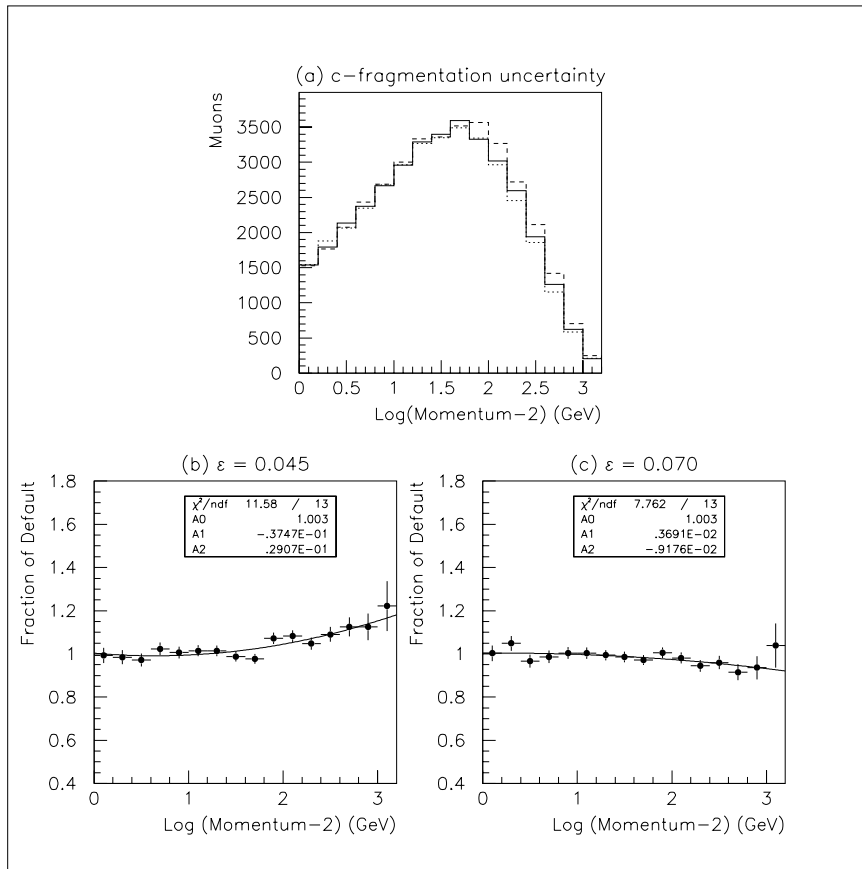


**Figure 6.30:** (Top): variations in the momentum distributions of muons from  $D$  hadron decays, for the central (solid line) and boundary (dashed lines) values of  $\epsilon_c$ . (Bottom left and right): ratios of these distributions and the fits used to weigh Monte Carlo events to calculate systematic errors.

## 6.10 Systematic Errors

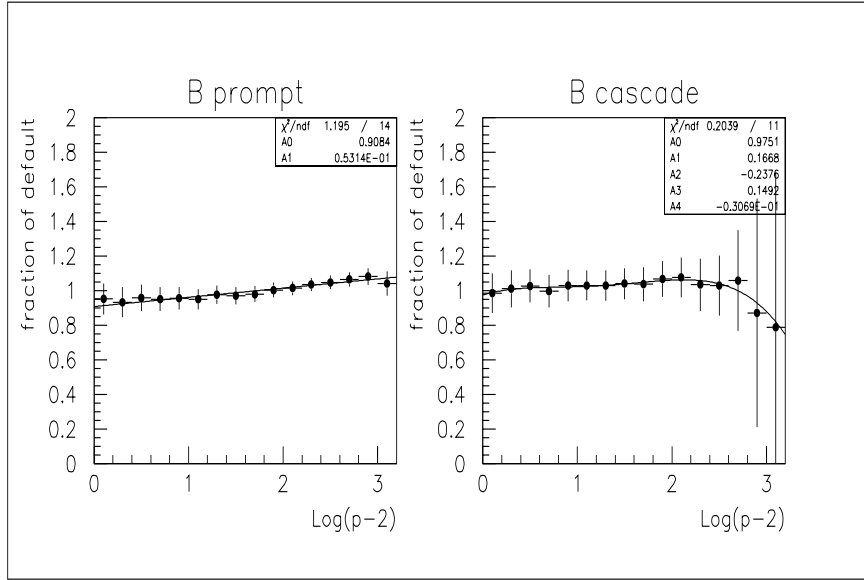


**Figure 6.31:** Ratios of the momentum distributions of primary (left) and secondary (right) muons from simulations with the standard Peterson and the phenomenological Aleph functions.

function and the ALEPH function. The ratio of these distributions, together with the fit used to evaluate the systematic error are shown in fig. 6.31. Muons in the Monte Carlo have been reweighted according to these fits as a function of the track total momentum and decay source. The corresponding variations in  $A_b$  and  $A_c$  are:  $\Delta A_b = 0.0018$  and  $\Delta A_c = 0.0026$ .

### 6.10.11 $B$ tag systematic error

A  $B$  tag calibration has been done, (as described in section 6.6), by correcting the Monte Carlo flavour composition according to the data in the low and high mass regions separately. For this purpose, we have calculated a set of efficiencies for  $b\bar{b}$ ,  $c\bar{c}$  and light quark events to be tagged as  $b\bar{b}$  or  $c\bar{c}$  in each of these regions as a function of  $|\cos\theta|$ . Uncertainties on the quantities used to calculate  $\epsilon_b$ ,  $\epsilon_c$  and  $\epsilon_{uds}$  (mainly due

## 6.10 Systematic Errors

---

to MC statistics or taken from  $R_b$  analysis measurements) are propagated to give the errors on these efficiencies. After calculating the shifts in the central values of  $A_b$  and  $A_c$  corresponding to the 1-sigma boundary values of the efficiencies, we have conservatively assumed as systematic error on the  $B$  tag calibration the sum in quadrature of all the 12 different variations, which yields:  $\Delta A_b = 0.0104$  and  $\Delta A_c = 0.0495$ .

### 6.10.12 L/D systematic errors

One of the systematic errors connected to the L/D variable is due to the uncertainty on the branching ratio of  $B \rightarrow D\bar{D}$  decays. The latest SLD inclusive measurement for the channel is  $(16.2 \pm 1.9)\%$  [112]. To extract the contribution from cascade semileptonic decays we have combined the measured exclusive states from ALEPH [113] ( $B \rightarrow D^0 D^+ X$ ,  $B \rightarrow D^0 D_s X$ ,  $B \rightarrow D^0 \bar{D}^0$  etc.) with the respective  $D$  semileptonic branching ratios from the PDG [7], and summed up to obtain  $BR(b \rightarrow D\bar{D}X \rightarrow l) = (7.3 \pm 1.5)\%$ . The fraction in our Monte Carlo is different according to the run period: the variations assumed are  $(11.5 \pm 2.5)\%$  for 1996-1998 and  $(7.5 \pm 1.5)\%$  for 1993-1995. The L/D weights have been recalculated for the boundary values of this branching ratio and the corresponding shift in the central values of  $A_b$  and  $A_c$  has been taken as a systematic error:  $\Delta A_b = 0.0086$  and  $\Delta A_c = 0.0022$ .

Another source of uncertainty on L/D could be the difference in lifetime between  $D^\pm$  and  $D^0$  mesons in  $b$  cascade events, related to the uncertainty on the  $B \rightarrow D^\pm \rightarrow \mu$  and  $B \rightarrow D^0 \rightarrow \mu$  relative branching ratios ( $\tau_{D^\pm} = 1.061$  ps,  $\tau_{D^0} = 0.413$  ps). Combining

## 6.10 Systematic Errors

---

the latest ALEPH measurements on charm production in  $b$  decays [114] with the PDG [7] semileptonic branching ratios of charmed mesons, one gets that the fraction of  $b$  cascade decays occurring via a  $D^\pm$  is approximately  $(40 \pm 5)\%$  and the fraction of those occurring via a  $D^0$  is  $\sim (38 \pm 5)\%$ . In order to estimate the systematic error, we have conservatively assumed an uncertainty of about twice the absolute error on these fractions (10%) and we have recalculated the L/D weights after increasing one fraction at a time (at the expense of the other). We have then taken the average of the variations found in the two cases:  $\Delta A_b = 0.0015$  and  $\Delta A_c = 0.0024$ .

Finally, a third systematic error has been evaluated by fitting the data to Monte Carlo ratio of the L/D distributions to a polynomial function and by rescaling the value of L/D in each event in the data according to this fit (before applying the weights). The shifts in the central values of  $A_b$  and  $A_c$  are:  $\Delta A_b = 0.0037$  and  $\Delta A_c = 0.0062$ .

### 6.10.13 Polarization

The year-by-year values of the luminosity-weighted average polarization have been summarised in table 3.2. Systematic errors have been calculated by varying the event polarization value by the statistical uncertainty relevant for each period (1993-1995, 1996 or 1997-1998). This shifts the central values of  $A_b$  and  $A_c$  by:  $\Delta A_b = 0.0048$  and  $\Delta A_c = 0.0029$ .

## 6.10 Systematic Errors

---

### 6.10.14 $B$ mixing

The error due to the uncertainty on the measurement of  $\bar{\chi}$  ( $0.1186 \pm 0.0043$ ) [15] is calculated by rescaling the  $\chi$  distribution (fig. 6.9) so as to shift its average by the corresponding relative amount in both directions. The only measurement affected is  $A_b$ , which varies by:  $\Delta A_b = 0.0105$ .

### 6.10.15 Second order QCD corrections and QCD systematic errors

Second order QCD corrections to the polarized forward-backward asymmetry are related to two effects: second order hard gluon radiation and *gluon splitting* [115].

The error due to the second term depends on the event selection through a multiplicative factor which is zero if all the events with gluon splitting are excluded from the analysis. Since this effect is included in JETSET, a conservative way to estimate the relative uncertainty is to eliminate from the analysis (run on Monte Carlo events) muons coming from these types of processes and recalculate the parameters  $A_b$  and  $A_c$ . The size of the correction, rescaled to account for the difference between the values of the splitting rates in JETSET and their world average values [15], has been used to shift the central values of  $A_b$  and  $A_c$ . The systematic errors are derived from the effect of the statistical uncertainty on the splitting rates and amount to:  $\Delta A_b = 0.0016$  and  $\Delta A_c = 0.0017$ .

For the  $O(\alpha_s^2)$  hard gluon radiation effects we have recently implemented new theoretical calculations by Ravindran and van Neerven [25]. These have been worked out for different values of the quark masses (pole masses and running) and predicted effects are about four times as big as in previous calculations [116] ( $\sim 1\%$  correction on  $A_b$  as opposed to

## 6.10 Systematic Errors

---

$\sim 0.3\%$ ). Defining

$$\tilde{A}_{FB}^f(Q^2) = (\tilde{A}_{FB}^f(Q^2))_0 \left\{ 1 - c_1 \frac{\alpha_s(\mu)}{\pi} - c_2 \left( \frac{\alpha_s(\mu)}{\pi} \right)^2 \right\}, \quad (6.25)$$

the values of the second order coefficients have been calculated to be  $c_2^b = 8.89$  and  $c_2^c = 11.5$  for  $b$  and  $c$  quarks respectively (for pole masses). These have been rescaled in the analysis by the mitigation factor calculated in section 6.4.2 and the central values of  $A_b$  and  $A_c$  have been shifted by the value of the correction ( $\delta A_b \simeq 0.011$ ,  $\delta A_c \simeq 0.008$ ). The systematic error on this term has been calculated by using the coefficients  $c_2^b$  and  $c_2^c$  corresponding to the running masses of the  $b$  and  $c$  quarks and assuming the variation in the correction as our uncertainty.

Other contributions to the QCD systematic error come from uncertainties on the first order correction, which arise from: i) uncertainty on the knowledge of  $\alpha_s$ ; ii) MC statistics in the calculation of the mitigation factors; iii) the choice of models of gluon radiation and hadronization; iv) uncertainty on the quark masses (difference between the use of running masses and pole masses). For case i)  $\alpha_s$  has been conservatively varied by twice the current world average error [7] ( $\pm 0.004$ ). For case iii) we have considered the difference between JETSET and Stav-Olsen in the treatment of first order QCD corrections, and also the difference between the JETSET first order Matrix Element and the Parton Shower model approaches. These have been found to account for a 30% and a 10% relative error on the size of the bias correction respectively.

All the contributions to the QCD systematic uncertainty have been summed up in quadrature to yield the total error:  $\Delta A_b = 0.0053$  and  $\Delta A_c = 0.0048$ .

## 6.11 Final results

After applying all these corrections, the final results and their errors are then:

$$A_b = 0.963 \pm 0.084(stat) \pm 0.029(syst) \quad (6.26)$$

$$A_c = 0.557 \pm 0.110(stat) \pm 0.068(syst)$$

for 1993-1995,

$$A_b = 1.016 \pm 0.118(stat) \pm 0.038(syst) \quad (6.27)$$

$$A_c = 0.666 \pm 0.171(stat) \pm 0.077(syst)$$

for 1996, and

$$A_b = 0.927 \pm 0.047(stat) \pm 0.023(syst) \quad (6.28)$$

$$A_c = 0.544 \pm 0.068(stat) \pm 0.064(syst)$$

for 1997-1998. A combination of these measurements is then calculated along with the errors using the technique BLUE [117], via the construction of a covariance matrix. Correlation between systematic errors of the measurements to be averaged is taken into account in the combination of the results (see the next paragraph for more details). The combined results are then:

$$A_b = 0.942 \pm 0.039(stat) \pm 0.024(syst) \quad (6.29)$$

$$A_c = 0.559 \pm 0.055(stat) \pm 0.061(syst)$$

and the detailed lists of contributions to the systematic errors are shown in tables 6.5 and 6.6.

## 6.11 Final results

<i>Source</i>	<i>Variations adopted</i>	(1993 – 1995)	(1996)	(1997 – 8)	<i>combined</i>
Monte Carlo stat.	4 MC subsamples	.0065	.0186	.0045	.0038
Tracking eff.	MC/DT trk mult.	.0064	.0111	.0072	.0074
Jet axis sim.	10 mrad smear.	.0023	.0025	.0018	.0020
Bkg level	$\pm 10\%$	.0079	.0057	.0028	.0041
Bkg asymmetry	DT/MC ratio	.0030	.0006	.0020	.0021
BR( $Z^0 \rightarrow b\bar{b}$ )	(21.64 $\pm$ .07)%	.0005	.0003	.0004	.0004
BR( $Z^0 \rightarrow c\bar{c}$ )	(16.74 $\pm$ .38)%	.0010	.0008	.0007	.0008
BR( $b \rightarrow \mu^-$ )	(10.62 $\pm$ .17)%	.0043	.0048	.0027	.0032
BR( $b \rightarrow c \rightarrow \mu^+$ )	(8.07 $\pm$ .25)%	.0052	.0059	.0033	.0039
BR( $b \rightarrow \bar{c} \rightarrow \mu^-$ )	(1.62 $\pm$ .40)%	.0024	.0024	.0064	.0052
BR( $b \rightarrow \tau \rightarrow \mu^-$ )	(0.452 $\pm$ .074)%	.0004	.0025	.0033	.0026
BR( $b \rightarrow J/\psi \rightarrow \mu^\pm$ )	(0.07 $\pm$ .02)%	.0029	.0023	.0029	.0028
BR( $c \rightarrow \mu^+$ )	(9.85 $\pm$ .32)%	.0020	.0010	.0010	.0012
$B \rightarrow D^{**}\mu\nu$ frac.	$\pm 10\%$	.0038	.0025	.0032	.0033
$D$ lept. spect.	$ACCM1_{-3}^{+2}$	.0048	.0038	.0040	.0042
$B_s$ fraction	.115 $\pm$ .050	.0030	.0031	.0006	.0013
$\Lambda_b$ frac.	.072 $\pm$ .030	.0023	.0028	.0015	.0018
$b,c$ frag.	see text	.0034	.0033	.0027	.0029
Aleph frag.	reweighting	.0030	.0063	.0008	.0018
Polarization	$P = 0.729 \pm .0038$	.0050	.0064	.0045	.0048
2 <sup>nd</sup> order QCD	$\Delta_{QCD}$ uncert.	.0050	.0057	.0053	.0053
gluon splitt.	$g_{b\bar{b}}, g_{c\bar{c}}$ uncert.	.0039	.0029	.0008	.0016
$B$ mixing	$\bar{\chi} = .1186 \pm .0043$	.0106	.0114	.0104	.0105
$D^0/D^\pm$	15% uncert.	.0000	.0041	.0016	.0015
$B$ tag	<i>eff. calib.</i>	.0163	.0175	.0077	.0104
L/D	DT/MC ratio	.0082	.0048	.0022	.0037
$B \rightarrow D\bar{D}$	see text	.0026	.0156	.0094	.0086
Total		.0285	0.0384	0.0227	0.0239

Table 6.5: Systematic errors on the  $A_b$  measurements.

## 6.11 Final results

<i>Source</i>	<i>Variations adopted</i>	(1993 – 1995)	(1996)	(1997 – 8)	<i>combined</i>
Monte Carlo stat.	4 MC subsamples	.0340	.0327	.0263	.0194
Tracking eff.	MC/DT trk mult.	.0036	.0021	.0031	.0031
Jet axis sim.	10 mrad smear.	.0020	.0019	.0016	.0017
Bkg level	$\pm 10\%$	.0228	.0222	.0076	.0130
Bkg asymmetry	DT/MC ratio	.0135	.0082	.0072	.0090
BR( $Z^0 \rightarrow b\bar{b}$ )	$(21.64 \pm .07)\%$	.0007	.0006	.0006	.0006
BR( $Z^0 \rightarrow c\bar{c}$ )	$(16.74 \pm .38)\%$	.0098	.0106	.0076	.0085
BR( $b \rightarrow \mu^-$ )	$(10.62 \pm .17)\%$	.0040	.0038	.0033	.0035
BR( $b \rightarrow c \rightarrow \mu^+$ )	$(8.07 \pm .25)\%$	.0053	.0031	.0034	.0039
BR( $b \rightarrow \bar{c} \rightarrow \mu^-$ )	$(1.62 \pm .40)\%$	.0138	.0100	.0112	.0118
BR( $b \rightarrow \tau \rightarrow \mu^-$ )	$(0.452 \pm .074)\%$	.0026	.0028	.0024	.0025
BR( $b \rightarrow J/\psi \rightarrow \mu^\pm$ )	$(0.07 \pm .02)\%$	.0005	.0004	.0004	.0004
BR( $c \rightarrow \mu^+$ )	$(9.85 \pm .32)\%$	.0206	.0148	.0107	.0137
$B \rightarrow D^{**}\mu\nu$ frac.	$\pm 10\%$	.0077	.0010	.0006	.0025
$D$ lept. spect.	$ACCM1_{-3}^{+2}$	.0018	.0075	.0007	.0016
$B_s$ fraction	$.115 \pm .050$	.0016	.0020	.0013	.0014
$\Lambda_b$ frac.	$.072 \pm .030$	.0016	.0010	.0010	.0011
$b,c$ frag.	see text	.0137	.0134	.0114	.0122
Aleph frag.	reweighting	.0037	.0027	.0021	.0026
Polarization	$P = 0.729 \pm .0038$	.0030	.0043	.0027	.0029
2 <sup>nd</sup> order QCD	$\Delta_{QCD}$ uncert.	.0030	.0060	.0054	.0048
gluon splitt.	$g_{b\bar{b}}, g_{c\bar{c}}$ uncert.	.0017	.0047	.0013	.0017
$B$ mixing	$\bar{\chi} = .1186 \pm .0043$	.0000	.0000	.0000	.0000
$D^0/D^\pm$	15% uncert.	.0000	.0057	.0029	.0024
$B$ tag	<i>eff. calib.</i>	.0398	.0571	.0523	.0495
L/D	DT/MC ratio	.0104	.0044	.0048	.0062
$B \rightarrow D\bar{D}$	see text	.0000	.0120	.0016	.0022
Total		.0680	0.0767	0.0639	0.0614

Table 6.6: Systematic errors on the  $A_c$  measurements.

# Chapter 7

## Conclusions

In conclusion, we have presented a measurement of the extent of parity violation in the coupling of  $Z^0$  bosons to  $b$  quarks by using identified charged muons from semileptonic decays. As a secondary result, we gave an estimate of  $A_c$  from the same data fit.

The analysis here presented is based on the full 1993-1998 SLD data sample of 550K  $Z^0$  decays produced with polarized  $e^-$  beams, and employs a new method of discrimination between bottom, charm and light quarks which incorporates vertexing information and therefore benefits from the excellent resolution of the SLD vertex detector. The resulting measurements represent a substantial increase in accuracy relative to the results obtained before the upgrade of the analysis. In particular, the precision on the  $A_b$  measurement has improved by a factor of 2 with respect to the previous 1993-1995 published numbers (with no vertexing) [118].

The final result

## Conclusions

---

$$A_b = 0.942 \pm 0.039(stat) \pm 0.024(syst)$$

is consistent with the Standard Model expectations ( $A_b=0.935$  for  $\sin^2 \theta_W = 0.23055$ ). The combined average with the analogous measurement using electrons instead of muons is:

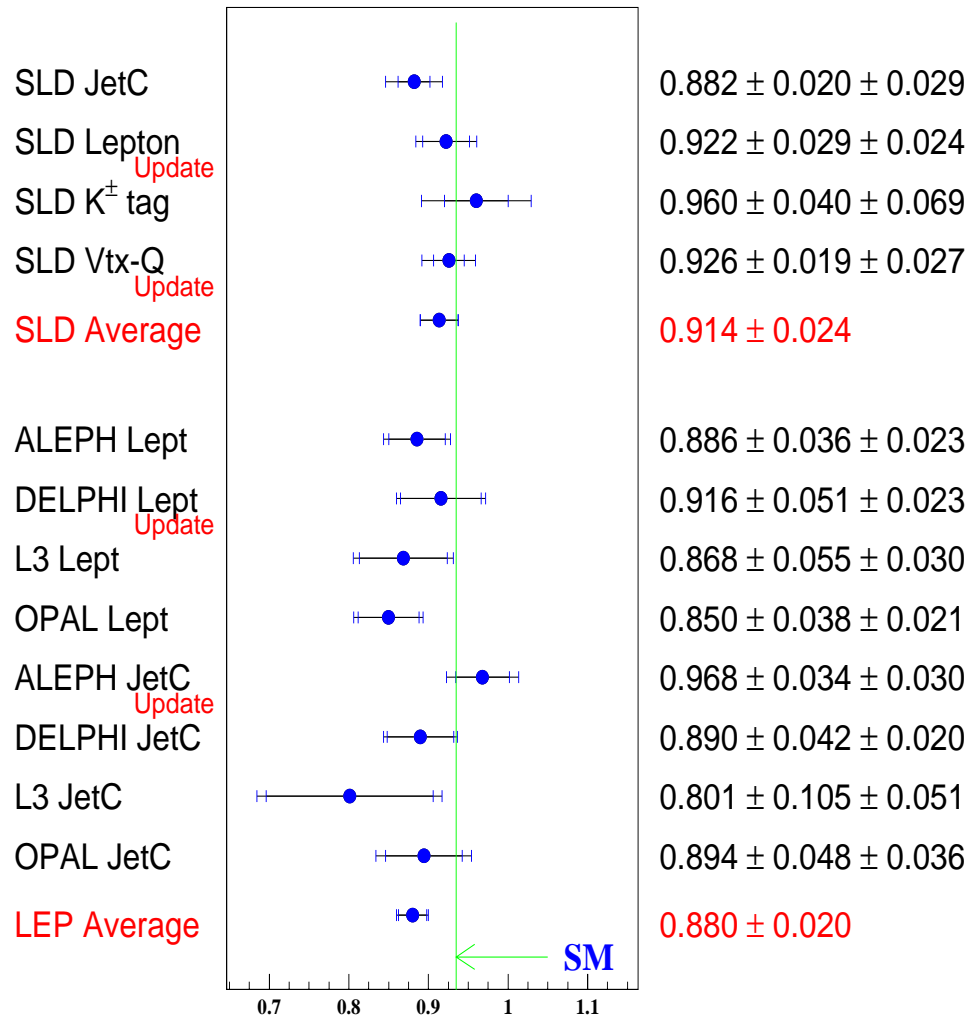
$$A_b = 0.922 \pm 0.029(stat) \pm 0.024(syst).$$

The full list of current measurements (as of the summer 2000 conferences) of  $A_b$  is presented in fig. 7.1. Shown are the 4 direct SLD measurements, obtained with the techniques described in chapter 2. These results have been combined taking into account statistical and systematic correlations. The statistical overlap was determined by explicitly tabulating events for a subset of the data and by considering the overlapping event fractions, the fractions of events where different tags assigned the same quark directions and the event weights, based on  $b$ -hadron purity, correct-sign probability and polar angle reconstruction. The statistical correlations extracted range from  $\sim 10 - 30\%$ . Muon-electron correlation is set to zero [119].

Correlations between analyses due to common systematic errors have been treated with the method developed by the LEP Electroweak Working Group [120]. The analyses are then combined in a weighted average using the individual analysis errors and the statistical correlation matrix. Each analysis receives a weight based on its statistical and uncorrelated systematic error.

The SLD combined average ( $0.914 \pm 0.024$ ) is consistent with the SM prediction (within  $\sim 1 \sigma$ ).

## $A_b$ Measurements (Summer-2000)



LEP Measurements:  $A_b = 4 A^{0,b_{FB}} / 3 A_e$   
 Using  $A_e = 0.1500 \pm 0.0016$  (Combine SLD  $A_{LR}$  and LEP  $A_l$ )

Figure 7.1: Current world measurements of  $A_b$  [122].

## Conclusions

---

The LEP measurements presented here are not the published ones, since what it is possible to measure at LEP is the unpolarized forward-backward asymmetry, hence only the product  $A_e A_b$ . The numbers shown here have therefore been extracted from the LEP measurements by assuming for  $A_e$  a value equal to the current combination of the SLD  $A_{LR}$  result and the LEP  $A_l$  measurements:  $A_e = 0.1500 \pm 0.0016$  [15]. The LEP average ( $0.880 \pm 0.020$ ) is consistent with the SLD result.

When taking the SLD+LEP average combination ( $A_b = 0.898 \pm 0.015$ ), though, the result is around  $2.5 \sigma$  below the SM expectation. A graphical representation of these results is shown in a TGR plane (after Takeuchi, Grant and Rosner [121]) in fig. 7.2. Plotted on the axes are  $\delta \sin^2 \theta_W$  and  $\delta \zeta_b$ , which express the dependence on oblique and non-oblique corrections respectively at the  $Z^0 \rightarrow b\bar{b}$  vertex. The three  $1\sigma$ -bands represent the 3 measurements of SLD  $A_b$ , LEP  $A_{FB}^b$  and SLD  $A_{LR}$  + LEP  $A_l$ , and shown are the 68% and 95% confidence level ellipses of their combined fit. The origin of the plot gives the SM expectation value and the red line represents the change in this value corresponding to different assumptions on the top quark and Higgs mass. The current best fit overlaps with SM predictions at the boundary of the 95% confidence region.

There has been speculation on the conclusions to draw from this picture, in the perspective that, if there is something new affecting the  $A_b$  measurement, this could also explain another puzzle, i.e. the  $3.2 \sigma$  difference between the purely leptonic and the hadronic measurements of  $\sin^2 \theta_W$  (see fig. 7.3). There are several possible explanations to the problem:

- the deviations could be simply the result of statistical fluctuations;

## Conclusions

---

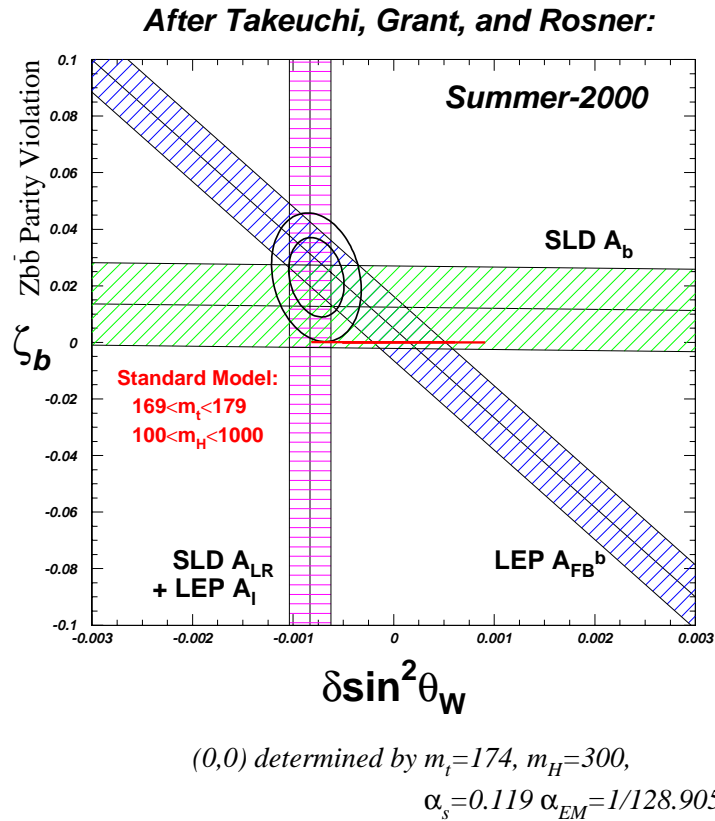


**Figure 7.2:** Measurements of  $A_l$ ,  $A_b$ ,  $A_{FB}^b$  are plotted in the  $\delta \sin^2 \theta_W$ - $\delta \zeta_b$  plane. The SM prediction appears as a horizontal line and the best fit to the data is shown as concentric 68% and 95% ellipses [123].

### SLD-LEP Weak Mixing Angle Results

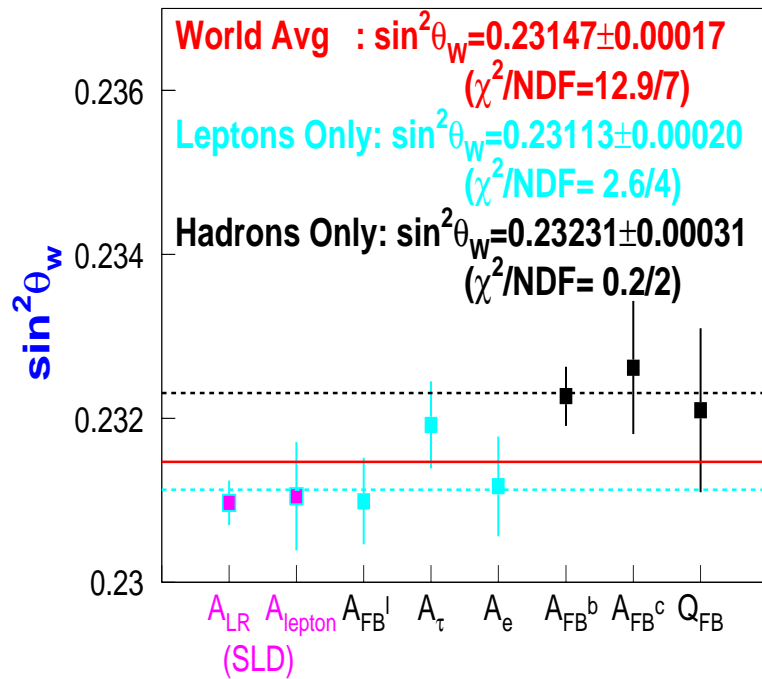


**Figure 7.3:** Current world measurements of  $\sin^2\theta_W$ . Hadronic measurements ( $A_{FB}^b$ ,  $A_{FB}^c$ ,  $Q_{FB}$ ) tend to be higher than the SM value, whereas purely leptonic ones ( $A_{FB}^l$ ,  $A_e$ ,  $A_l$ ) are slightly lower [124].

## Conclusions

---

- unknown systematic effects could be distorting some or all of the results;
- we could be seeing evidence of new physics.

The second case has been examined in a recent study by J. H. Field [125]. He first points out how the individual measurements show quite good internal consistency, and how, even excluding the most outlying ones (the ALEPH jet charge and the OPAL leptons), the deviation only changes within  $-2.9 < \sigma < -1.7$ . If only the most accurate measurements of each observable are used, the deviation observed is around  $-2.5 \sigma$ , whereas, using all the remaining measurements, it goes down to  $-0.82 \sigma$ . This could be a hint that the systematic errors of the most precise measurements have been underestimated, leading to an overestimation of the deviation from the SM. The LEP average value is statistics dominated, and its systematic error is about 50% correlated. In contrast, the SLD statistical and systematic error are roughly equal and the correlated component of the systematic error is relatively small. Even by applying a factor of 1.5 or 1/1.5 to the global systematic error, no dramatic effect on the significance of the deviation is observed.

In the third case, the possibility that new physics at a higher energy scale might be affecting the  $Z^0 \rightarrow b\bar{b}$  couplings has been studied in different scenarios. Experimental constraints are however quite difficult to accommodate by any new proposed model. The lepton sector, in particular, seems to be mostly consistent with the SM as well as  $R_b$ , which is proportional to the sum  $\{(g_L^b)^2 + (g_R^b)^2\}$ . Any deviation on the right-handed coupling  $g_R^b$  (the one  $A_b$  is most sensitive to) would therefore imply a similar and opposite deviation on the left-handed one:  $(\delta g_L^b)^2 \simeq -(\delta g_R^b)^2$ .

## Conclusions

---

One of the possible models [126] postulates the existence of anomalous right-handed currents in the  $Z^0 \rightarrow b\bar{b}$  vertex, related to an extended gauge group  $SU(2)_L \times SU(2)_R \times U(1)$ . Additional contributions to the neutral current sector would come from the interaction with an extra neutral gauge boson  $Z'$  and from the interaction with the ordinary  $Z$  boson, being suppressed by the mixing angle  $\xi$  between  $Z$  and  $Z'$ . In this model corrections to the  $Z \rightarrow b\bar{b}$  vertex would have the form  $\bar{u}(\Delta_b^L \gamma_\mu P_L + \Delta_b^R \gamma_\mu P_R)u$ , where  $\Delta_b^R = 0$  in the SM picture. Two parameters  $\epsilon_b$  and  $\epsilon_b'$  can be defined, the first of which comprises top quark mass dependent corrections in the SM, while the second measures the anomalous right-handed current interaction and goes to 0 in the SM limit. By rewriting the  $\Gamma_b$  and  $A_{FB}^b$  observables as a function of these parameters, and by fitting to the current LEP+SLD data, it is possible to find an allowed region of  $\epsilon_b$  and  $\epsilon_b'$  at 95% confidence level.

In a recent work, M. Chanowitz [127] finds that it could be possible to accommodate all measurements by changing both the left- and the right-handed  $b$  neutral couplings. However, there would be consequences on the flavour-changing neutral currents, with enhanced  $Z$  penguin amplitudes in rare  $K$  and  $B$  decays (such as  $K^+ \rightarrow \pi^+ \nu \bar{\nu}$ ,  $K_L \rightarrow \pi^0 \nu \bar{\nu}$ ,  $B \rightarrow X_s \nu \bar{\nu}$ ,  $B_s \rightarrow \mu \bar{\mu}$ ), which could only be probed in the future at  $B$  factories (BaBar [128], LHCb [129], BTeV [130]) or experiments such as KTeV [131].

In support of the first scenario there is the fact that, although interesting and possibly suggestive of new physics, the deviation in  $A_b$  is still of only marginal statistical significance. However, since the full LEP and SLD  $Z^0$  pole data have essentially been already analyzed, no further light will be shed unless a future linear collider [132] is ap-

## Conclusions

---

proved. If a short period of running at the  $Z^0$  pole is to be scheduled (as it has been proposed by both the European and the American working groups), at a luminosity of  $\mathcal{L} \sim 5 \times 10^{33} \text{ cm}^{-2}\text{s}^{-1}$ , a *Linear Collider Z Factory* could collect a sample of  $10^9$   $Z^0$  decays in only 70 days (i.e.  $100\times$  the LEP1 data sample or  $2000\times$  the SLD one). Assuming that both the electron and the positron beams can be polarized, with  $\mathcal{P}_{e^+} = \pm 60\%$  and  $\mathcal{P}_{e^-} = \pm 80\%$ , (corresponding to an effective polarization of  $\sim 95\%$ ) [133], the analysis will be  $25\%$  more sensitive to  $A_b$  than the current one. Better  $b$ -tagging will significantly improve the precision of techniques such as the vertex-charge method, but even just the extrapolation of the two main LEP methods (leptons and jet-charge) shows that a statistical error of  $\Delta A_b = 4 \cdot 10^{-4}$  could be achieved, and that a total error of  $\Delta A_b \sim 10^{-3}$  could be possible. Since a similar improvement could also be obtainable on  $A_e$ , a combined projection on the precision attainable on these measurements is summarized by fig. 7.4 [133]. A more stringent test of the Standard Model would therefore be possible, and any hint of new physics could be definitely confirmed or discarded.

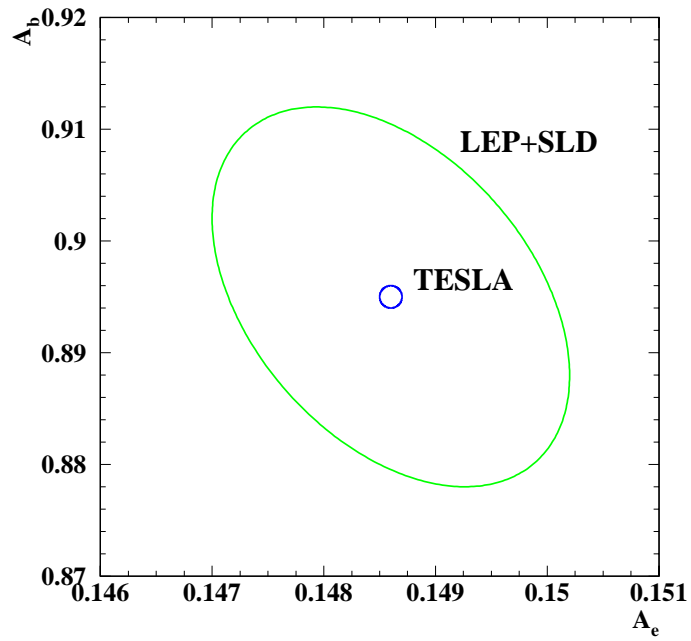


**Figure 7.4:**  $A_b$  vs  $A_e$  from the current LEP and SLD electroweak data, compared to the expectation for the TESLA  $Z^0$  factory running. Taken from [133].

# Bibliography

- [1] E. Fermi, *Nuovo Cim.* **11**, 1-19 (1934).  
E. Fermi, *Z. Phys.* **88**, 161-177 (1934).
- [2] T. D. Lee and C. N. Yang, *Phys. Rev.* **104**, 254 (1956).
- [3] C. N. Yang and R. L. Mills, *Phys. Rev.* **96**, 191 (1954).
- [4] S. L. Glashow, *Nucl. Phys.* **22**, 579 (1961).
- [5] S. Weinberg, *Phys. Rev. Lett.* **19**, 1264 (1967).
- [6] A. Salam, in “Elementary particle theory”, ed. N. Svartholm, Stockholm, p.367.
- [7] D. E. Groom *et al.*, *Eur. Phys. J.* **C15**, 1 (2000).
- [8] J. E. Augustin *et al.*, *Phys. Rev. Lett.* **33**, 1406 (1974).  
J. J. Aubert *et al.*, *Phys. Rev. Lett.* **33**, 1404 (1974).
- [9] M. Perl *et al.*, *Phys. Rev. Lett.* **35**, 1489 (1975).
- [10] W. R. Innes *et al.*, *Phys. Rev. Lett.* **39**, 1240 (1977).
- [11] F. Abe *et al.*, CDF Collaboration, *Phys. Rev. Lett.* **74**, 2626 (1995).  
S. Abachi *et al.*, D0 Collaboration, *Phys. Rev. Lett.* **74**, 2632 (1995).
- [12] G. Arnison *et al.*, UA1 Collaboration, *Phys. Lett.* **B134**, 469 (1984).
- [13] G. Arnison *et al.*, UA1 Collaboration, *Phys. Lett.* **B126**, 398 (1983).
- [14] F. Halzen and A. D. Martin, “Quarks and leptons: an introductory course in modern particle physics”, Wiley (1984).
- [15] The LEP and SLD Collaborations, “A combination of preliminary electroweak measurements and constraints on the Standard Model”, CERN-EP-2000-016 (2000).
- [16] The LEP and SLD Collaborations, “Combined results on  $b$ -hadron production rates, lifetimes, oscillations and semileptonic decays”, SLAC-PUB-8492 (2000).
- [17] D. Muller, “Recent QCD results at SLD”, talk given at the QCD99 conference, Montpellier, France (1999).

BIBLIOGRAPHY

---

- [18] K. Abe *et al.*, Phys. Rev. Lett. **84**, 5945 (2000).
- [19] D. C. Kennedy, J. M. Im, B. W. Lynn and R. G. Stuart, SLAC-PUB-4128 (1988).
- [20] B. W. Lynn, M. E. Peskin and R. G. Stuart, SLAC-PUB-3725 (1985).
- [21] M. E. Peskin and T. Takeuchi, Phys. Rev. **D46**, 381 (1992).
- [22] A. Blondel, B. W. Linn, F. M. Renard, C. Verzegnassi, Nucl. Phys. **B304**, 438 (1988).
- [23] F. M. Renard, A. Blondel and C. Verzegnassi, "QED and QCD effects in polarized forward-backward asymmetries", in "Polarization at LEP", CERN-88/06 Vol.1 (1988).
- [24] J. Stav and H. Olsen, Phys. Rev. **D52,3**, 1359 (1995),  
J. Stav and H. Olsen, Phys. Rev. **D54,1**, 817 (1996)
- [25] V. Ravindran and W. L. van Neerven, Phys. Lett. **B445**, 214 (1998)
- [26] B. Holdom, Phys. Lett. **B339**, 114 (1994),  
J. Erler and P. Langacker, Phys. Rev. Lett. **84**, 212 (2000).
- [27] H. E. Haber and G. L. Kane, Phys. Rept. **117**, 75 (1985).
- [28] M. Boulware and D. Finnell, Phys. Rev. **D44**, 2054 (1991)
- [29] T. G. Rizzo, SLAC-PUB-6672 (1994).
- [30] K. Abe *et al.*, SLAC-PUB-7886 (1997).
- [31] T. R. Wright, SLD Analysis Note, March 2000.
- [32] K. Abe *et al.*, SLAC-PUB-8200 (1999).
- [33] K. Abe *et al.*, SLAC-PUB-8447 (2000) submitted to Phys. Rev.
- [34] K. Abe *et al.*, SLAC-PUB-8199 (1999).
- [35] SLAC Linear Collider Conceptual Design Report, SLAC-R-229 (1980). K. Abe *et al.*, Phys. Rev. Lett. **73**, 25 (1994).
- [36] R. Alley *et al.*, Nucl. Instr. & Meth. **A365**, 1 (1995).
- [37] C. Simopoulos and R. L. Holtzapple, SLAC-PUB-6813 (1995)
- [38] C. Adolphsen *et al.*, SLAC-PUB-6118 (1993)
- [39] J. E. Clendenin, SLAC-PUB-4743 (1989),  
R. Pitthan *et al.*, Particle Acceler. Conf., IEEE 1991:2098.
- [40] R. Jacobsen *et al.*, SLAC-PUB-5205 (1990)
- [41] W. Heitler, "The Quantum Theory of Radiation", 3<sup>rd</sup> ed., p.264-267, Clarendon Press, Oxford.

**BIBLIOGRAPHY**

---

- [42] R. Erickson, SLAC-PUB-4479 (1987)
- [43] P. Raimondi *et al.*, SLAC-PUB-7955 (1998).
- [44] T. Maruyama *et al.*, Phys. Rev. Lett. **66**, 2376 (1991).
- [45] T. Limberg, P. Emma, R. Rossmanith, IEEE PAC 1993:429 (1993).
- [46] D. Calloway *et al.*, SLAC-PUB-6423 (1994).
- [47] P. Reinertsen *et al.*, SLAC-PUB-8029 (1998).
- [48] G. Blaylock *et al.*, SLAC-PUB-5649 (1992).
- [49] SLD Design Report, SLAC-REPORT-273 (1984).
- [50] G. Agnew *et al.*, SLAC-PUB-5906 (1992).
- [51] S. Hedges *et al.*, SLAC-PUB-6950 (1995).  
C. J. S. Damerell *et al.*, Nucl. Instr. & Meth. **A400**, 287 (1997).
- [52] T. Abe, Contributed paper at 8<sup>th</sup> International Workshop on Vertex Detectors, VERTEX99, Texel, Netherlands, SLAC-PUB-8239 (1999).
- [53] M. Hildreth *et al.*, Nucl. Instr. & Meth. **A367**, 111 (1995).
- [54] D. C. Williams, Ph. D. Thesis, MIT, SLAC-R-445 (1994).
- [55] P. Reinertsen, Ph. D. Thesis, University of California Santa Cruz, SLAC-R-537 (1999).
- [56] D. Aston *et al.*, Nucl. Instr. & Meth. **A283**, 582 (1989).
- [57] D. Dong, Ph. D. Thesis, MIT, SLAC-R-550 (1999).
- [58] H. Staengle, Ph. D. Thesis, Colorado State University, SLAC-R-549 (1999).
- [59] D. Axen *et al.*, Nucl. Instr. & Meth. **A328**, 472 (1993).
- [60] E. Vella *et al.*, SLAC-PUB-5953 (1992).
- [61] A. Benvenuti *et al.*, Nucl. Instr. & Meth. **A290**, 353 (1990).
- [62] A. Benvenuti *et al.*, SLAC-PUB-5332 (1990).
- [63] S. C. Berridge *et al.*, IEEE Trans. Nucl. Sci. **37**, 1191 (1990).
- [64] K. Pitts, Ph. D. Thesis, Oregon University, SLAC-R-446 (1994).
- [65] D. Sherden, Nucl. Instr. & Meth. **A265**, 342 (1988).
- [66] T. Sjöstrand, CERN-TH-7112-93, 1994.
- [67] T. Sjöstrand, Computer Phys. Commun. **43**, 367 (1987)
- [68] P. N. Burrows and H. Masuda, SLD Physics Note 36 (1995).

BIBLIOGRAPHY

---

- [69] C. Peterson, D. Schlatter, I. Schmitt and P.M. Zerwas, Phys. Rev. **D27**, 105 (1983)
- [70] ALEPH Collab., “Heavy flavour physics with leptons”, contributed to ICHEP92, Dallas, Texas (1992).
- [71] D. Buskulic *et al.*, Z. Phys. **62**, 1 (1994).
- [72] N. Isgur, D. Scora, B. Grinstein and M. B. Wise, Phys. Rev. **D39**, 799 (1989)
- [73] T. R. Junk, Ph. D. Thesis, SLAC, SLAC-R-276 (1995).
- [74] H. Albrecht *et al.*, (ARGUS Collaboration), Z. Phys. **58**, 191 (1993),  
H. Albrecht *et al.*, (ARGUS Collaboration), Z. Phys. **54**, 13 (1992).
- [75] M. Thulasidas, Ph. D. Thesis, Syracuse University (1993).
- [76] GEANT program, version 3.21, CERN Application Software Group, CERN Program Library (1993). See R. Brun *et al.*, GEANT3 User’s Guide, CERN-DD/EE/84-1, CERN (1989).
- [77] W. Ralph Nelson, H. Hirayama, D. W. O. Rogers, SLAC-R-265 (1985).
- [78] H. fesefeldt, GEISHA, PITHA 85/02 (1985).
- [79] F. A. Berends, Nucl. Phys. **B253**, 441 (1985).
- [80] S. Gonzalez Martirena, Ph. D. Thesis, MIT, SLAC-R-439 p.104 (1994).
- [81] R. D. Elia, Ph. D. Thesis, SLAC , SLAC-R-429 p.100-103(1994).
- [82] J. M. Yamartino, Ph. D. Thesis, MIT, SLAC-R-426 p.61-63 (1994).
- [83] K. Abe *et al.*, SLAC-PUB-8225 (1999).
- [84] D. Jackson, Nucl. Instr. & Meth. **A388**, 247 (1997).
- [85] S. Brandt *et al.*, Phys. Lett. **12**, 57 (1964),  
E. Farhi, Phys. Rev. Lett. **39**, 1587 (1977).
- [86] K. Abe *et al.*, Phys. Rev. **D59**, 12002 (1999).
- [87] W. Bartel *et al.*, Z. Phys. **33**, 23 (1986).
- [88] K. Abe *et al.*, Phys. Rev. Lett. **80**, 660 (1998).
- [89] P. Billoir, Nucl. Instr. & Meth. **A225**, 352 (1984).
- [90] D. J. Jackson, reported at the International Europhysics Conference on High Energy Physics, Tampere, Finland, July 15-21, 1999. More detailed discussion can be found in SLAC-PUB-8225.
- [91] G. Mancinelli, “Improved muon identification at SLD”, SLD Physics Note 65 (1998).
- [92] K. Abe *et al.*, Nucl. Instr. & Meth. **A371**, 195 (1996).
- [93] J. A. Quigley, Ph. D. Thesis, MIT, SLAC-R-506 p.65 (1997).

BIBLIOGRAPHY

---

- [94] A. G. Frodesen, O. Skjeggstad, H. Tofte, “Probability and statistics in particle physics”, Universitetsforlaget (1979).
- [95] I. Dunietz, FERMILAB-PUB-96/104-T (1996).
- [96] K. Abe *et al.*, SLD Physics Note 66 (1998).
- [97] T. Abe, private communication.
- [98] D. Bardin *et al.*, CERN-TH-6443-92 (1992).
- [99] J. P. Fernandez, Ph.D. Thesis, University of California Santa Cruz (1999).
- [100] A. Zell *et al.*, SNNS (Stuttgart Neural Network Simulator), <http://www.informatik.uni-stuttgart.de/ipvr/bv/projekte/snns/snns.html>, Institute for Parallel and Distributed High Performance Systems, University of Stuttgart (1990).
- [101] D. Aston, D. Muller and T. Pavel, SLD Physics Note 58 (1997).
- [102] B. Barish *et al.*, Phys. Rev. Lett. **76**, 1570 (1996).  
L. Gibbons *et al.*, PRD **D56**, 3783 (1997).
- [103] W. Bacino *et al.*, Phys. Rev. Lett. **43**, 1073 (1979).
- [104] G. Altarelli *et al.*, Nucl. Phys. **B208**, 365 (1982).
- [105] LEP Heavy Flavour Working Group, LEPHF/94-01 (1994).
- [106] D. Buskulic *et al.*, Phys. Lett. **B361**, 221 (1995).
- [107] R. Barate *et al.*, Eur. Phys. J. **C2**, 197 (1998).
- [108] R. Akers *et al.*, OPAL Collaboration, Z. Phys. **C60**, 601 (1993).
- [109] K. Ackerstaff *et al.*, OPAL Collaboration, Z. Phys. **C74**, 1 (1997).
- [110] K. Abe *et al.*, Phys. Rev. Lett. **84**, 4300 (2000).
- [111] D. Buskulic *et al.*, ALEPH Collaboration, Phys. Lett. **B357**, 699 (1995).
- [112] M. R. Convery, SLD Collaboration, SLAC-PUB-8076 (1999).
- [113] R. Barate *et al.*, Eur. Phys. J. **C4**, 387 (1998).
- [114] D. Buskulic *et al.*, Phys. Lett. **B388**, 648 (1996).
- [115] P. Abreu *et al.*, Phys. Lett. **B405**, 202 (1997).  
R. Barate *et al.*, Phys. Lett. **B434**, 437 (1998).
- [116] G. Altarelli and B. Lampe, Nucl. Phys. **B391**, 3 (1993).
- [117] L. Lyons *et al.*, Nucl. Instr. & Meth. **A270**, 110 (1988).
- [118] K. Abe *et al.*, Phys. Rev. Lett. **83**, 3384 (1999).

**BIBLIOGRAPHY**

---

- [119] K. Abe *et al.*, SLAC-PUB-8211 (1999).
- [120] ALEPH, DELPHI, L3 and OPAL Collaborations, CERN-PPE-96-017 (1996).
- [121] T. Takeuchi *et al.*, FERMILAB-CONF-94/279-T (1994).
- [122] D. Su, private communication.
- [123] B. Schumm, private communication.
- [124] T. Abe, talk given at XXX International Conference on High Energy Physics, Osaka, Japan (2000).
- [125] J. H. Field and D. Sciarrino, hep-ex/9907018 (1999).
- [126] K. Y. Lee, hep-ph/9904435 (1999).
- [127] M. Chanowitz, hep-ph/9905478 (1999).
- [128] P. F. Harrison *et al.*, THE BABAR PHYSICS BOOK: physics at an asymmetric  $B$  factory, SLAC-R-0504 (1998).
- [129] S. Amato, LHCb Technical Proposal, CERN-LHCC-98-4 (1998).
- [130] BTeV Collaboration, The BTeV Proposal, [http://www-btev.fnal.gov/public\\_documents/btev\\_proposal](http://www-btev.fnal.gov/public_documents/btev_proposal), May 2000.
- [131] E. Cheu *et al.*, FERMILAB-P-0799 (1997).
- [132] J. Bagger *et al.*, The American Linear Collider Group, SLAC-PUB-8495 (2000).
- [133] R. Hawkings and K. Mönig, DESY-99-157 (hep-ph/9910022) (1999). Submitted to Eur. Phys. J.